Experimental Investigation of Saltwater Intrusion Dynamics in Porous Media Under the Influence of Beach Slope and Tidal Conditions

Thesis submitted to the
Indian Institute of Technology Kharagpur
for Award of the Degree

of

Doctor of Philosophy

by

Chitaranjan Dalai

Under the Guidance of

Dr. Anirban Dhar

SCHOOL OF WATER RESOURCES
INDIAN INSTITUTE OF TECHNOLOGY KHARAGPUR
December 2020

APPROVAL OF THE VIVA-VOCE BOARD

/ /2020

Certified that the thesis entitled **Experimental Investigation of Saltwater Intrusion Dynamics in Porous Media Under the Influence of Beach Slope and Tidal Conditions** submitted by **Chitaranjan Dalai** to the Indian Institute of Technology Kharagpur, for the award of the degree of Doctor of Philosophy has been accepted by the external examiners and that the student has successfully defended the thesis in the viva-voce examination held today.

Dr. H. P Reddy	**Dr. Bhabagrahi Sahoo**	**Dr. Manoj K. Tiwari**
Dept. of Civil Engg.	School of Water Resources	School of Water Resources
Member of the DSC	Member of the DSC	Member of the DSC

Dr. Anirban Dhar

Department of Civil Engineering

Supervisor

External Examiner

Chairman, DSC

CERTIFICATE

This is to certify that the thesis entitled **Experimental Investigation of Saltwater Intrusion Dynamics in Porous Media Under the Influence of Beach Slope and Tidal Conditions**, submitted by **Chitaranjan Dalai** to Indian Institute of Technology Kharagpur, is a record of bonafide research work under my supervision and I consider it worthy of consideration for the award of the degree of Doctor of Philosophy of the Institute.

Dr. Anirban Dhar

Associate Professor

Department of Civil Engineering

Indian Institute of Technology Kharagpur

Date: 30/12/2020
Place: IIT Kharagpur

Acknowledgment

I would like to express my sincere gratitude to my advisor Dr. Anirban Dhar for his excellent guidance and constant encouragement. His immense knowledge, motivation, dedication to research, and patience to tolerate a novice like me have inspired me. He has supported me throughout my thesis with his patience and knowledge whilst allowing me the room to work in my own way.

Special thanks to my members of my Doctoral Scrutiny Committee (DSC). I would also like to extend appreciation to the Head, Civil Engineering Department, IIT Kharagpur for providing the laboratory facilities in the department.

I extend my sincere thanks and regards to all Professors in the School of Water Resources for their support and help throughout my stay in the campus.

Everything is meaningless without my parents and my brother. I received their continuous support, motivation, and unconditional love in this journey. Their undoubted faith in me has been the pillars of my strength. I dedicate this thesis to them.

I would also thank my friends for providing invaluable help, continued support, who made my stay here a memorable one. I am also thankful to the Mr. Debasish Ghosh of Hydraulic and Water Resources Engineering Laboratory.

Chitaranjan Dalai

DECLARATION

I certify that

a. The work contained in the thesis is original and has been done by myself under the general supervision of my supervisor.

b. The work has not been submitted to any other Institute for any degree or diploma.

c. I have followed the guidelines provided by the Institute in writing the thesis.

d. I have conformed to the norms and guidelines given in the Ethical Code of Conduct of the Institute.

e. Whenever I have used materials (data, theoretical analysis, and text) from other sources, I have given due credit to them by citing them in the text of the thesis and giving their details in the references.

f. Whenever I have quoted written materials from other sources, I have put them under quotation marks and given due credit to the sources by citing them and giving required details in the references.

Chitaranjan Dalai

List of Journal Publication(s)

1. **Dalai, C.**, Munusamy, S.B., and Dhar, A. "Experimental and numerical investigation of saltwater intrusion dynamics on sloping sandy beach under static seaside boundary condition" *Flow Measurement and Instrumentation*, 75, 101794, 2020.

2. Fingering effect:
The fingering effect, also known as "saltwater fingering" or "gravity current fingering," occurs when a denser fluid, such as saltwater, intrudes into a lighter fluid, such as freshwater, in a non-uniform manner. Instead of forming a smooth interface, the denser fluid penetrates the lighter one in finger-like patterns due to the interplay of buoyancy and fluid dynamics.

3. The G-channel in RGB (Red, Green, Blue) image analysis:
refers to the green component of an image. Utilizing the G-channel involves extracting and analyzing information primarily from the green color channel to study specific features or patterns within an image. This technique is often employed in image processing applications, such as vegetation analysis or object detection, where green components convey significant information.

Abstract

Saltwater intrusion in coastal aquifers is a critical hydro-environmental problem. Intrusion of saltwater in freshwater aquifer occurs due to variable density flow in porous media. The conceptual understanding of saltwater intrusion dynamics is important from aquifer management point of view. In the current research focuses on quantification of influence of beach slope and tidal conditions on saltwater dynamics in single and multilayered porous media. A series of experiments were performed in a 2*D Sand Box Model* (longitudinal & vertical). The Five cases were corresponding to single layered porous media under static saltwater side boundary condition. Also five cases saltwater side boundary condition was changed to tidal one. The Five cases were corresponding to multilayered porous media under static saltwater side boundary condition. The saltwater side boundary condition was changed to tidal one in five cases. Locally available *Clean Sand* was utilized as aquifer material in two cases. However, Grade-I IS Sand was used for all other cases. *Bentonite* was used for low permeability layer. *Rohdamine B* was utilized as the saltwater tracer. Time varying pore-water pressure and images were captured during the experiments. Experimental and numerical analyses showed that the movement rate and volume of the saltwater wedge (i.e., saltwater-freshwater interface toe length) [*1] decreases with the increase in beach slope (e.g., $\alpha = 15^0$ to $\alpha = 30^0$). Fingering effect [*2] was prominent for flatter slopes. The G-Channel (of R-G-B) based image analysis technique [*3] identified the saltwater-freshwater interface and concentration gradient from the experimental images. The 50% concentration isolines obtained from the numerical simulations were matched with the interfaces obtained from the image analysis. Narrow mixing zone was observed for the current set of experiments. Upper saline plume (USP) [*4] developed for all experimental cases for unconfined layer in single and multilayered systems under tidal saltwater side boundary condition. The extent of the upper saline plume was dependent on the freshwater flux. The vertical SGD gap (ζ_0) [*5] decreases with increase in beach face slope whereas the SWI toe length increases. Submarine groundwater discharge (SGD) pathways were identified through tracer injection technique for all the cases. Flow circulation mechanism in saltwater wedge was also identified in $CASE-1/S$. Dimensionless groups were identified for both tidal and non-tidal conditions. The saltwater-freshwater interface toe length and submarine groundwater discharge gap values were dependent on beach slope. Flow stability was determined on the basis of Rayleigh number ($R_a^\star = 150$ to 250 or 750).

4. The upper saline plume:
refers to the upper layer of a saltwater intrusion in an estuary or coastal aquifer. It occurs when denser saltwater intrudes into the freshwater, forming a distinct layer above the underlying freshwater.

5. The vertical SGD (Submarine Groundwater Discharge) gap:
denoted by ζ0, represents the vertical separation between the seafloor and the groundwater table or the level of the submarine groundwater discharge.

Contents

List of Tables

List of Figures

List of Algorithms

Chapter 1

Introduction

1.0 Background

Worldwide coastal zones are highly populated ones (MOEFCC, 2017). Saltwater intrusion in coastal aquifers is a critical hydro-environmental problem (Llopis-Albert and Pulido-Velazquez, 2014; Post and Werner, 2017; Kim and Yang, 2018; Zhang et al., 2019). Intrusion of saltwater (Figure 1.1) in freshwater aquifer occurs due to variable density flow (Holzbecher, 1998) in porous media. Saltwater density is higher than the density of freshwater. High density saltwater generates large concentration gradient in the saltwater-freshwater interface (SWI) zone. Density stratification across the SWI alters the flow dynamics and mass transport in porous media. This flow dynamics generates a landward force. Freshwater flux or submarine groundwater discharge quasi-dynamically maintains the saltwater-freshwater interface and the nutrient balance in sea. This saltwater-freshwater interface can be conceptualized using a) sharp interface approach (no mixing zone), and b) diffused interface approach (wide mixing zone). Hydrostatic balance of saltwater-freshwater interface under sharp interface approximation was first defined by Ghyben and Herzberg (Diersch, 2013). Sharp interface approximation was used in large number of studies , e.g., Reilly and Goodman (1985), Bear (1999), and Cheng and Ouazar (1999). However, sharp interface between two miscible fluids (saltwater and freshwater) cannot exist in reality. Diffused interface approach is required for better representation of saltwater-freshwater transition zone. Henry (1964) and Pinder and Cooper Jr (1970) started the use of density dependent diffused interface approach for coastal problems. Analytical and numerical models with sharp interface approximation are computationally less expensive compared to diffused interface models. Pumping pattern, beach slope, tidal dynamics, and sea level rise influence the saltwater-freshwater interface. Physically consistent and stable/unsatble multiple flow patterns are possible under variable density condition.

Situation becomes worse in presence of tidal oscillations. Density driven flow in porous media remains one of the challenging problems owing to its inherent non-linearity, and limited availability of analytical solutions or availability of standard or field data set (Simpson and Clement, 2003). Thus conceptual understanding of saltwater intrusion dynamics is important from aquifer management point of view.

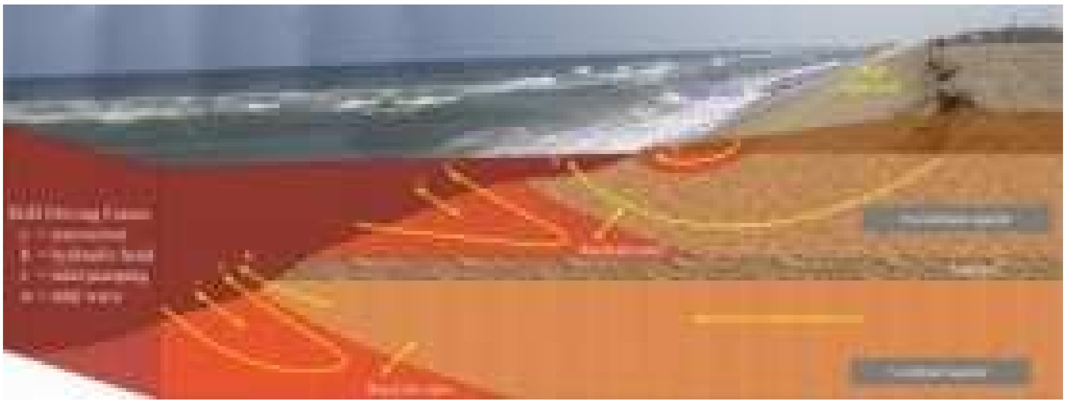

Figure 1.1: Schematic Representation of Multilayered Coastal Aquifer with Driving Forces

Field observations are mostly scattered information and limited by cost. Point data do not provide sufficient information about the dynamics and flow patterns in coastal aquifers. In recent years, different in-situ observation based methods were proposed to identify the fluid dynamics of density dependent flows (Souza and Voss, 1987; Kim et al., 2007; MacAllister et al., 2018). Experimental investigation can provide scientific and systematic information on freshwater-saltwater interface and flow pattern under geometric, kinematic, and dynamic similitude conditions. Moreover, experimental quantification is necessary to evaluate the performance of mathematical/numerical models in the context of robust and reliable engineering solutions. Laboratory-scale experiments were widely used to investigate the behaviour of saltwater interface (Schincariol and Schwartz, 1990; Zhang et al., 2002; Goswami and Clement, 2007; Konz et al., 2008, 2009b, a; Chang and Clement, 2013; Dose et al., 2014; Mehdizadeh et al., 2014). These studies mostly focused on the dispersive mixing zone while solving the variants of the Henry problem (Werner et al., 2013). Experiments were performed under confined or unconfined, steady-state or transient conditions under controlled temperature, pressure, and hydraulic gradient. A large number of studies considered one dimensional ($1D$) saltwater dynamics experiments (Hassanizadeh and Leijnse, 1995; Schotting et al., 1999; Watson et al., 2002; Jiao and Hötzl, 2004). However, saltwater-freshwater interface identification is not possible from $1D$ experiments. Two-dimensional (Goswami and Clement, 2007; Abdoulhalik and Ahmed, 2018) or three-dimensional (Pearl et al., 1993; Oswald and Kinzelbach, 2004; Oswald et al.,

1. Image Analysis: Involves obtaining concentrations through visual interpretation of images. This technique utilizes digital image processing to analyze features.

2. Gamma Radiation technique: this method is employed to assess soil or subsurface properties by measuring the intensity of gamma rays emitted by naturally occurring radioactive isotopes, providing information about soil composition and contamination.

3. Nuclear magnetic Resonance imaging: MRI can be applied to investigate subsurface structures, soil properties, or fluid distribution. The technique relies on the behavior of atomic nuclei, particularly hydrogen protons, in a magnetic field. When exposed to radiofrequency pulses, these nuclei emit signals that are processed to create detailed cross-sectional images, providing valuable information about the composition and spatial distribution of substances within a sample.

2007) *Sand Box Models* are preferred as the shape of the saltwater-freshwater interface is scale dependent. Two-dimensional (2*D*) *Sand Box Models* was utilized for the current study over three-dimensional (3*D*) model considering the ease in a) instrumentation (Non intrusive measurement) and b) visualization. Under controlled conditions, i.e., known boundary conditions, initial condition and porous material properties, repeatability of the experiments can be ascertained. Most of the studies in literature considered vertical beach face for saltwater intrusion experiments (Konz et al., 2008; Lu et al., 2019; Mehdizadeh et al., 2020; Wu et al., 2020). Previous studies either used vertical saltwater boundary or homogenous configuration to understand the density dependent flow process. Vertical beach face is very rare under natural conditions. The density gradient at non-vertical sloping boundary plays a vital role in changing the hydraulic gradient and contaminant transport across the SWI. Only a few studies included the sloping beach face (Zhang et al., 2001; Kuan et al., 2012; Shen et al., 2020) and layered media (Mehdizadeh et al., 2014; Shi et al., 2018; Abdoulhalik et al., 2020). However, experimental quantification of beach slope effect was not studied. The multilayered coastal aquifers are the commonly encountered in real settings. Layer heterogeneity dictates the intra and inter layer mass transfer. Previous saltwater intrusion studies (Ketabchi et al., 2014; Liu et al., 2014; Dose et al., 2014; Mehdizadeh et al., 2014, 2017; Strack and Ausk, 2015) considered layered configurations to represent subsurface heterogeneous conditions. Experimental investigations (Abdoulhalik and Ahmed, 2017b; Strack and Ausk, 2015) showed that layered heterogeneity controls the saltwater-freshwater interface toe location. Saltwater dynamics in sloping beach multilayered porous media was not studied with/without tidal conditions.

Quantification studies can be designed based on head and concentration. Porewater pressure measurement can provide head values. Concentrations were usually obtained from image analysis[1] (Schincariol and Schwartz, 1990; Swartz and Schwartz, 1998; Zhang et al., 2001), gamma radiation technique[2] (Oostrom et al., 1992), or nuclear magnetic resonance imaging technique[3] (Oswald and Kinzelbach, 2004). Tracer studies require colour dye for visualization purpose. Image analysis can be considered as a semi-quantitative method. Previous studies (Schincariol and Schwartz, 1990; Swartz and Schwartz, 1998; Zhang et al., 2001) were based on monochromatic images. These images do not provide sufficient information of the saltwater-freshwater mixing zone Zhang et al. (2001). High resolution coloured images can provide concentration variation information with small measurement errors Konz et al. (2008). Concentration isolines can be checked against the processed images.

The previous works focused on the position, shape and thickness of the saltwater-

1.Convective fingering: This phenomenon occurs when warm fluid rises through a cooler, denser fluid due to buoyancy. The warm fluid forms elongated fingers that penetrate the cooler fluid, creating a characteristic finger-like pattern.Slope matters: On a sloped face, the warm fluid has a downward component of its motion due to gravity. This additional driving force, along with buoyancy, enhances the vertical rise of the fingers and intensifies the fingering effect. The downward tilt also lengthens the fingers by providing them with a larger vertical distance to travel before encountering the cooler fluid above.Vertical face: On a vertical face, the warm fluid only has buoyancy to contend with. This leads to weaker and shorter fingers compared to a sloped face.

freshwater transition zone for density dependent flow in porous media. The convective saltwater circulation phenomenon (Oz et al., 2015) was not studied in detail. The convective fingering effect[1] is another phenomenon not observed in the previous vertical boundary studies. It is well known that variable density flows in porous media can become unstable (Dentz et al., 2006). The occurrence of fingering is caused by flow instabilities due to differences in viscosity and density values between two miscible fluids. Instabilities and fingering develop when a denser fluid lies above the lighter fluid (Manickam and Homsy, 1995; Wooding et al., 1997; Simmons et al., 2001; Diersch and Kolditz, 2002). Viscous fingers develop and can be visualized in the form of corrugated interface (Schincariol et al., 1994). The fingers propagate rapidly, until they reach a stable convective flow regime. The results of density-coupled groundwater flow simulations were typically represented a.t. in terms of concentration isolines (Lee and Cheng, 1974; Volker and Rushton, 1982; Simpson and Clement, 2004) or vector plots of the groundwater velocity (Mehnert and Jennings, 1985; Simmons and Narayan, 1997). Saltwater circulation pattern cannot be determined from these types of information. Circulation patterns in steady state mixed convection problems can be identified from the streamline plots. The density-driven circulation can be conceptually divided into two consecutive processes:(i) flow of high density fluid (in counter clockwise direction) towards low density fluid due to density gradient, and (ii) upward flow of low density fluid towards free surface of the interface. Moreover, limited number of studies are available on circulation pattern in density dependent flows (Oz et al., 2015).

2. Density Dependent circulation:
This difference in density creates a vertical density gradient.

In the Northern Hemisphere, due to the Coriolis effect, this downward flow tends to deviate and form a counterclockwise circulation pattern.

As the denser fluid sinks, it creates a space that needs to be filled. This vacancy triggers the less dense fluid above to rise due to its buoyancy.

1.1 Motivation

Literature review on saltwater dynamics in porous media revealed that most of the experimental studies utilized density dependent flow in porous media with vertical beach face under static and tidal saltwater side boundary conditions. Vertical beach face do not represent the natural coastal aquifer condition. There is need for quantification of influence of beach slope on saltwater dynamics in single and multilayered porous media. The obtained results can be verified with standard numerical code(s). Non-intrusive measurement techniques[9] (e.g., pore-water pressure, image analysis) can be employed for quantitative, semi-quantitative and qualitative analysis. Only a few studies included pressure sensor data acquisition in experiments. Tracer based experimental study can be utilized for capturing time varying images. However, no standard framework is available on experimental image analysis for saltwater dynamics in porous media. There is scope for development of methodology for experimental image analysis. Moreover, no study is available on

Dimensional Analysis is Crucial for Quantifying Scale Effects:

Complexity Reduction: Physical systems often involve multiple variables with different dimensions (e.g., length, time, mass). Dimensional analysis combines these variables into dimensionless groups, reducing the number of independent parameters and simplifying the analysis.

Similitude: Non-dimensional parameters allow for comparison of systems of different sizes that are geometrically, kinematically, and dynamically similar. This makes it possible to predict the behavior of full-scale systems based on smaller-scale experiments or models.

experimental identification of submarine groundwater discharge pathways. Hence, there is need for tracer injection study in freshwater zone. Moreover, Dimensional Analysis study is required for identification of suitable non-dimensional parameters to quantify the scale effect.[1] The current Thesis is aimed at addressing aforementioned gaps.

1.2 Objectives of the Thesis

The main objective of the study is to find out the Influence of varying beach face impact on the saltwater dynamics in porous media. The specific objectives of this thesis are:

2. Pressure Trunsducers pressure transducer placed on the container would sense this change in pressure and send out a corresponding electrical signal.

- To experimentally investigate the saltwater dynamics in single and multilayered systems under static and tidal conditions.
- To develop an image analysis technique to quantify the concentration gradient in porous media.
- To quantify the saltwater dynamics through numerical analysis and direct pressure measurement method with pressure transducers.[2]
- To quantify the influence of beach slope on saltwater movement.

1.3 Outline of the Thesis

The thesis consists of seven chapters, including this introductory chapter. Present chapter introduces the fundamentals of saltwater intrusion process including previous works, motivation, objectives of the Thesis. However, relevant literature for individual topics are included in respective chapters.

Chapter 2 is devoted to the experimental design and methodology. Detailed descriptions of instrumentation and material characterization are also presented.

Chapter **??** deals with experimental conceptualization under static condition. It also includes a basic image analysis method. Pore-water measurement, numerical simulation and analytical solution are used for quantitative analysis. Circulation patterns in saltwater wedge and freshwater zones are also included.

Chapter 3 presents laboratory scale experimental observations with varying beach slopes in single layered porous media under static and tidal saltwater side boundary conditions. A novel G-Channel based image analysis technique is presented. Submarine groundwater discharge pathways are also included.

Chapter 4 presents laboratory scale experimental observations with varying beach slopes in multilayered porous media under static and tidal saltwater side boundary conditions. Submarine groundwater discharge pathways are also included.

Chapter 5 includes Dimensional Analysis for both single and multilayered porous media under static and tidal saltwater side boundary conditions. Expressions for saltwater-freshwater interface toe length and submarine groundwater discharge gaps are presented.

In Chapter 5, overview of this study, conclusions, and recommendations for further work are presented.

1. Peristaltic pumps:
sometimes called hose pumps or tube pumps, are a unique type of positive displacement pump that use rollers or a rotor to squeeze a flexible tube, propelling the fluid inside along a specific path. Imagine squeezing a toothpaste tube – that's essentially how a peristaltic pump works, but with much more control and precision.

2. CTD DRIVER
Collects Conductivity (salinity), Temperature, and Depth data in the ocean.A driver is a software component that allows a computer system to communicate with a specific hardware device, like the CTD instrument in this case. The CTD driver manages data communication between the CTD and the computer software that will analyze the collected data.

Chapter 2

Experimental Design & Methodology

2.0 Overview

This Chapter focuses on the basics of experimental design. There are two major components in the experimental design, a) instrumentation and b) material characterization. Use of higher precision instruments can eliminate instrumentation error. However, selection of proper material can eliminate/ reduce errors in the inherent assumptions used in the controlled experiments. In this Thesis, a two dimensional ($2D$) *Sand Box Model* was utilized for conducting the physical experiments. Both instrumentation and material selection (including characterization) are discussed in detail.

2.1 Instrumentation

The experimental instrumentation can be divided into five parts/ units a) Sand Box Model, b) Tidal Mechanism, c) Pressure Transducer, d) Data Acquisition System, and e) Digital Camera. Moreover, Peristaltic Pump [1] and Conductivity Temperature, and Depth (CTD) Diver [2] were also utilized for the experiments.

2.1.1 Sand Box Model

The *Sand Box Model* was utilized to study variable density currents in both confined and unconfined hydraulic conditions. The frame structure of the experimental setup is made of stainless steel. It is 3.0 m long, 1.0 m high and 0.02 m wide and resting on three iron frame bases (Figure 2.1). The width of the setup is very small compared to other two dimensions to ensure the $2D$ flow in the vertical cross section (Cartwright et al., 2004; Goswami and Clement, 2007; Luyun Jr et al., 2011; Kuan et al., 2012; Zhou et al., 2016; Yu et al., 2019a).

(a)

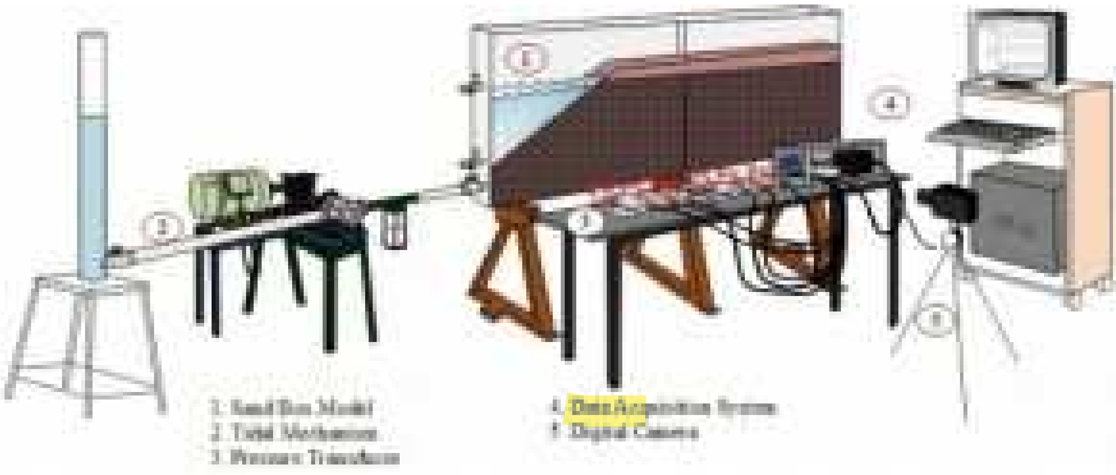

(b)

Figure 2.1: *Sand Box Model*: a Pictorial Representation of Experimental Setup and b Schematic Representation of Experimental Setup. See page 44

The *Sand Box Model* is made of two glass plates of 180 *mm* thickness parallelly placed at a distance of 0.02 *m*. Two water reservoirs (each 50 *mm* length) are available at both ends. The right reservoir is used to feed (flux condition) freshwater flow to the system. Constant head condition is maintained in the left reservoir (filled with saltwater). An overflow outlet pipe (5 *mm* diameter) is place at a height of 0.64 *m* from the base of the model. Stainless steel mesh (0.1 *mm* opening) is used to sperate both the reservoirs from the middle sand box zone. The top of

Why used??

1.Rotodyne DC motor:

Brushless DC motor: Unlike brushed DC motors that use brushes to contact the rotor and generate sparks, Rotodyne motors have electronically controlled commutation, offering smoother operation, longer lifespan, and reduced maintenance needs.

High torque and displacement: Compared to conventional DC motors, Rotodyne motors deliver significantly higher torque and displacement per unit size, making them ideal for applications requiring powerful and compact solutions.

High efficiency

the setup is in direct contact with the atmosphere representing unconfined aquifer condition. Bottom part of the setup has 18 flow controlling outlets including one each at the bottom of the end reservoirs. The back side of glass wall has 59 openings (8 *mm* diameter) for taking pressure measurements and injection-extraction of fluid.

2.1.2 Tidal Mechanism

The tidal mechanism was designed to impose a periodic head boundary condition at the left side of the *Sand Box Model*. It has four sub-units i) Water Column, ii) Flexible Pipe Connector, iii) Rotodyne DC Motor,[3] iv) Control System. Figure 2.2 shows different components of the Tidal Mechanism. This mechanism produces a linear periodic water level variation. The rotodyne DC motor transfers saltwater from the column to the *Sand Box Model* through flexible pipe connector in forward cycle. In backward cycle, water from *Sand Box Model* gets transferred to the saltwater column. This forward-backward (direction) motion of rotodyne DC motor and its duration are automatically controlled by the *Control System*. A potentiometer circuit controls the rotational speed (rpm: revolutions per minute) of the DC motor. Therefore, water level variations (amplitude of fluctuations) of different periodicity could be imposed by changing the speed of the motor. High and low tide levels can be generated from clockwise and anti-clockwise rotation of the motor. Two switches are available as a backup to initiate the cycle (direction) change in case of micro switch failure (automatic).

2.Relation between effective overpressure and pore water pressure:
Effective Overpressure Calculation: In hydrostatic conditions, pore water pressure increases linearly with depth due to the weight of the water column above. To determine the effective overpressure, which reflects pressure beyond this hydrostatic component, you subtract the hydrostatic pressure from the measured pore water pressure.

Piezometric Head Estimation: In confined or non-hydrostatic conditions, the hydrostatic assumption doesn't hold, and pore water pressure doesn't strictly follow a linear relationship with depth. Under these circumstances, the measured pore water pressure itself can be directly used to estimate the piezometric head, as it reflects the total hydraulic potential at that point.

2.1.3 Pressure Transducer

Pressure Transducers were used to measure the pore water pressure developed within the saturated porous medium. Pore water pressure refers to the pressure of water held or trapped between the inter-particle gaps. Under phreatic or unconfined condition the pore water pressure is hydrostatic in nature. Pore water pressure increases with salinity. Effective overpressure was estimated from the pore water pressure by subtracting the hydrostatic component from it. Under confined or non-hydrostatic pressure condition, pore water pressure was directly used to estimate the piezometric head[2]. Water table wave information was extracted from the pressure transducer measurements. Forces generated due to buoyancy and capillary effects generally oppose each other. Buoyancy originates from the density difference between the brine phase and the fresh water phase, and points toward upward direction. Capillary pressure is a function of the pore size. It opposes the movement of brine in response to buoyancy or other forces.

(a)

(b)

Figure 2.2: Tidal Control Mechanism a Tidal Mechanism and b Control Panel (see page 46)

Pore water pressured was captured by Super TJE ultra precision pressure transducers (STJE AP111) from Honeywell. The pressure transducers (with cylindrical stainless steel casing of 50 mm diameter and 64 mm high) can measure up to 10 psi gauge (psi gauge pressure)[1] with an accuracy of ± 0.05 %. This is equivalent to 7.0319 m water head with an accuracy of ± 0.0035 m. Each externally mounted pressure transducers were connected to the openings (8 mm diameter) present in the rear glass wall of *Sand Box Model* through flexible rubber tube (8 mm diame-

1. PSI gauge pressure:
PSI gauge pressure is a measurement of pressure relative to the surrounding atmospheric pressure. PSI stands for pounds per square inch. It's an imperial unit of pressure, where one PSI is equal to the force of one pound exerted on an area of one square inch.

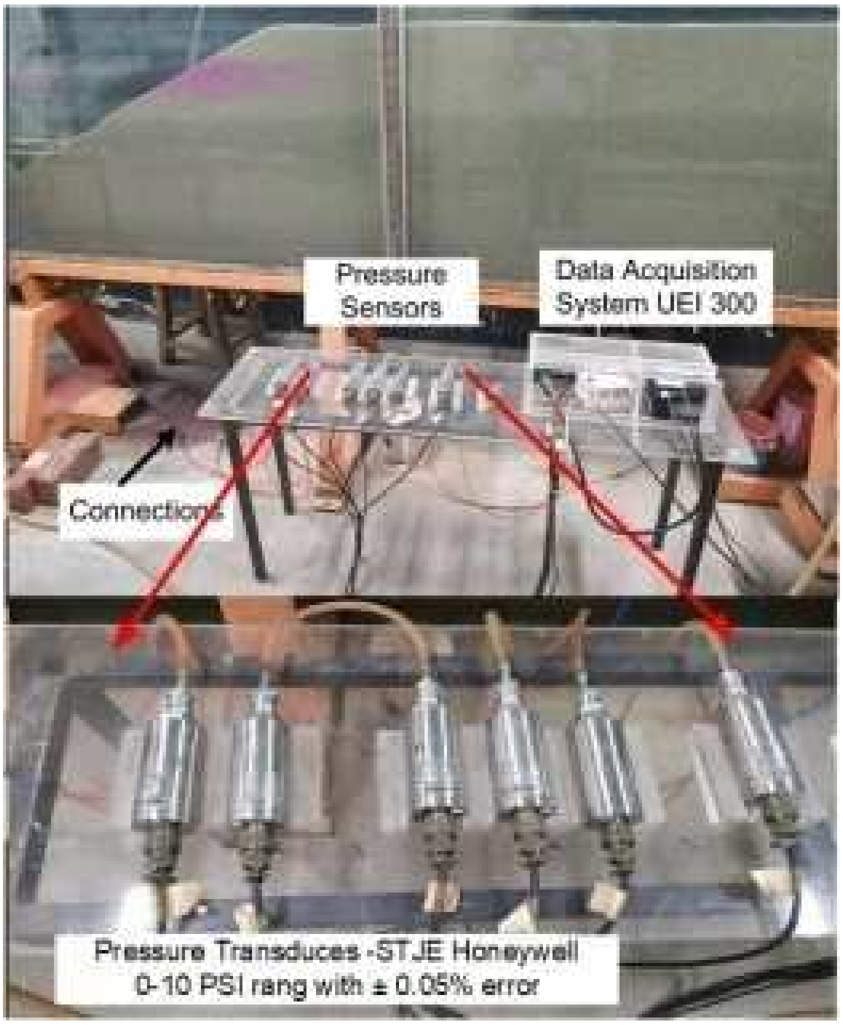

Figure 2.3: Pressure Transducers and Data Acquisition System (see page 47)

ter). The data sampling frequency used in the present study was 20 HZ to avoid instrument response time related issues.

2.1.4 Data Acquisition System

Data Acquisition (DAQ) System was used acquire data from the pressure transducers. Pressure transducers send pore water pressure equivalent electrical signals to DAQ. DAQ supplies power to the transducer. After signal conditioning, the transducer signal is passed to the analog input board. The analog input board (UEILogger 300, Figure 2.4) converts the conditioned analog voltage into a computer readable digital format. The UEIlogger is connected to a computer through ethernet port. The raw data can be visualized and transferred from the UEILogger Graphical User Interface.

Process Flow:
Pressure Transducers: Continuously measure pore water pressure. Send corresponding electrical signals to the DAQ system.

DAQ System: Provides power to the transducers. Refines the electrical signals (signal conditioning). Passes the conditioned signals to the analog input board.

Analog Input Board (UEILogger 300): Transforms the analog signals into digital data.

Data Transfer: Digital data is sent to the computer via Ethernet.

UEILogger GUI: Receives and displays the raw data in a visual format. Allows for data storage and further analysis.

Figure 2.4: UEILogger 300— A: Network Connectors, B: USB Port, C: SD Card Slot, D: RS-232 Port, E: I/O Board/Layer Slots, F: I/O Layer Status LEDs, G: Sync Connector, H: Start/Reset Button, I: Communication Status LEDs, J: Power Connectors (page 48)

2.1.5 Digital Camera

The Digital Single Lens Reflex (DSLR) camera Nikon d5100 was utilized for capturing time varying experimental saltwater-fresh water interface movement visible from the front glass wall of the *Sand Box Model*. The camera mounted on a fixed tripod was placed centrally in front of the *Sand Box Model* at a distance of 1 m (Figure 2.1b). A wide angle lens was used to overcome the space restriction. The recorded images show mild distortion toward the periphery of the frame. Distortion removal technique is discussed in Chapter **??**. Images were capture using the self capturing mode at an interval of 2 s to 2 min depending on the stage of saltwater-freshwater interface development.

Figure 2.5: Digital Single Lens Reflex (DSLR) Camera (Nikon d5100)

2.1.6 Peripheral Apparatus

Peristaltic Pump and CTD Diver were used for freshwater-saltwater supplies and conductivity-depth measurements, respectively.

2.1.6.1 Peristaltic Pump

Two *Peristaltic Pumps* were utilized for i) freshwater supply: to maintain freshwater flux at the right side boundary, and ii) saltwater supply: to maintain saltwater density at the left side boundary. A set of rotating rollers squeeze the tube to supply water at a constant flow rate. Electrolab India make Peristaltic pumps of Model:*PP-50VX* were used (Figure 2.6).

Figure 2.6: Variable Speed Peristaltic Pump (PP-50VX). see page 49

The flux was controlled by fixing the rotational speed (rpm: revolutions per minute) of the motor. It varies from 1 to 200 rpm. The pumps were individually calibrated to obtain the relationship between rotational speed and flow rate (Figure 2.7).

2.1.6.2 Conductivity, Temperature and Depth (CTD) Diver

Two *CTD Divers* were utilized in i) water column: to monitor the time-varying saltwater density variation, and ii) left compartment of the *Sand Box Model*: to monitor the time-varying saltwater density and water level variations. The CTD Diver Model: *DI272* (Make: Schlumberger Water Services, Delft, Netherlands) measures absolute pressure, temperature, and conductivity of the water. CTD diver can operate in conductivity range of 0 to 120 mS/cm (equivalent to 0 mg/l to 76800 mg/l) with an accuracy of $\pm$ 1 %. In the Thesis, sampling was performed at an interval of 15 *milliseconds* for 10-12 *hours*. Both the divers were calibrated based on known salt concentration values.

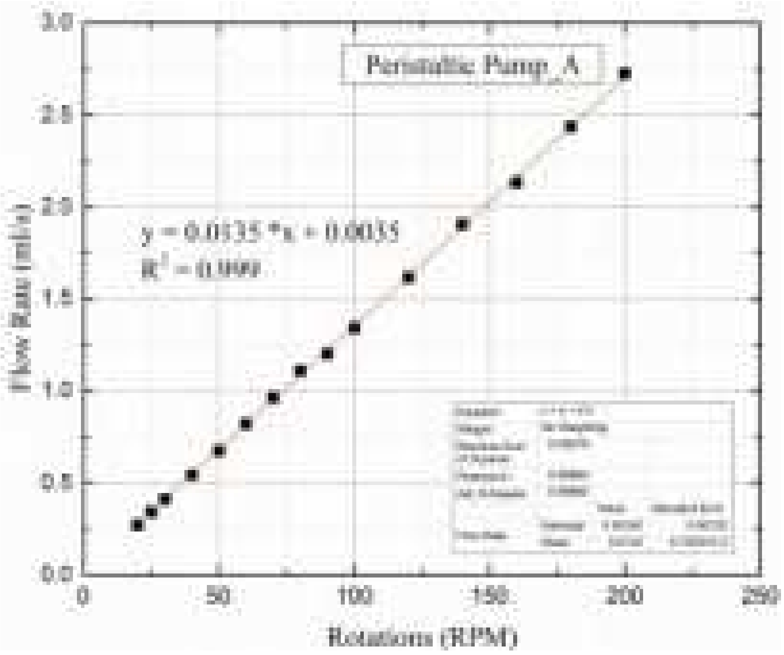

(a) Peristaltic Pump A.

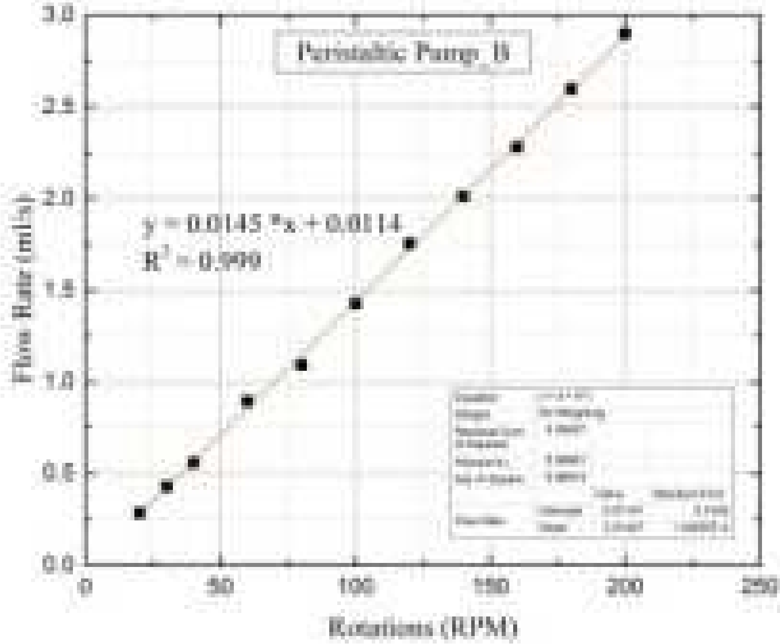

(b) Peristaltic Pump B.

Figure 2.7: Calibration of Peristaltic Pump See page 50

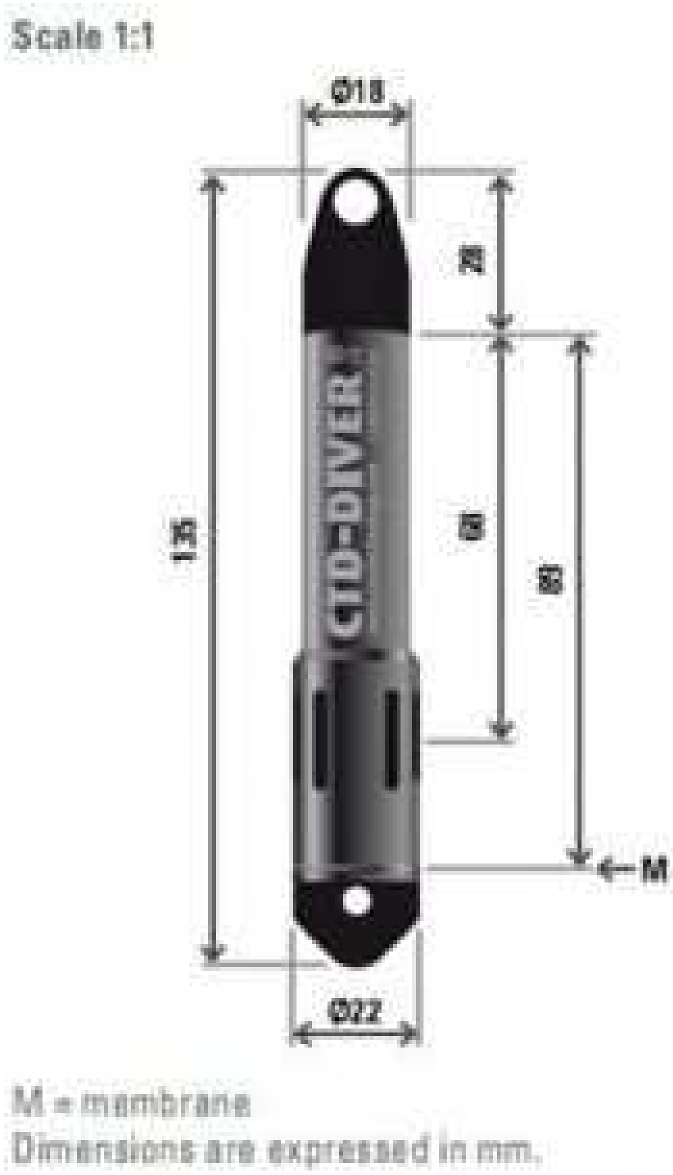

Figure 2.8: Conductivity, Temperature and Depth (CTD) Diver

See page 51

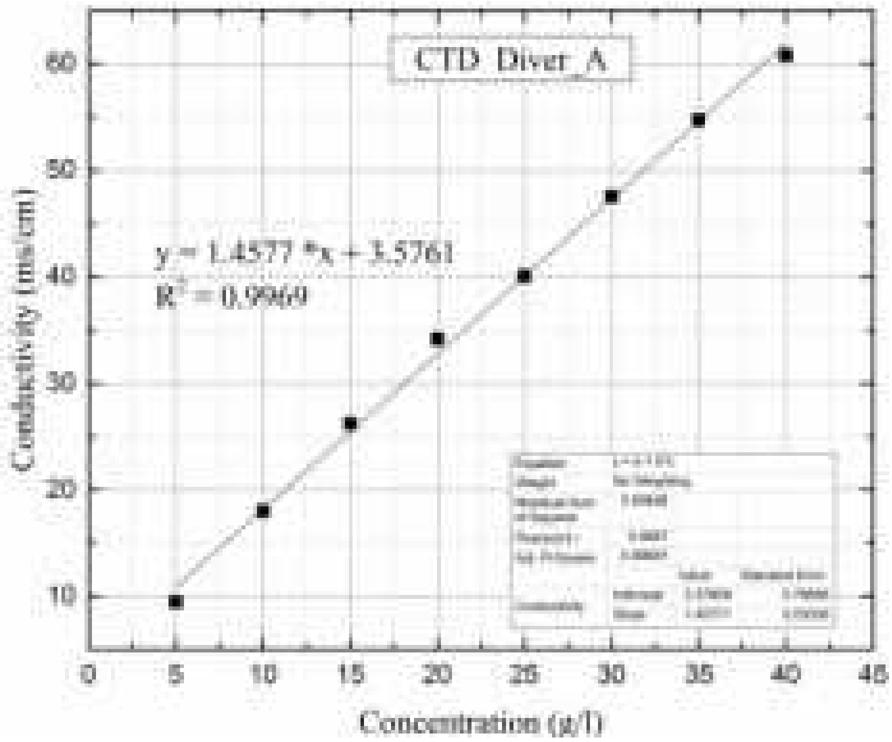

(a) CTD Diver A.

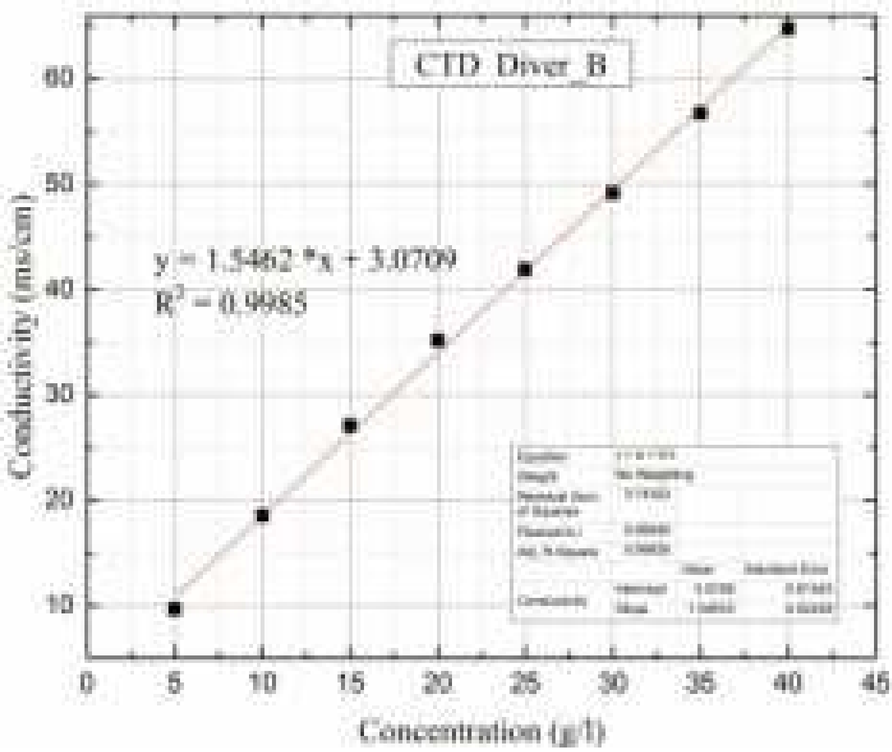

(b) CTD Diver B.

Figure 2.9: Calibration of CTD Diver

2.2 Material Characterization

The *Material Characterization* can be divided into two parts/units a) Porous Materials/Aquifer Materials, and b) Tracer for Saltwater.

2.2.1 Porous Materials/Aquifer Materials

Three types of porous material i) Locally available clean sand, ii) Grade-I Indian Standard sand (IS 650:1991),[1] iii) Bentonite clay were used as aquifer/aquitard material in the *Sand Box Model*. Scanning Electron Microscope (SEM) Micrograph[2] and Energy-dispersive X-ray (EDX) spectrum[3] of *Clean Sand*, *Grade-I IS Sand*, and Bentonite are shown in Figures 2.11, 2.12, and 2.13, respectively. The SEM images at different magnifications indicate the presence of noticeable pores. Maximum pore space can be observed for Bentonite. This might cause an increase in the surface area and pore volume. The EDX analysis for *Clean Sand* indicates presence of Silica, Aluminum, Carbon, Oxygen, Iron and a small percentage of Potassium. However, EDX spectrum of Grade-I IS Sand shows the presence of Silica, Aluminum, Oxygen, and Potassium. Thus, it evident that Grade-I IS Sand is free from organic impurities (indicated by Carbon). EDX spectrum of Bentonite shows the presence of Silica, Oxygen, Iron and Potassium. *Clean Sand* was selected based on local availability. The clean sand was washed with water to remove fine clay particles attached to the sand grains. The cleaned sand was dried at room temperature. However, repeatability of the experimental results could be ensured with standard material. Grade-I IS Sand (IS 650:1991) was selected as porous material as it possesses standard physical characteristics. Bentonite was used as aquitard material for multilayered porous medium experiments.

(a) Clean Sand (b) Grade-I IS Sand (c) Bentonite Clay

Figure 2.10: Experimental Porous Materials

Physical properties for the Sands were determined as per the methods prescribed in Bureau of Indian Standards codes (Table 2.1). The specific gravity,

1. Standard Sand Indian Grade 1:
Bag of 25 Kg is made of local (French Source) natural silica sand (silica content higher than 98%), having a water content lower than 0.1 %. The constituent grains of this natural sand are uncrushed and of rounded form.
The standard sand is obtained from Ennore, Tamil Nadu, and is also known as Ennore sand.

2. Scanning Electron Microscope (SEM) Micrograph:
Electron Beam:
Instead of light, SEM uses a focused beam of high-energy electrons.

Scanning:
This beam scans across the surface of the sample in a raster pattern, like a TV screen.

Secondary Electrons (SE): These reveal the sample's topography, providing a 3D-like image of its surface features.

Backscattered Electrons (BSE): These tell about the composition of the sample, as denser areas scatter electrons more strongly, creating brighter regions in the image.

X-rays: These give information about the elemental composition of the sample.

An EDX spectrum

is a type of analysis that reveals the elemental composition of a material.It works by bombarding the sample with an electron beam, causing atoms to emit X-rays.Each element emits X-rays at specific energies, like a fingerprint, allowing identification and quantification.

X-axis: Shows the energy of the X-rays (keV).

Y-axis: Shows the number of X-rays detected at each energy level.

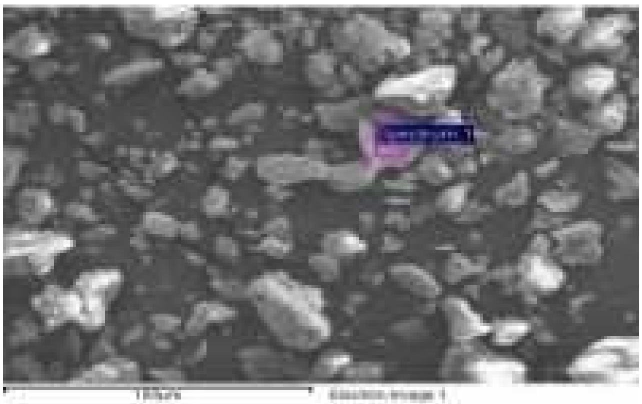

(a) SEM Micrographs

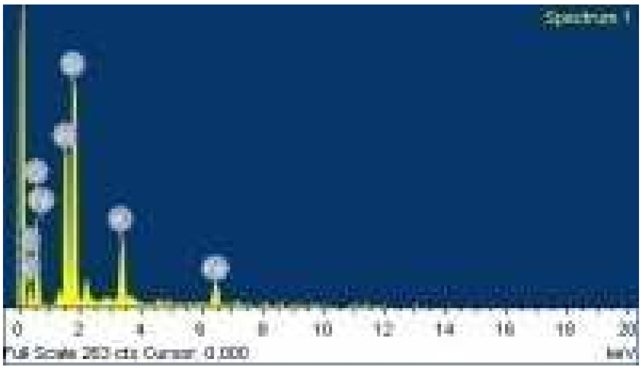

(b) EDX Spectrums

Figure 2.11: SEM Micrographs and EDX Spectrums of Clean Sand

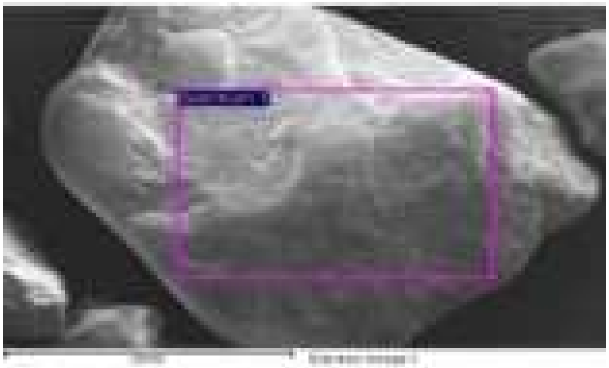

(a) SEM Micrographs

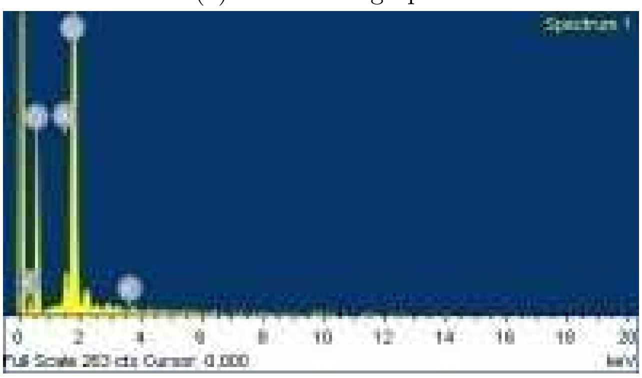

(b) EDX Spectrums

Figure 2.12: SEM Micrographs and EDX Spectrums of Grade-I IS Sand See page 54

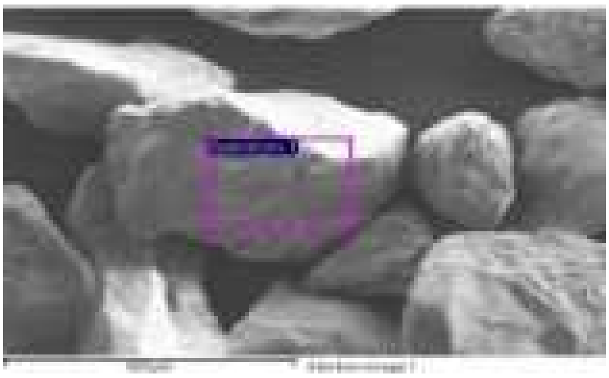

(a) SEM Micrographs

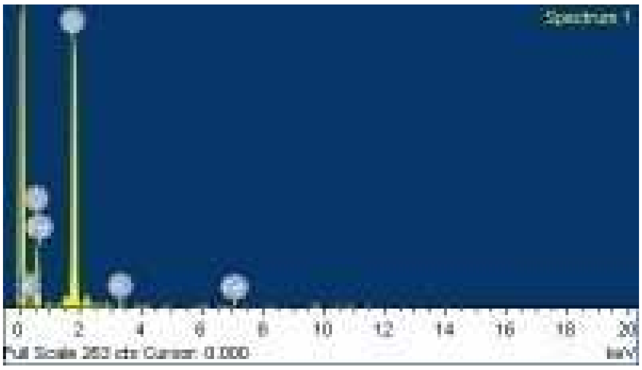

(b) EDX Spectrums

1. The coefficient of gradation, also known as the coefficient of curvature

Figure 2.13: SEM Micrographs and EDX Spectrums of Bentonite Clay

mean grain size, coefficient of uniformity, coefficient of gradation,[1] and hydraulic conductivity values for both *Clean Sand* and *Grade-I IS Sand* are summarized in Table 2.2. Grain size distribution plots for *Clean Sand* and *Grade-I IS Sand* are shown in Figures 2.14 and 2.15, respectively. Coefficient of uniformity and coefficient of gradation indicate that both the Sands are of uniform grade. However, hydraulic conductivity value is higher for Grade-I IS Sand compared to Clean Sand.

Table 2.1: Relevant Porous Material Properties and BIS Codes

Properties	IS Code
Grain size analysis	IS-2720 (Part 4):1985
Specific gravity	IS:2720(Part 4)-1985
Permeability	IS:2720(Part XVII)-1966
Indian Standard Sand	IS 650:1991

2.2.2 Tracer for Saltwater

Saltwater ($NaCl$) does not have any specific colour. Thus a suitable tracer is required to identify the saltwater-freshwater interface movement. Tracer will

Table 2.2: Physical Properties of Aquifer Materials

Properties	Clean Sand	Grade-I IS Sand
Specific gravity (G)	2.65	2.67
Mean grain size, $D_{50}(mm)$	1.025	1.124
Coefficient of uniformity, C_u	1.4	1.36
Coefficient of gradation, C_c	1.07	0.75
Permeability K (m/sec)	0.00017	0.00207

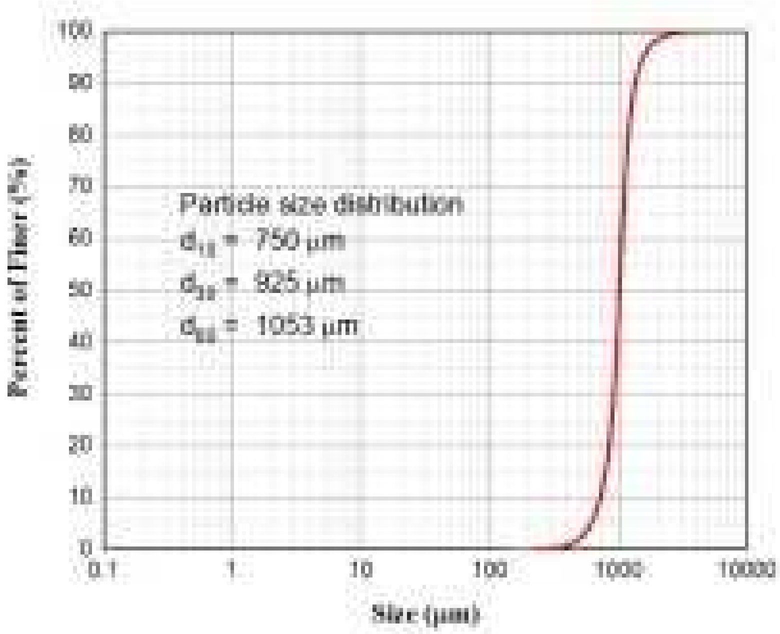

Figure 2.14: Grain Size Distribution of Clean Sand

1. Buoyancy neutral means that the tracer should have the same density as the medium it's moving through.

convect at the local seepage velocity. Moreover, tracer should be buoyancy neutral[1]. Thus, the tracer should be i) soluble in aqueous solution, ii) non-reactive (low absorption), and ii) non-diffusive. Four Dyes [a natural or synthetic substance, Adegoke and Bello (2015)] were tested, e.g., i) Rhodamine-B (C.l. 45170, Basic Violet 10), ii) Indigo Carmine AR (C.l. 73015, Acid Blue 74), iii) Methyl Orange Indicator ACS (C.l. 13025, Acid Orange 52), iv) Commercial Food Dye(Neoteric DCBA Ideas).

Molecular structure of first three dyes are shown in Figures 2.16, 2.17, and 2.18. If a dye dissociates into positively charged ion in aqueous solution is called cationic dye or basic dye. Otherwise, it is called anionic dye or acidic dye in case of negatively charged ion. All four dyes are soluble in aqueous solution. Rhodamine B is cationic dye, whereas Indigo Carmine and Methyl Orange are acidic ones. Diffused reflectance absorption spectra (DRS) [with OR-3100 spectrophotometer (ORLAB)] were recorded to check the absorption characteristics. Ultra-

Diffused reflectance absorption spectra (DRS):

This is a spectroscopic technique that measures the light reflected by a sample after it interacts with the material.

Unlike traditional transmission spectroscopy, where light passes through the sample, DRS deals with scattered and reflected light.

DRS is valuable for analyzing opaque or highly scattering materials such as powders, films, and pigments.

Measuring the DRS provides information about the wavelengths of light that the sample absorbs.

Analyzing the absorption peaks in the spectra reveals details about the electronic structure and composition of the material.

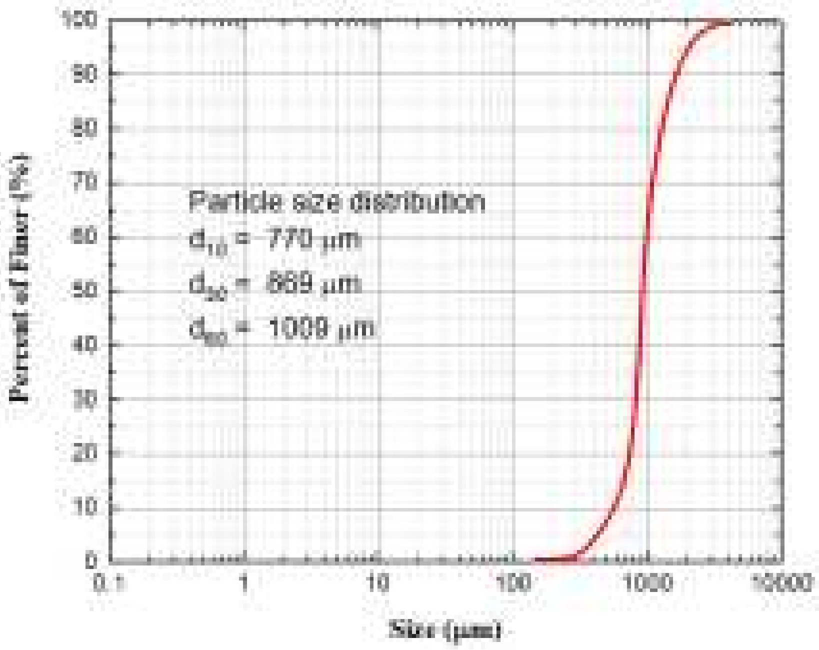

Figure 2.15: Grain Size Distribution of Grade-I IS Sand

Figure 2.16: Molecular Structure of Rhodamine B

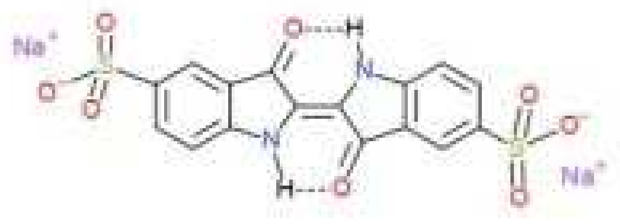

Figure 2.17: Molecular Structure of Indigo Carmine

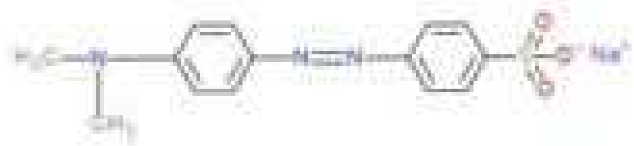

Figure 2.18: Molecular Structure of Methyl Orange

violet–Visible (UV/vis) Spectroscopic measurements (in the range 380 to 720 nm) quantify the interaction of visible light with aqueous solution of dye. This allows determination of unknown solution concentration values. Transmittance is determined by taking the proportion of the intensity of light leaving the dye solution to the intensity of light entering the dye solution. Deionized water was used for preparing aqueous solution for the tests.

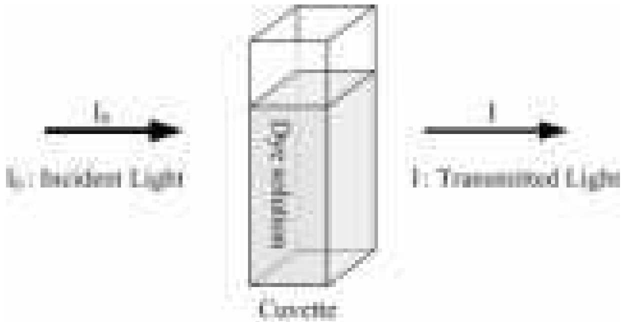

Figure 2.19: Transmittance ($T = I/I_0$) of Light by Aqueous Solution.

Absorbance (A) is calculated from the transmittance:

$$A = \log_{10}\left(\frac{1}{T}\right) \tag{2.1}$$

where T is transmittance of the light by dye solution. The absorption spectra is a plot of the absorbance of a sample (for a particular dye concentration) as a function of wavelength. Figures 2.20 and 2.21 show the absorbance spectra for different dyes in aqueous solution. Maximum absorption for dyes occur at different wavelengths.

Beer's Law plot is between absorbance and known concentration of the solution. This plot can be utilized to determine the unknown concentration level corresponding to a known absorbance level. The amount of light absorbed at specific wavelength is directly proportional to the concentration of the solution. Figures 2.20 and 2.21 show the *Beer's Law* plots for different dyes in aqueous solution. The present research focuses on saltwater dynamics in porous medium (primarily in Sand). All the absorption experiment results shown in Figures 2.20 and 2.21 were performed without Sand. Absorption rate and amount varies for different dyes in presence of sand (Figures 2.22 and 2.23). In order to measure the adsorption batch studies were carried out with 100 ml solution (mixed with 100 mg dye). Six different concentration levels were considered. Adsorption values were recorded using OR-3100 spectrophotometer (ORLAB)corresponding to different wavelengths. The maximum absorbance values corresponding to different concentration levels are visible in Figure 2.22 and 2.23 . The change in absorbance (with and without Sand) of the dye solution was used to calculate the dye concentration

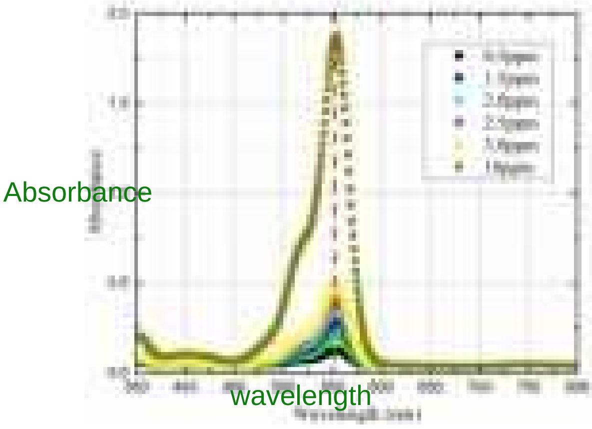

(a) Absorption Spectra of Rhodamine B

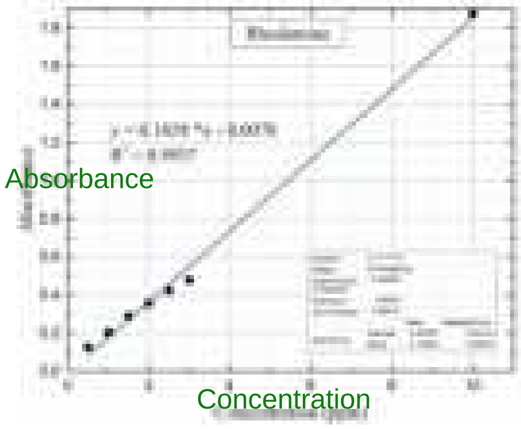

(b) Beer's Law Plot for Rhodamine B

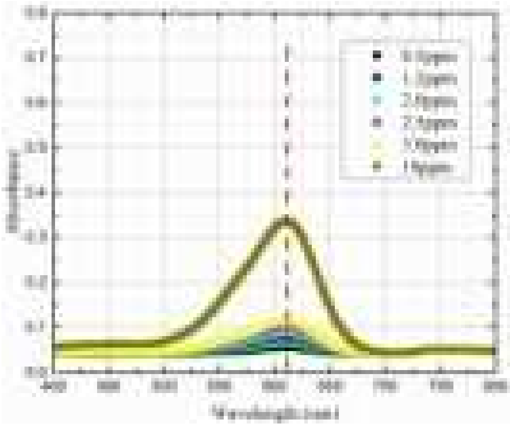

(c) Absorption Spectra of Indigo Carmine

See page 60

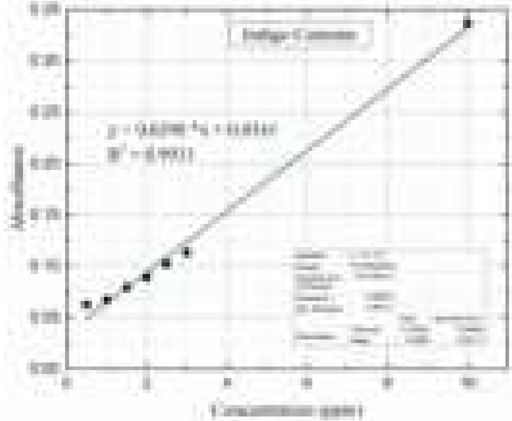

(d) Beer's Law Plot for Indigo Carmine

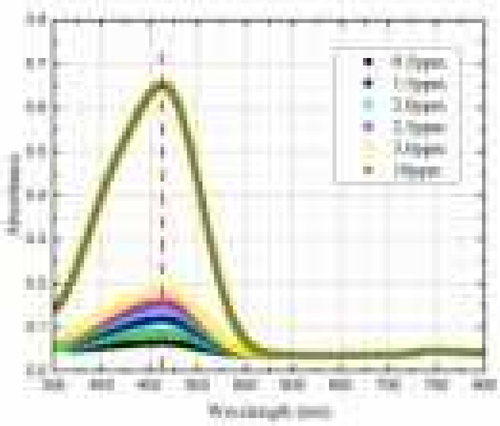

(e) Absorption Spectra of Methyl Orange

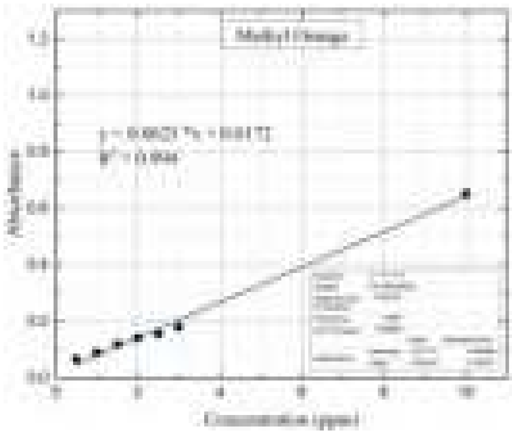

(f) Beer's Law Plot for Methyl orange

Figure 2.20: Absorption Spectra of Rhodamine B, Indigo Carmine, Methyl Orange in Aqueous Solution

in solution and the percentage adsorption of the dye on sand.

$$Dye\ Adsorption(\%) = \left(1 - \frac{C_f}{C_i}\right) \times 100 \tag{2.2}$$

where $C_f\ and\ C_i$ are the initial and the final concentration values of the dye solution, respectively. From Figure 2.24, it is clear that adsorbed amount changes with dye. *Rhodamine-B* was identified as the most suitable dye for the current

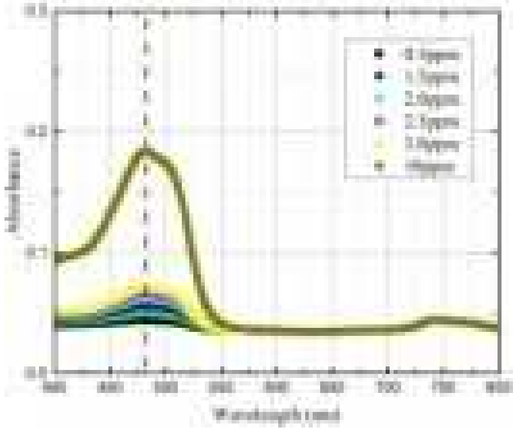

(a) Absorption Spectra of Commercial Food Dye

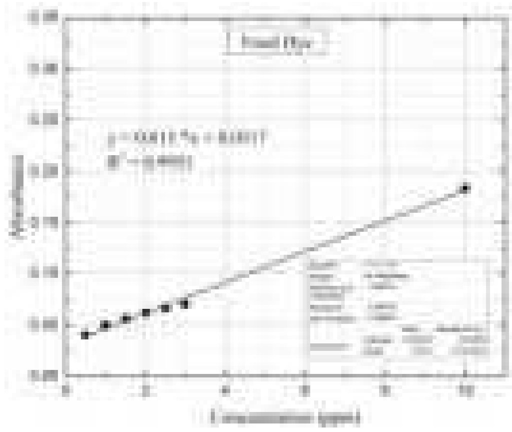

(b) Beer's Law Plot for Commercial Food Dye

Figure 2.21: Absorption Spectra of Commercial Food Dye in Aqueous Solution

research with Sand.

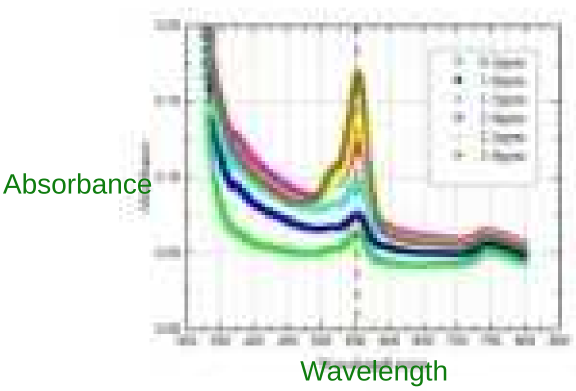

(a) Rhodamine B

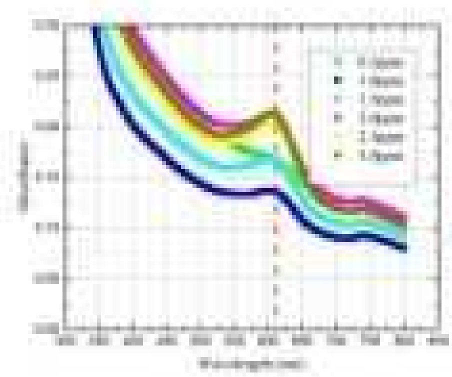

(b) Indigo Carmine

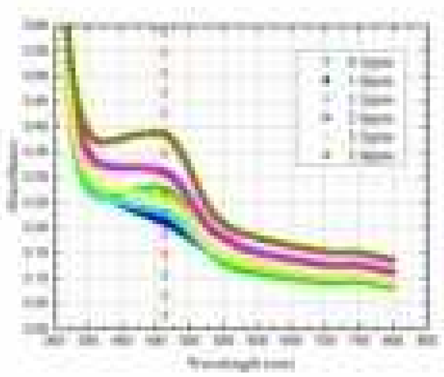

(c) Methyl Orange

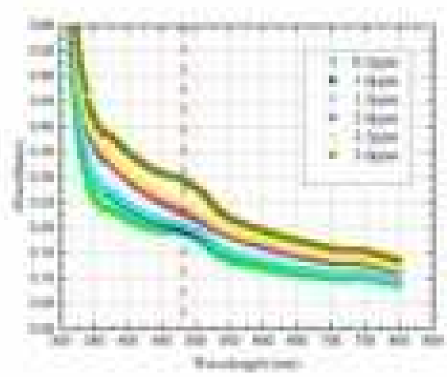

(d) Commercial Food Dye

Figure 2.22: Absorption Spectra of Dyes in Aqueous Solutions at Different Concentration Levels with Clean Sand

Diffusion characteristics vary for different dyes in presence of sand. Moreover, saltwater-freshwater interface is diffused in nature. A scaled version of *Sand Box*

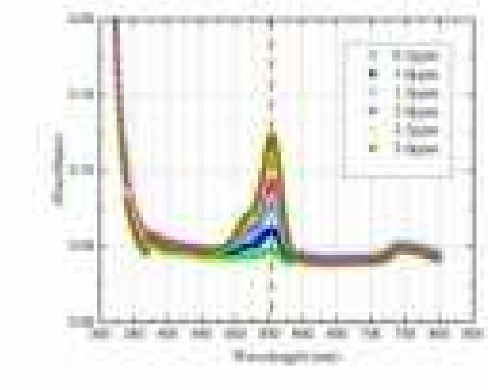

(a) Rhodamine B

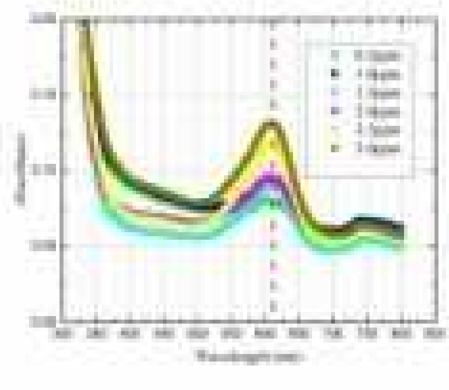

(b) Indigo Carmine

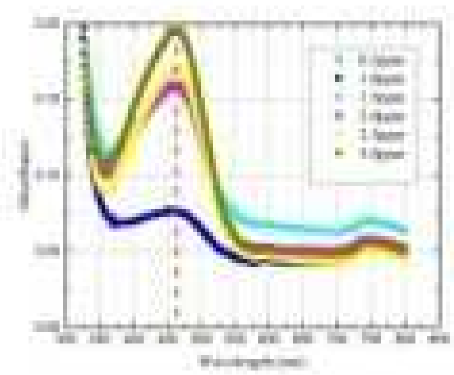

(c) Methyl Orange

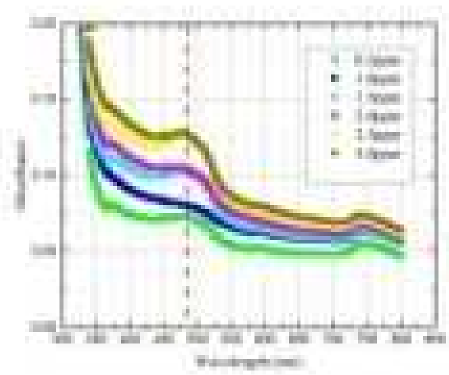

(d) Commercial Food Dye

Figure 2.23: Absorption Spectra of Dyes in Aqueous Solutions at Different Concentration Levels with Grade-I IS Sand

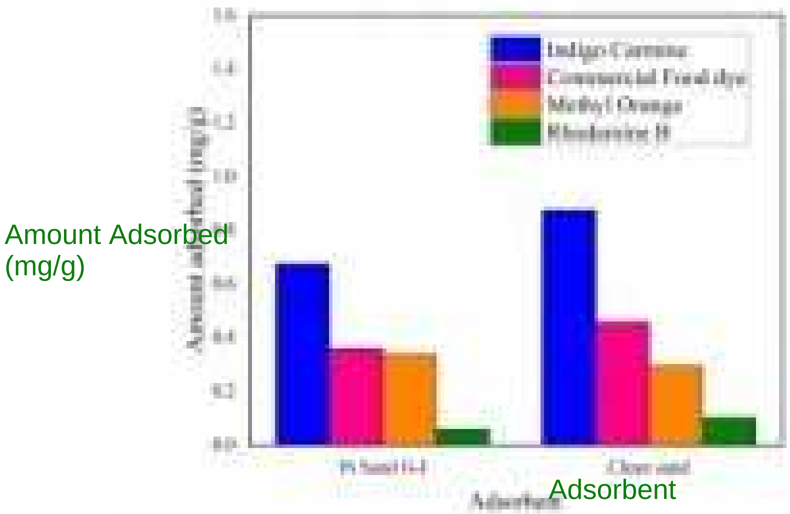

Figure 2.24: Dye Adsorption Performance (Adsorbent Dose = 10 g/l, Dye Concentration = 10 mg/l)

Model was utilized for visualization of saltwater-freshwater interface in presence dye mixed saltwater. Porous material was placed in the middle compartment of the model. Static saltwater (prepared by dissolving 35 *g NaCl* per liter of water) head boundary condition was applied in the left compartment of the scaled model. Freshwater head was considered at right side compartment. Development of saltwater wedge was observed for the experiments. The interface gets generated due to difference in the fluid densities (between saltwater and freshwater). All four dyes were tested under similar conditions. Figures 2.25 and 2.26 show the saltwater wedge and saltwater-freshwater interface in *IS Sand*. It is evident that both the dyes show similar results in terms of diffusion. However, *Rhodamine-B* was identified as the most suitable dye considering the better visualization effect.

Figure 2.25: Salt Wedge and Saltwater-Freshwater Interface for Rhodamine-B in IS Sand

Figure 2.26: Salt Wedge and Saltwater-Freshwater Interface for Food Dye in IS Sand

2.3 Summary

In this chapter detailed descriptions of the experimental setups, peripheral apparatus and material characteristics were provided. The details of the *Sand Box Model* used for laboratory scale experiments was explained. Next Chapter deals with the laboratory experiments on saltwater movement in single and multilayered porous media (Aquifer Material: Clean Sand) under static saltwater boundary condition.

Chapter 3

Influence of Beach Slope on Saltwater Movement in Single Layer Under Static and Tidal Conditions

3.0 Overview

The coastal aquifer boundary is generally non-vertical. The classical *Henry Problem* (Henry, 1960) considered a vertical coastal boundary due to difficulties in incorporating a sloping geometry in finite difference model. Most of the previous laboratory tests were performed under vertical seaside boundary approximation, e.g., water table salinization (Nakagawa et al., 2005; Goswami and Clement, 2007; Oz et al., 2015), physical barrier system (Abdoulhalik et al., 2017; Armanuos et al., 2019) saltwater upconing (Werner et al., 2009; Jakovovic et al., 2016; Abdoulhalik and Ahmed, 2018). Process complexity increases with the sloping beach condition. Tide and wave forces create complex seaside boundary condition (combination of static and dynamic pressure head conditions). Laboratory scale sloping beach condition was considered in few studies only (Dalai et al., 2020; Shen et al., 2020; Kuan et al., 2019; Stoeckl et al., 2016; Sriapai et al., 2012). However, none of these studies had quantified the effect of beach slope on the *Saltwater-freshwater Interface* movement in porous media. Walther et al. (2017) presented a numerical investigation to qualitatively comment on the saltwater-freshwater mixing zone shift under beach slope variation. The current study focuses on quantification of impact of beach slope variation on *Saltwater-freshwater Interface* movement in unconfined configuration under static and tidal saltwater side boundary conditions. Physical experiment, numerical analysis, image analysis and analytical solution were utilized for quantitative and qualitative analysis.

3.1 Influence of Beach Slope on Saltwater Movement in Single Layer Under Static Condition

The laboratory experiments were carried out with Grade I (1-2 *mm*) Indian Standard Sand (IS: 650-1991; Manufactured by Tamilandu Minerals Limited) with varying beach slope to understand the saltwater dynamics in single (homogeneous) layered porous media under static saltwater boundary conditions. The experimental configurations are presented in Table 3.1. Experiments also included the study of flow circulation in freshwater zone within the porous media.

Table 3.1: Configurations for Experiments with Single Layered Porous Media Under Static Saltwater Side Boundary Condition

Cases	Beach Slope	Sand	Stratification	Tidal/ Static	Remarks
$CASE-3A/S$	15^0	Grade I IS Sand $d_{50} = 1.12\ mm$	No	Static	-
$CASE-3B/S$	20^0	Grade I IS Sand $d_{50} = 1.12\ mm$	No	Static	-
$CASE-3C/S$	25^0	Grade I IS Sand $d_{50} = 1.12\ mm$	No	Static	-
$CASE-3D/S$	30^0	Grade I IS Sand $d_{50} = 1.12\ mm$	No	Static	-

3.1.1 Experimental Method

Experiments were carried with the *Sand Box Model* described in *Section* ??. Same experimental steps were followed to obtain pressure head data under static saltwater boundary condition. Figure 3.1 shows the experimental setup. *Grade-I IS Sand* was used as the aquifer medium in the middle part of the *Sand Box Model* ($ZoneB$). In the present study, six pressure transducers ($PS1$, $PS2$, $PS3$, $PS4$, $PS5$, and $PS6$) were connected through 8 *mm* diameter openings of the back side glass wall for taking pressure measurements. Pressure measurements and images were recorded until the saltwater-freshwater interface reached the quasi steady state condition. Four cases with different slopes (15°, 20°, 25°, 30°) were considered (Figures 3.2, 3.3, 3.4 and 3.5). The salinity in the saltwater reservoir was

Initial fluctuations of the pressure values??

continuously monitored as mentioned in *Section* **??** using a CTD Diver (Figure **??**). Initial fluctuations were observed due to initial saltwater-freshwater mixing in the *Sand Box Model*. Approximately 35000 mg/l saltwater concentration was maintained in *Zone A* after initial period (Figures 3.6a, 3.6b, 3.6c, and 3.6d). The measurements for density dependent flow experiments were recorded only after stabilisation of the salinity measurements. Figure 3.6 shows the starting point for different experimental cases. The experiments ($CASE-3A/S$, $CASE-3B/S$, $CASE-3C/S$, and $CASE-3D/S$) were continued for 12 h to 15 h.

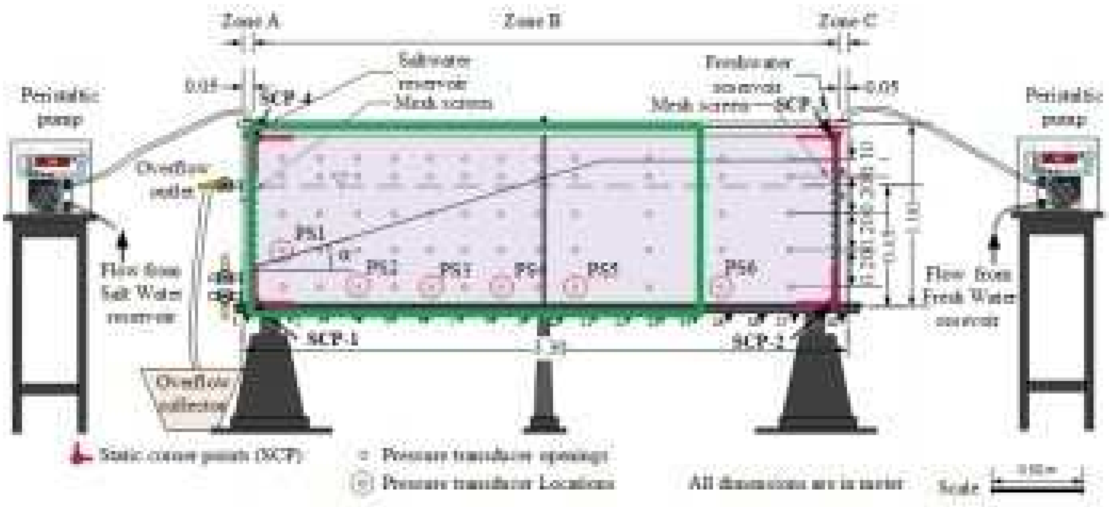

Figure 3.1: Schematic Representation Experimental Setup with Single Layered Porous Media Under Static Saltwater Side Boundary Condition

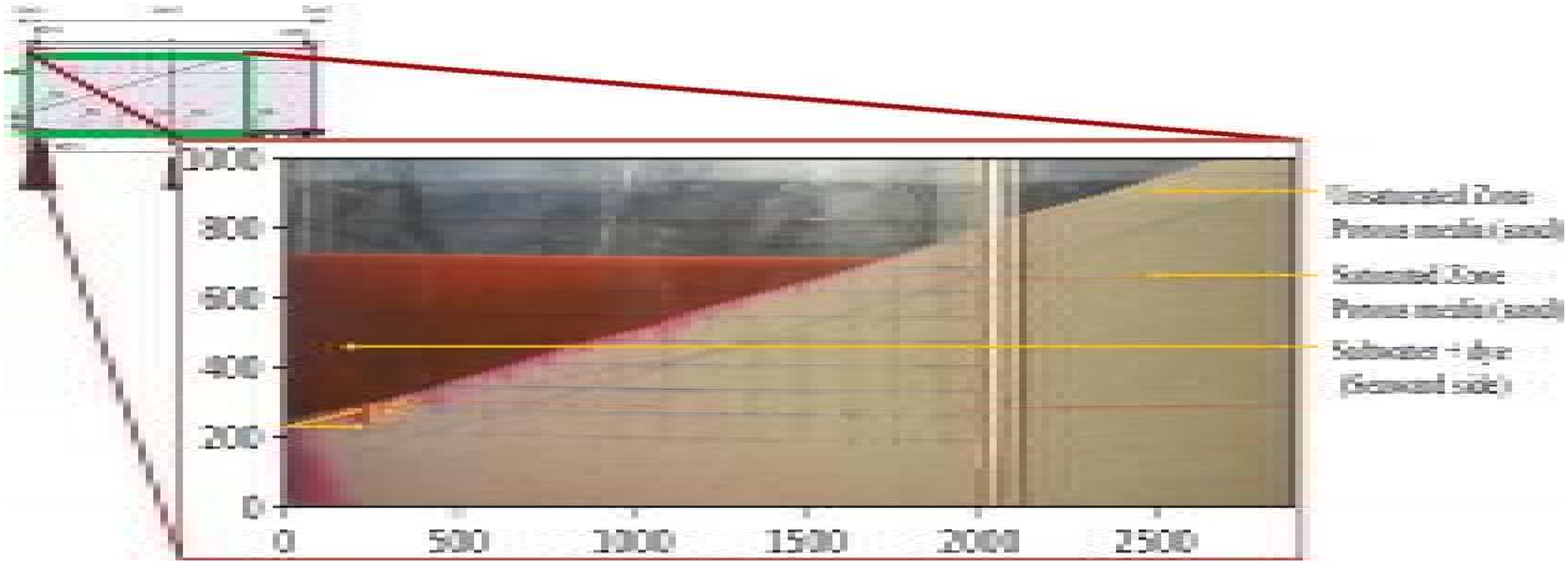

Figure 3.2: Green Rectangular Box and Experimental Beach Slope for $CASE-3A/S$

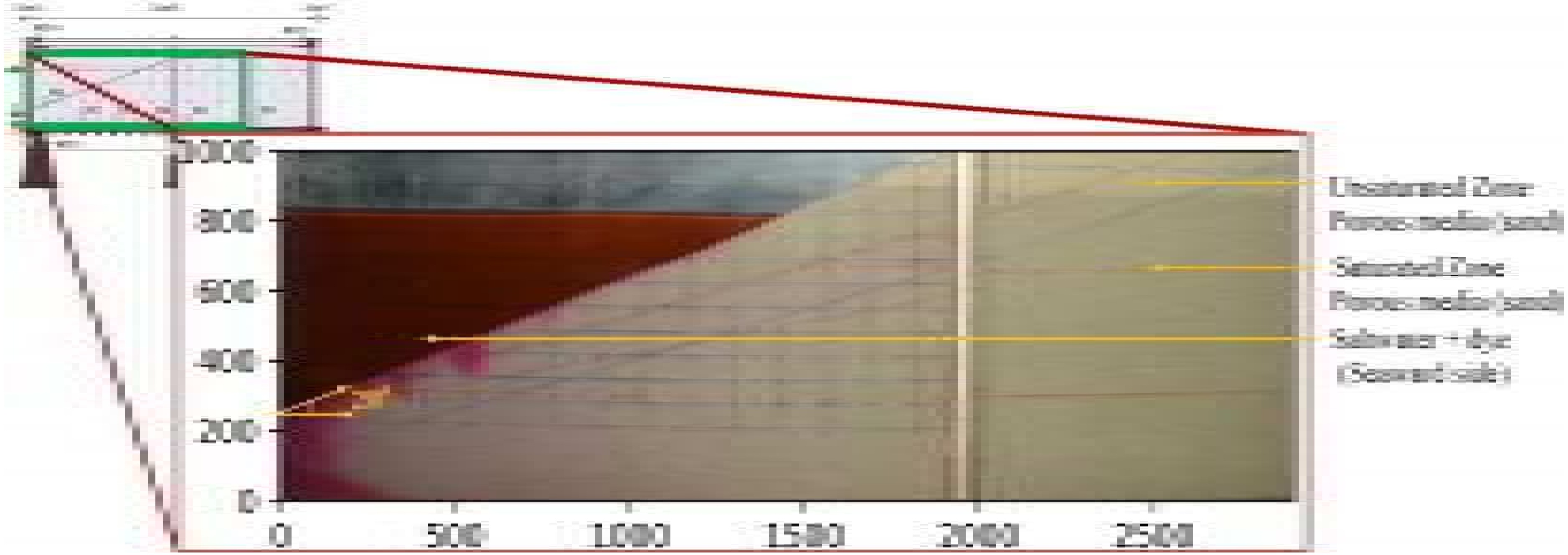

Figure 3.3: Green Rectangular Box and Experimental Beach Slope for $CASE-3B/S$

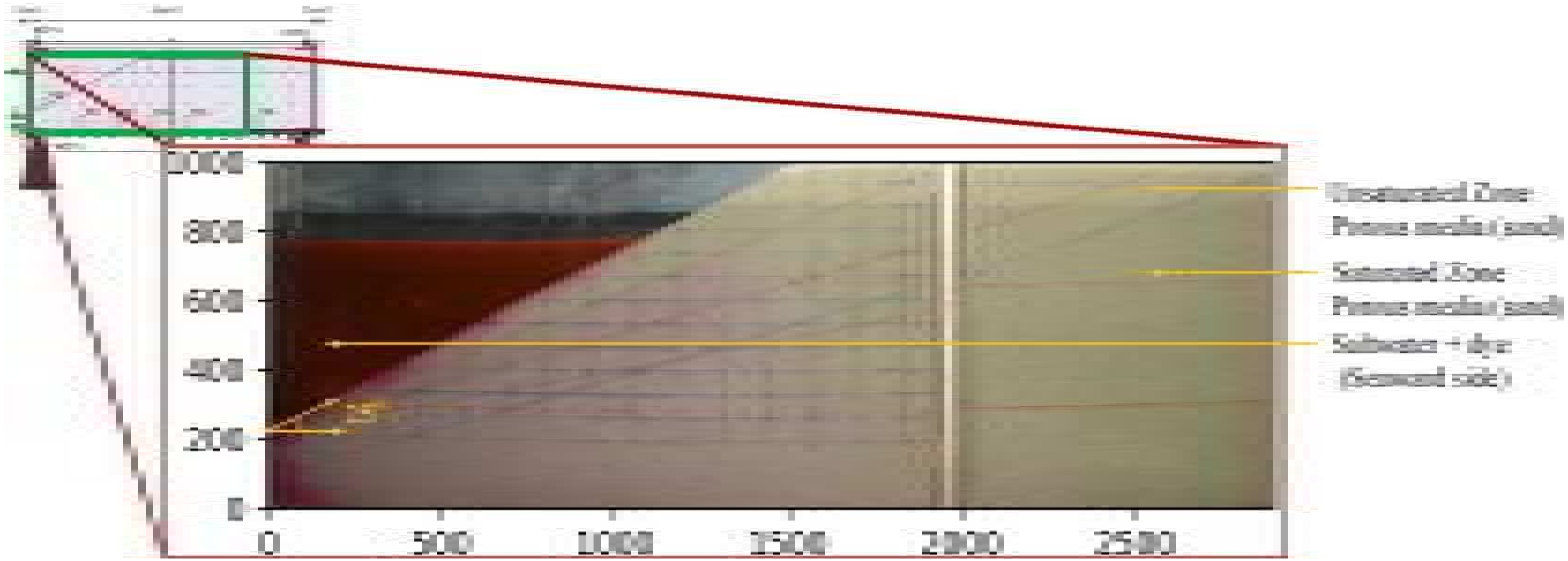

Figure 3.4: Green Rectangular Box and Experimental Beach Slope for $CASE-3C/S$

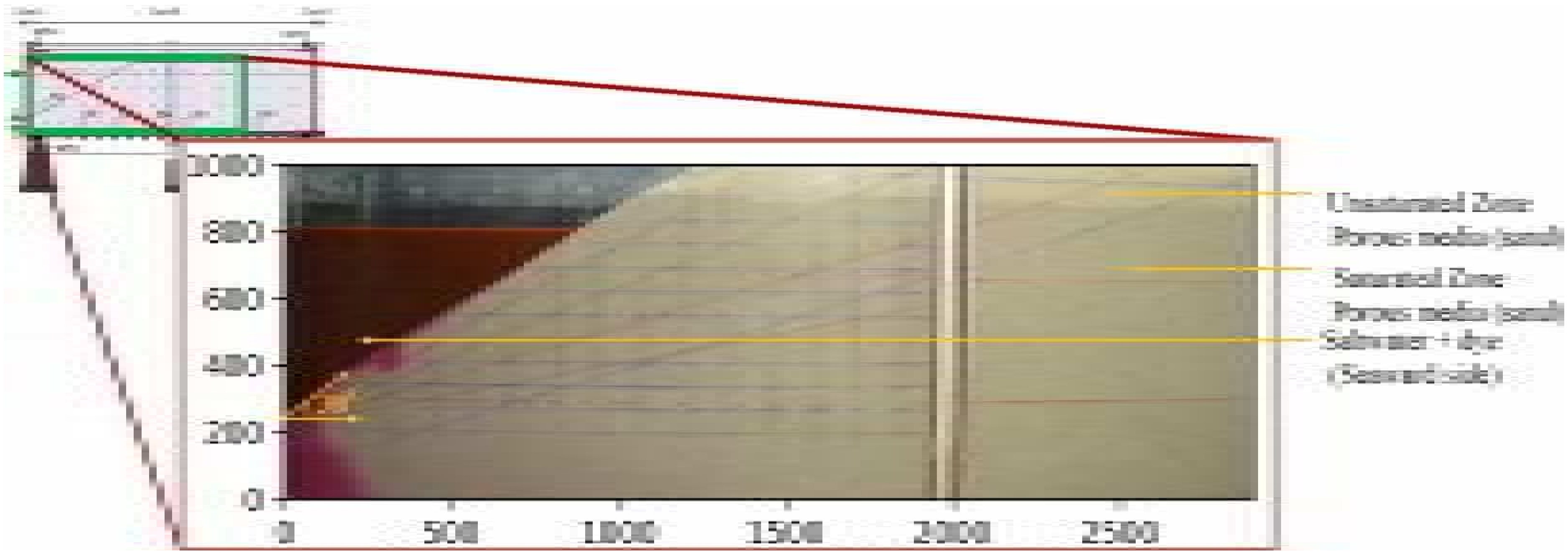

Figure 3.5: Green Rectangular Box and Experimental Beach Slope for $CASE - 3D/S$

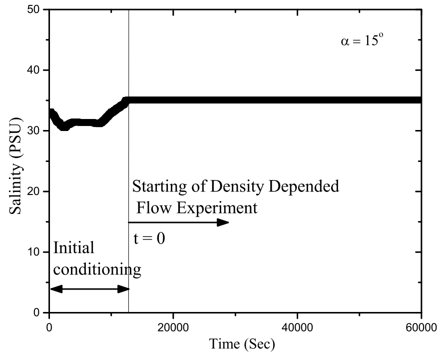

(a) $CASE-3A/S$

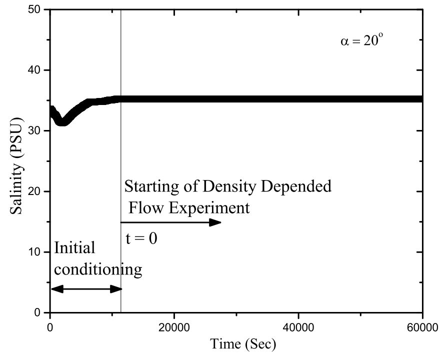

(b) $CASE-3B/S$

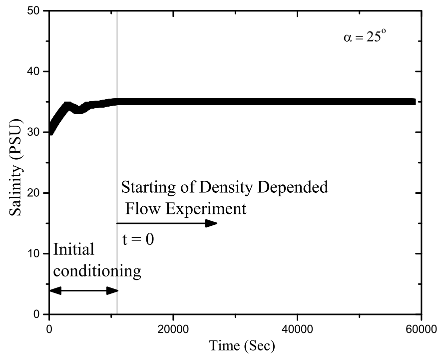

(c) $CASE-3C/S$

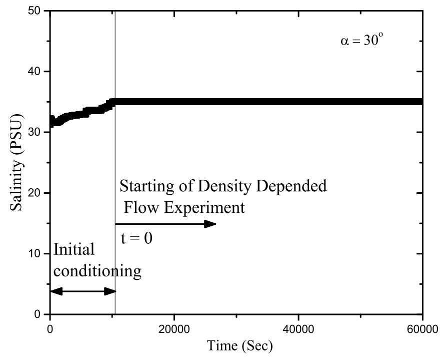

(d) $CASE-3D/S$

Figure 3.6: Observed Time Varying Salinity Profiles at Saltwater Reservoir ($Zone-A$)

3.1.2 Numerical Simulation Model

The laboratory scale experiments and the numerical simulation model were used to produce a series of data sets (pressure head and concentration) at different time levels. Numerical simulations in two-dimensional vertical cross-section were performed using the finite-element based model FEFLOW (Diersch, 2013). The governing equations for variably saturated flow and transport are presented in *Section* **??**. Unstructured finite element mesh of different sizes were utilized to discretize the *Sand Box Model* for four cases. Mesh convergence study was performed with finer and coarser spatial discretizations. The optimal element size varies from 0.001 m to 0.004 m. Initial and boundary Conditions were specified as per the *Subsection* **??**. Details of boundary conditions are shown in Figure 3.7. The flow and transport simulations were performed with a longitudinal dispersivity value of 0.004 m (of the order of the average grain diameter). The transverse dispersivity value was assumed to be 1/10 of the longitudinal dispersivity Welty and Gelhar (1994). Molecular diffusion, fluid viscosity, and the relative permeability function values were assigned on the basis of commonly reported estimates appearing in the literature (Liu et al., 2016). The effective diffusivity (the product of free water diffusivity and tortuosity) of the *Rhodamine B* was numerically fitted. The difference in diffusion coefficients for salt constituents and *Rhodamine B* was neglected. Thus *Rhodamine B* was safely used to delineate the saltwater region within the porous media. The individual cases were calibrated against the experimental results by varying the parameters. Numerical parameter values are present in Table 3.2.

Table 3.2: Numerical Parameters Used for Experiments with Single Layered Porous Media Under Static Saltwater Side Boundary Condition

Parameters	**Symbols**	**Value**	**Unit**
Horizontal Length	L	3.1	m
Domain thickness	H	1.0	m
Porosity	ϵ	0.35	-
Saltwater level	h_f	0.66	m
Freshwater density	ρ_0	1000	kg/m^3
Saltwater density	ρ_s	1025	kg/m^3
Saltwater concentration	C_s	35	kg/m^3
Longitudinal dispersivity	β_L	0.004	m
Transverse dispersivity	β_T	0.0004	m
Molecular diffusion coefficient	D	10^{-9}	m^2/s
Density Ratio	χ	0.025	-
Hydraulic conductivity	K	600	m/d

3.1.3 G-Channel Based Image Analysis

Instantaneous movement of saltwater was visually captured at an interval of 2 s by a Digital Single-Lens Reflex (DSLR) camera (Nikon $d5100$) placed centrally in front of the Sand Box Model ($Zone\ B$). Lighting arrangements were kept same as of $CASE-1/S$ and $CASE-2/S$. A virtual green rectangular box was utilized as a reference frame for the experimental images (Figures 3.2, 3.3, 3.4, 3.5). Portions of the experimental images were used as raw images (input) for further analysis. At beginning, the captured images were cropped to fit the virtual green rectangular box. Raw images corresponding to all time periods ($\mathbf{Im_{Raw}|_t}$) were aligned with respect to common coordinate system. Saltwater-freshwater interface movement information was extracted at a particular time by comparing the image with the reference image ($\mathbf{Im_{Raw}|_{t_0}}$).

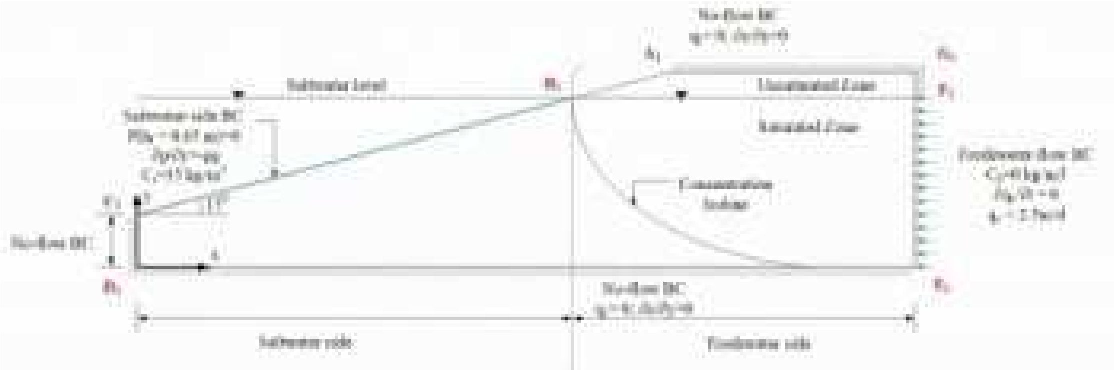

(a) $CASE-3A/S$

(b) $CASE-3B/S$

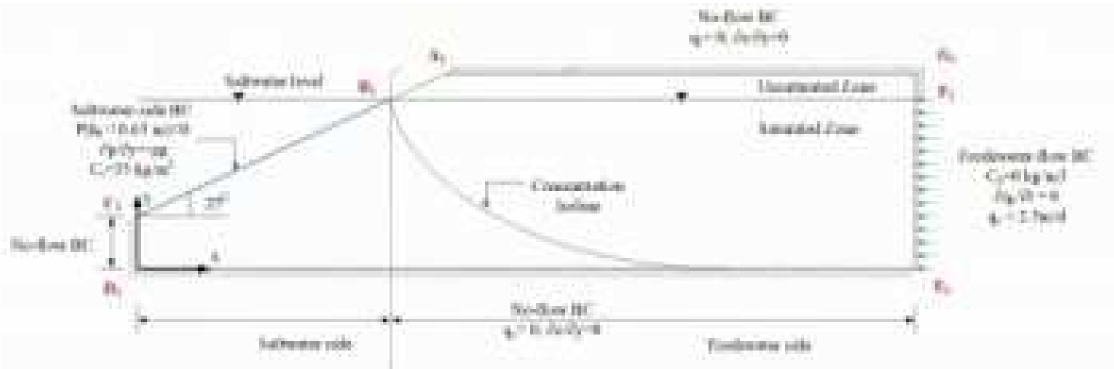

(c) $CASE-3C/S$

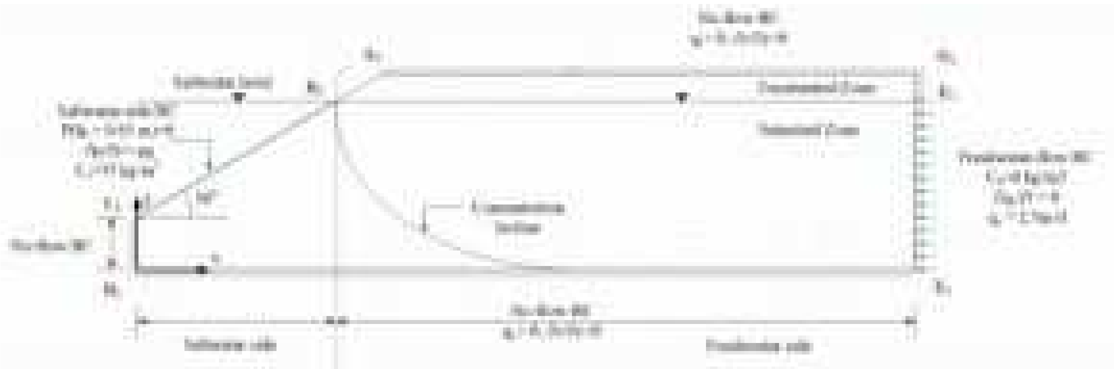

(d) $CASE-3D/S$

Figure 3.7: Boundary Conditions Used in Numerical Simulation for Experiments with Single Layered Porous Media Under Static Saltwater Side Condition

Experimental images contained colour information (pixel level) of i) unsaturated sand, ii) saturated sand, ii) *Rhodamine B* (tracer) mixed saltwater, iv) saltwater mixed sand. A robust image analysis technique was utilized for extraction of concentration gradient information. Image ($\mathbf{Im_{Raw}|_t}$) corresponding to a particular time (t) stores colour (R-G-B) information (Figure **??**) in pixels ($p_y \times p_x \times 3$). A colour can be regarded as a mixture of basic colours, viz. Red (R), Green (G), Blue (B) with different Digital Number (DN) values (between 0-255). Individual images can be decomposed into three different $2D$ ($p_y \times p_x$) matrices ($\mathbf{Im^R_{Raw}|_t}$, $\mathbf{Im^G_{Raw}|_t}$, $\mathbf{Im^B_{Raw}|_t}$) corresponding to Red, Green and Blue colours, respectively. The basic image analysis technique, proposed in *Section* **??**, utilized difference between Red and Green DN values for extracting concentration gradient information. In-depth image analysis revealed that same DN value difference corresponds to multiple combinations of Red and Green channel values. Comparative analysis of different channels (R-G-B) showed that DN value standard deviation was maximum for Green Channel (G-Channel). Modeling of G Channel ($\mathbf{Im^G|_t}$) as a spatial process revealed physically consistent pattern near saltwater boundary corresponding to different pixel locations. However, variation in spatial pattern within the intermediate domain required a special attention. The proposed algorithm identifies spatial patterns on the basis of threshold DN value differences (between t and t_0). This was achieved by G-channel matrix subtraction ($\mathbf{Im^G_t} = \mathbf{Im^G_{Raw}|_t}$ - $\mathbf{Im^G_{Raw}|_{t_0}}$). A typical instantaneous and reference images ($p_y = 243 \times p_x = 800$) are shown in Figure 3.8b and Figure 3.8a, respectively. Figure 3.8c shows the output of G-Channel matrix subtraction.

Pixel level information (DN value difference) obtained from G-channel matrix subtraction was utilized for identification of concentration isolines. Line joining pixels with equal threshold DN level showed too much variation. Figure 3.9a shows raw saltwater-freshwater interface. Statistical mean value cannot be utilized for filtering out fluctuations. Winsorized statistical mean is less sensitive to outliers. It eliminates an equal amount of both extremes and 10% to 25% values are replaced (Hastings et al., 1947). Saltwater-freshwater interface fluctuations were filtered (Figure 3.9b) by using 10% Winsorized Mean ($\mathcal{WM}$) based on neighbouring pixels of i $\left(.., \mathbf{Im^G_t}|_{i-1,j}, \mathbf{Im^G_t}|_{i,j}, \mathbf{Im^G_t}|_{i+1,j}, ..\right)$ present at level j. The framework utilized threshold DN values (DN_{Max} and DN_{Min}) corresponding to maximum and minimum concentration levels (c_{Max} and c_{Min}). Thresholds were fixed based on image statistics. For pixels (Set $\mathbb{Z}_{SWB}$) corresponding to saltwater boundary maximum concentration value (c_{Max}) was specified. Similarly, 0.5 concentration isoline value (c_{Min}) was specified for the pixels (Set $\mathbb{Z}_{SFI}$) present in saltwater-freshwater interface. Concentration gradient information ($\mathbf{Im^c_{Grad}}$) for intermediate zone was obtained from an order statistics based linear interpolation method. Given two sets of concentration information points (DN_{Max}, c_{Max}) and

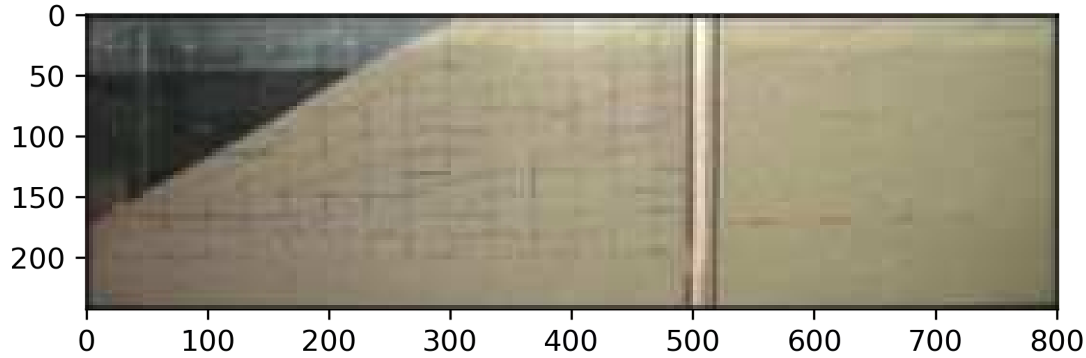

(a) $\mathbf{Im_{Raw}}|_{\mathbf{t_0}}$

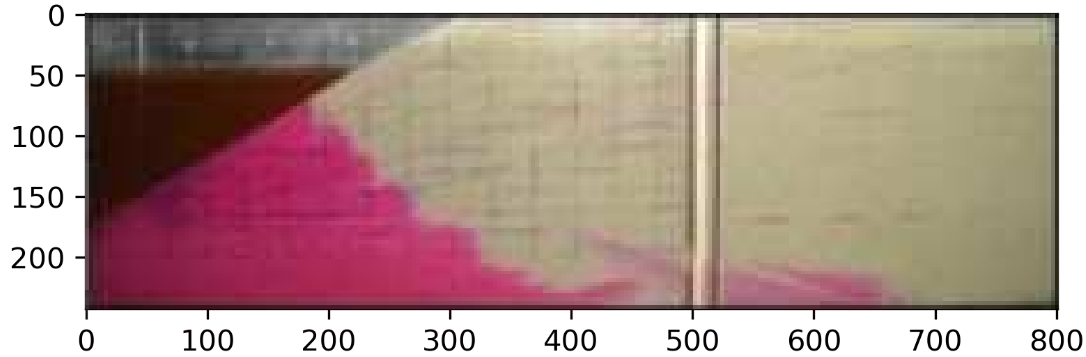

(b) $\mathbf{Im_{Raw}}|_{\mathbf{t}}$

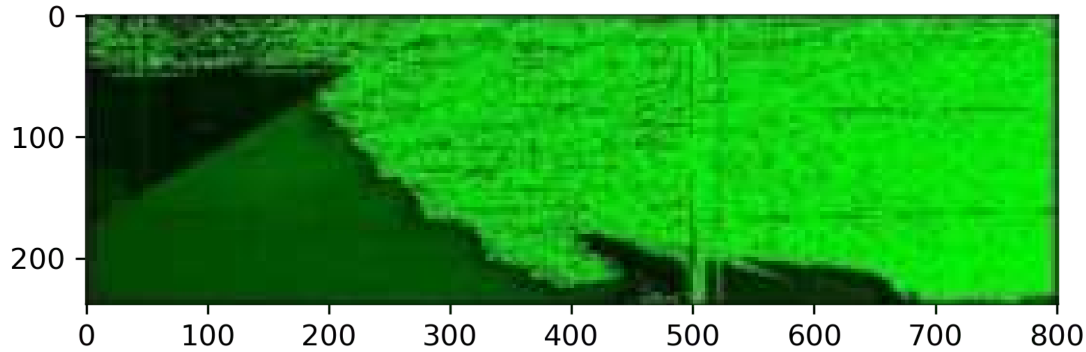

(c) $\mathbf{Im^G}|_{\mathbf{t}}$

Figure 3.8: Detailed Steps of G-Channel Matrix Substraction

$(DN_{Min},\ c_{Min})$, a linear polynomial can be constructed as

$$\ell(\mathbf{Im_t^G}|_{i,\ j}) = \frac{\mathbf{Im_t^G}|_{i,\ j} - DN_{Min}}{DN_{Max} - DN_{Min}} c_{Max} + \frac{\mathbf{Im_t^G}|_{i,\ j} - DN_{Max}}{DN_{Min} - DN_{Max}} c_{Min} \tag{3.1}$$

$\ell(\mathbf{Im_t^G}|_{i,\ j})$ interpolates the concentration (c) value for pixel $(i,\ j)$ in intermediate zone. Concentration gradient information matrix can be calculated as

$$\mathbf{Im^c_{Grad}}|_{i,\ j} = \ell(\mathbf{Im_t^G}|_{i,\ j}) \tag{3.2}$$

Figure 3.9c shows derived concentration distribution within the saltwater wedge within the porous media. The proposed G-Channel Based Image Analysis framework is presented in Algorithm 1. A python code was written to implement the proposed algorithm.

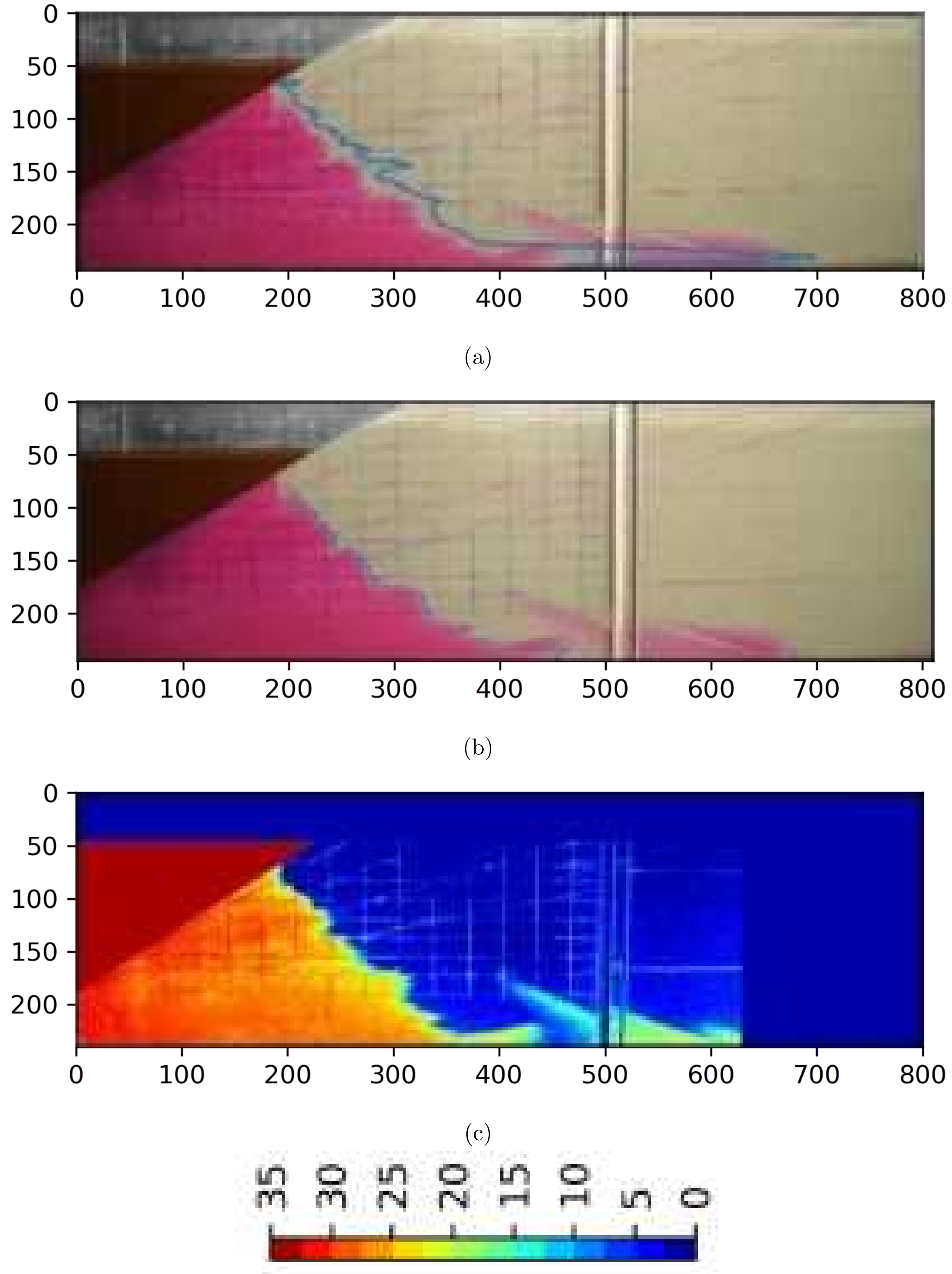

Figure 3.9: Detailed Steps of G-Channel Based Image Analysis: (a) Identification of Saltwater-Freshwater Interface, (b) Filtered Saltwater-Freshwater Interface Obtained from 10% Winsorized Mean , (c) Concentration Distribution

3.1.4 Results and Discussion

Saltwater-freshwater interface dynamics in single layer was studied for four different beach slopes ($\alpha =, 15°, 20°, 25°, 30°$) under static saltwater water level condition. The study quantified the influence of beach slope on saltwater dynamics in porous media. Laboratory-Scale numerical simulations was also utilized to assess the consistency of the experimental results.

Physical experiments, numerical simulations, experimental image analysis, and analytical solution were utilized for comprehensive analysis. Time varying saltwater intrusion flow pattern from experiments, G-Channel based image analysis and numerical simulations (0.5-concentration isoline) are shown in Figures 3.10, 3.11, 3.12, 3.13. Saltwater-freshwater interface and concentration distribution were analyzed corresponding to $t = 600\ s$, $t = 2100\ s$, $t = 7320\ s$, $t = 25800\ s$. Saltwater-freshwater interfaces are clearly visible for the $CASE - 3A/S$, $CASE - 3B/S$, $CASE - 3C/S$, $CASE - 3D/S$. Reasonable match of experiment, image analysis and numerical simulation results were obtained for all the cases. Due to diffusive nature of the saltwater-freshwater interface only visual matching technique was utilized. Interface toe location was used as key matching parameter. Numerically simulated interface toe location reasonably matched with the experimental one.

Fingering effect is prominent in $CASE - 3A/S$ for 15° slope. Effect is still visible for $CASE - 3B/S$ for 20° slope. It is evident that initial saltwater fingering effect reduces with the increase in beach slope. However, the numerical simulation results captured the local fingering effect partially. This was due the scale (mesh size) considered during the numerical simulations. Finer mesh would give a better fingering effect. However, finer mesh was not used as our focus was on developed saltwater-freshwater interface. Saltwater intrusion occurred rapidly, i.e., size of the saltwater wedge increases, for flatter slopes ($CASE - 3A/S$). Thus saltwater-freshwater interface intruded less in $CASE - 3D/S$. Both experimental and numerical solutions showed similar trends. Moreover, time required to reach the quasi-steady condition was less in $CASE - 3A/S$. It increases with the increase in beach slope. Overall influence of slope is evident from the aforementioned analysis.

Algorithm 1: G-Channel Based Image Analysis

Input: $\mathbf{Im_{Raw}}|_{\mathbf{t_0}}$, $\mathbf{Im_{Raw}}|_{\mathbf{t}}$

Output: $\mathbf{Im^{c}_{Grad}}$

Reference Image Decomposition
$\mathbf{Im_{Raw}}|_{\mathbf{t_0}} \rightarrow [\mathbf{Im^{R}_{Raw}}|_{\mathbf{t_0}}, \mathbf{Im^{G}_{Raw}}|_{\mathbf{t_0}}, \mathbf{Im^{B}_{Raw}}|_{\mathbf{t_0}}]$
while $t < T_{max}$ **do**
    Image Decomposition
    $\mathbf{Im_{Raw}}|_{\mathbf{t}} \rightarrow [\mathbf{Im^{R}_{Raw}}|_{\mathbf{t}}, \mathbf{Im^{G}_{Raw}}|_{\mathbf{t}}, \mathbf{Im^{B}_{Raw}}|_{\mathbf{t}}]$
    G-channel Matrix Subtraction
    $\mathbf{Im^{G}_{t}} \leftarrow \mathbf{Im^{G}_{Raw}}|_{\mathbf{t}}$ - $\mathbf{Im^{G}_{Raw}}|_{\mathbf{t_0}}$
    for j=1 *to* p_y **do**
        for i= 1 *to* p_x **do**
            Winsorized Mean Calculation
            $\mathcal{WM} \leftarrow WinsorizedM\left(.., \mathbf{Im^{G}_{t}}|_{i-1,j}, \mathbf{Im^{G}_{t}}|_{i,j}, \mathbf{Im^{G}_{t}}|_{i+1,j}, ..\right)$
            Saltwater Boundary Identification
            if $\mathcal{WM} > \mathbf{DN_{Max}}$ **then**
                $\mathbb{Z}_{SWB} \leftarrow$ (i, j)
                break
            end
        end
        for i= 1 *to* p_x **do**
            Winsorized Mean Calculation
            $\mathcal{WM} \leftarrow WinsorizedM\left(.., \mathbf{Im^{G}_{t}}|_{i-1,j}, \mathbf{Im^{G}_{t}}|_{i,j}, \mathbf{Im^{G}_{t}}|_{i+1,j}, ..\right)$
            Saltwater-Freshwater Interface Identification
            if $\mathcal{WM} < \mathbf{DN_{Min}}$ **then**
                $\mathbb{Z}_{SFI} \leftarrow$ (i, j)
                break
            end
        end
    end
    Concentration for Saltwater Boundary
    for *each* $(i,\ j) \in \mathbb{Z}_{SWB}$ **do**
        $\mathbf{Im^{c}_{Grad}}|_{i,\ j} \leftarrow c_{Max}$
    end
    Concentration for Saltwater-Freshwater Interface
    for *each* $(i,\ j) \in \mathbb{Z}_{SFI}$ **do**
        $\mathbf{Im^{c}_{Grad}}|_{i,\ j} \leftarrow c_{Min}$
    end
    Concentration for Intermediate Zone
    for j=1 *to* p_y **do**
        for i= 1 *to* p_x **do**
            if $(i,\ j) \notin \mathbb{Z}_{SWB}$ *and* $(i,\ j) \notin \mathbb{Z}_{SFI}$ **then**
                $\mathbf{Im^{c}_{Grad}}|_{i,\ j} = \ell(\mathbf{Im^{G}_{t}}|_{i,\ j})$
            end
        end
    end
end while

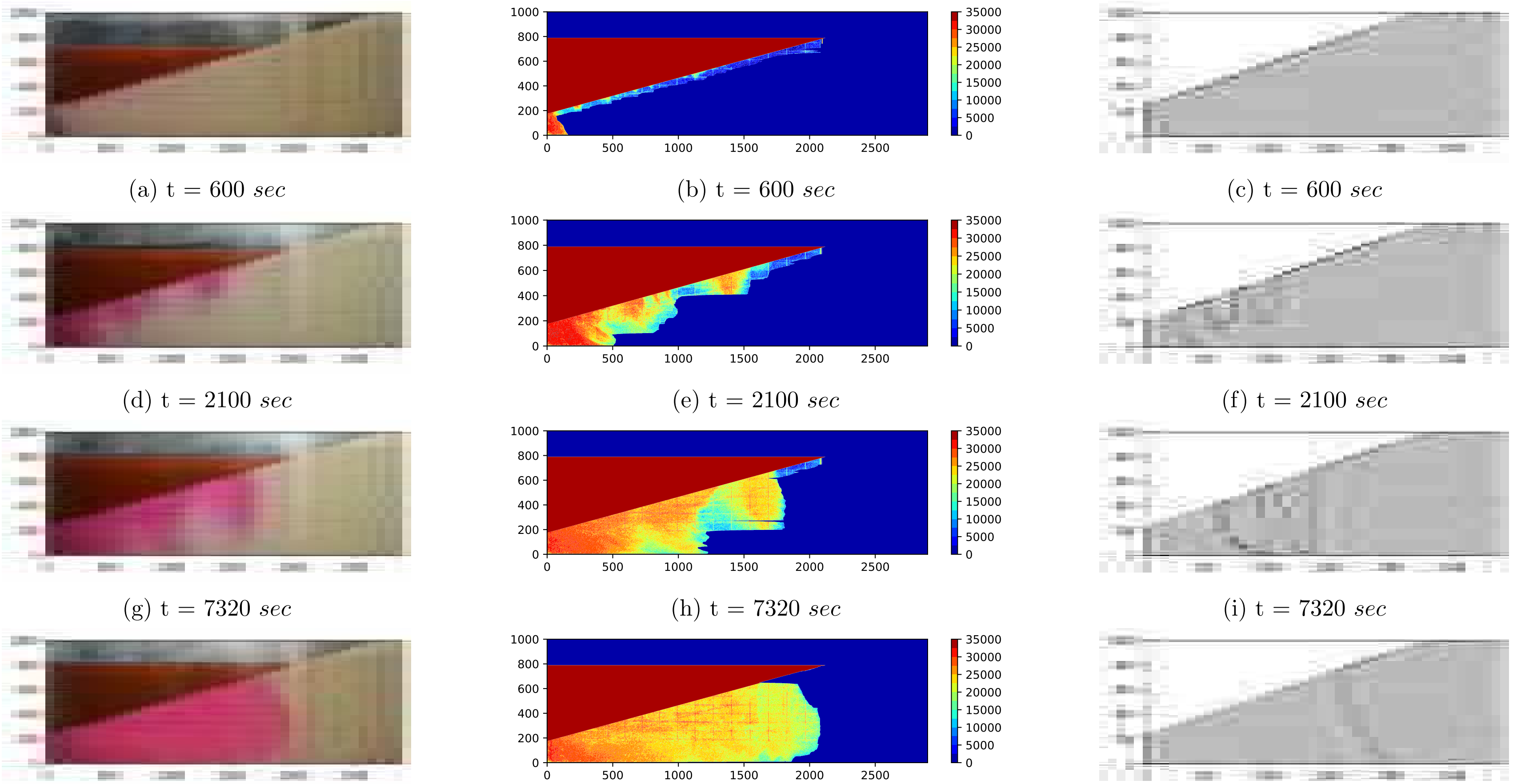

(a) t = 600 sec (b) t = 600 sec (c) t = 600 sec

(d) t = 2100 sec (e) t = 2100 sec (f) t = 2100 sec

(g) t = 7320 sec (h) t = 7320 sec (i) t = 7320 sec

(j) t = 25800 sec (k) t = 25800 sec (l) t = 25800 sec

Figure 3.10: Development of Saltwater Wedge with Time in $CASE-3A/S$ [First Column: Experimental Images; Second Column: Output of G-Channel Based Image Analysis; Third Column: Numerical Simulation (0.5-Concentration Isoline), The Color Maps Indicate Concentration]. All dimensions are in mm.

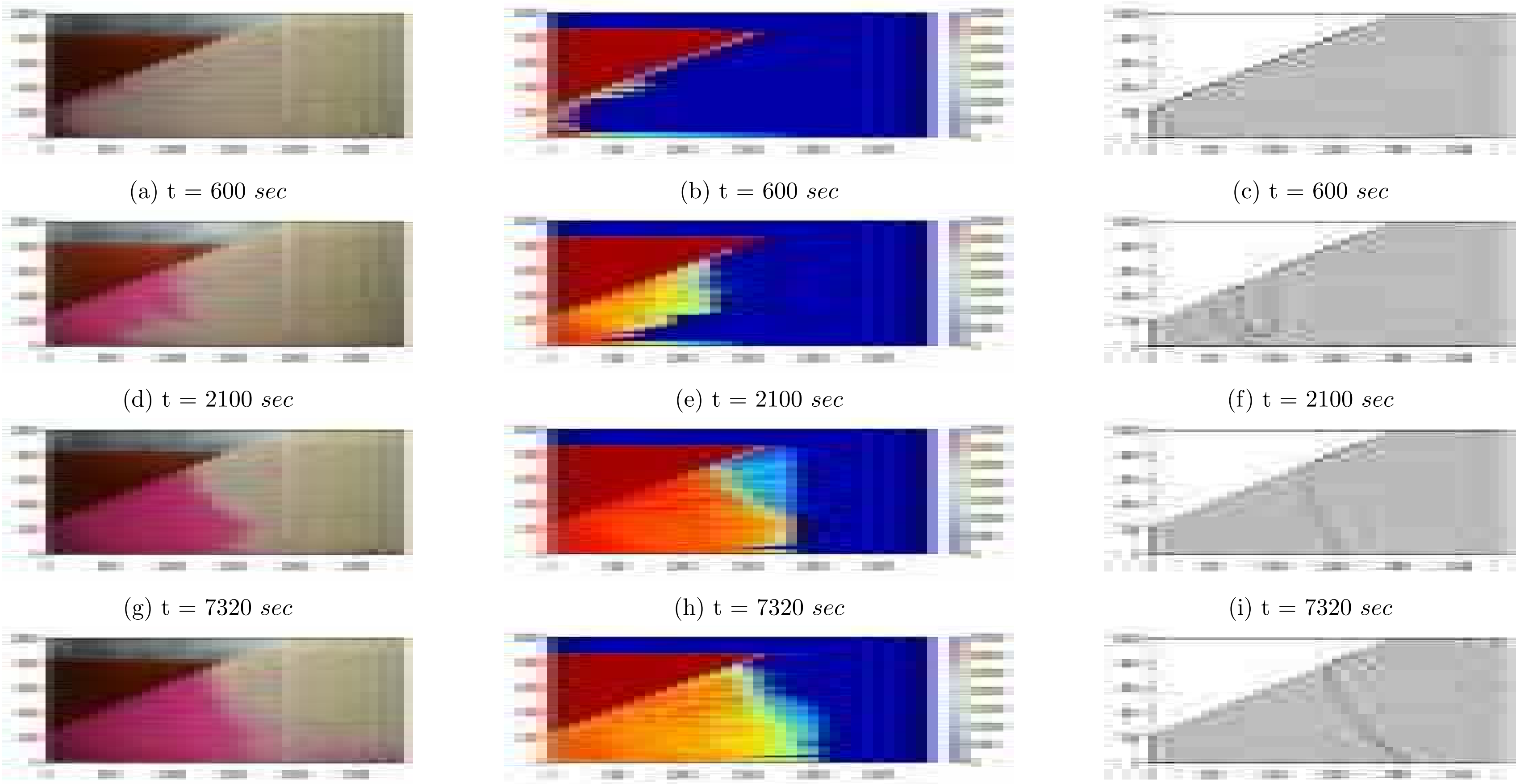

(a) t = 600 *sec* (b) t = 600 *sec* (c) t = 600 *sec*

(d) t = 2100 *sec* (e) t = 2100 *sec* (f) t = 2100 *sec*

(g) t = 7320 *sec* (h) t = 7320 *sec* (i) t = 7320 *sec*

(j) t = 25800 *sec* (k) t = 25800 *sec* (l) t = 25800 *sec*

Figure 3.11: Development of Saltwater Wedge with Time in $CASE - 3B/S$ [First Column: Experimental Images; Second Column: Output of G-Channel Based Image Analysis; Third Column: Numerical Simulation (0.5-Concentration Isoline), The Color Maps Indicate Concentration]. All dimensions are in mm.

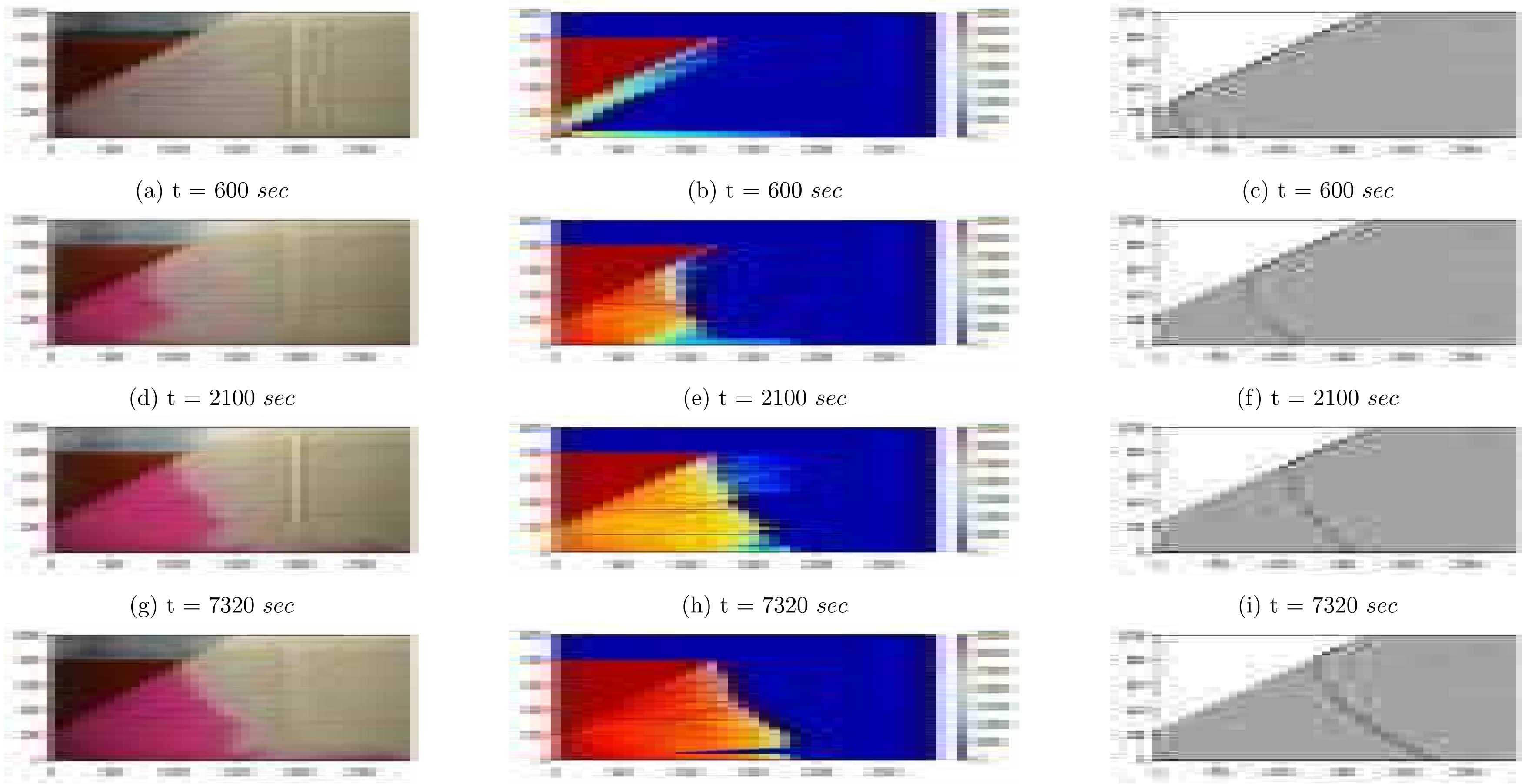

(a) t = 600 sec (b) t = 600 sec (c) t = 600 sec

(d) t = 2100 sec (e) t = 2100 sec (f) t = 2100 sec

(g) t = 7320 sec (h) t = 7320 sec (i) t = 7320 sec

(j) t = 25800 sec (k) t = 25800 sec (l) t = 25800 sec

Figure 3.12: Development of Saltwater Wedge with Time in $CASE-3C/S$ [First Column: Experimental Images; Second Column: Output of G-Channel Based Image Analysis; Third Column: Numerical Simulation (0.5-Concentration Isoline), The Color Maps Indicate Concentration]. All dimensions are in mm.

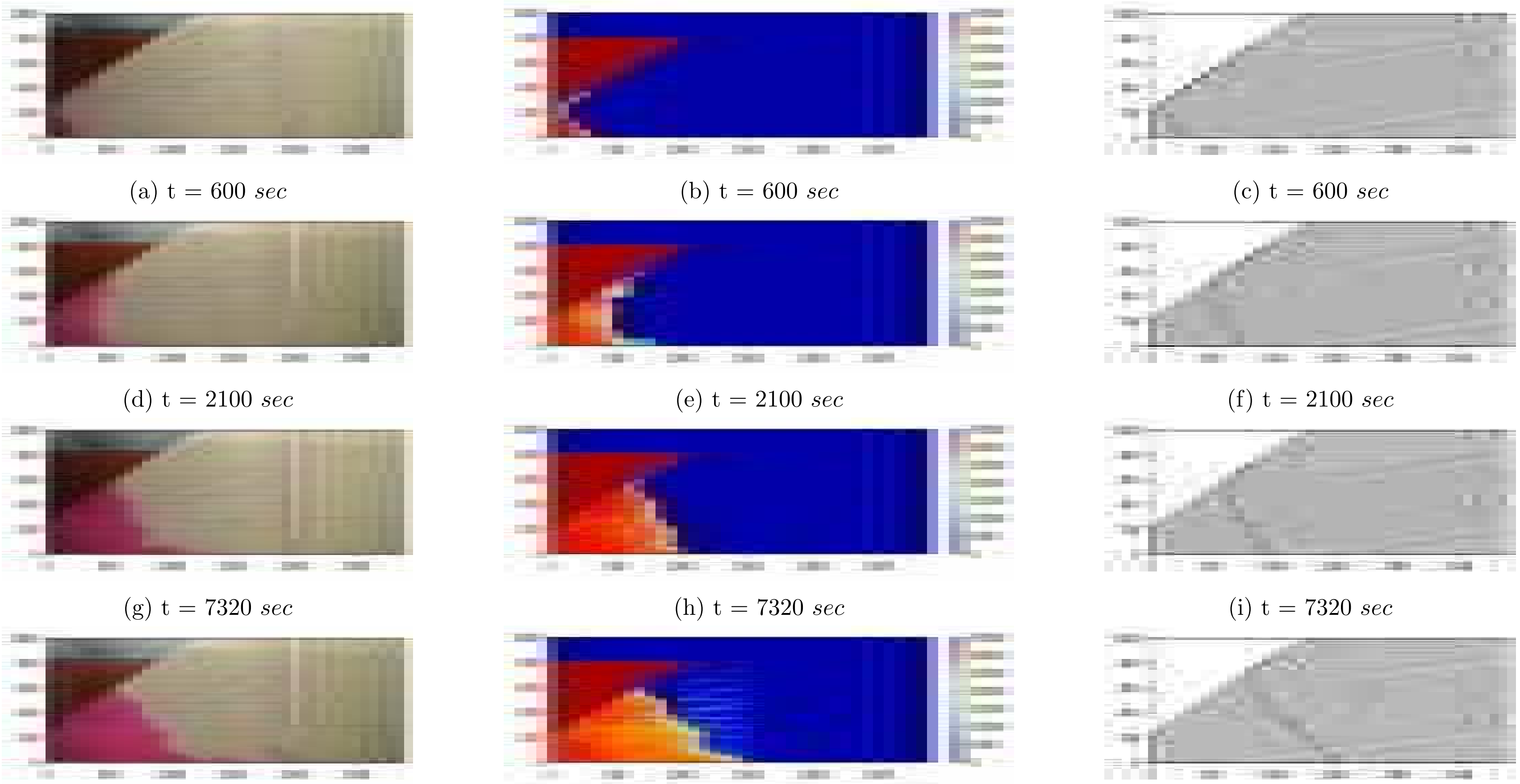

(a) t = 600 *sec* (b) t = 600 *sec* (c) t = 600 *sec*

(d) t = 2100 *sec* (e) t = 2100 *sec* (f) t = 2100 *sec*

(g) t = 7320 *sec* (h) t = 7320 *sec* (i) t = 7320 *sec*

(j) t = 25800 *sec* (k) t = 25800 *sec* (l) t = 25800 *sec*

Figure 3.13: Development of Saltwater Wedge with Time in $CASE-3D/S$ [First Column: Experimental Images; Second Column: Output of G-Channel Based Image Analysis; Third Column: Numerical Simulation (0.5-Concentration Isoline), The Color Maps Indicate Concentration]. All dimensions are in mm.

Further numerically simulated and experimental (Pore Water Pressure Measurement) hydraulic head values were plotted to check the consistency of the obtained results. Figure 3.14 shows the plots corresponding to $CASE-3A/S$, $CASE-3B/S$, $CASE-3C/S$, and $CASE-3D/S$ with a 0.5 *cm* band on both sides. The outlier clusters corresponding to different pressure transducers are clearly visible from the plots. Spatial location of pressure transducers ($PS1$, $PS2$, $PS3$, $PS4$, $PS5$, $PS6$) were fixed with respect to *Sand Box Model* for cases. In $CASE-3A/S$ all the pressure transducers showed good match except $PS2$. This was due to boundary effect as $PS2$ was located very near to the sloping boundary (15°). In $CASE-3B/S$ outlier clusters were corresponding to pressure transducers $PS3$, $PS5$, $PS6$. Pressure transducer $PS5$ was located below the junction of saltwater level and beach face (20°). Thus some effect of submarine groundwater discharge (SGD) was present. Deviation in $PS6$ was due to freshwater boundary effect. This overestimation was due to marginal rise of water level near right boundary. In $CASE-3C/S$ all the pressure transducers showed good match except $PS2$ and $PS4$. Some effect of submarine groundwater discharge (SGD) was present in $PS4$ (25°). Similarly, effect of submarine groundwater discharge (SGD) was present in $PS3$ for $CASE-3D/S$.

Comparative analysis was performed with saltwater-freshwater interface corresponding to 50%-salinity line from FEFLOW and processed images (G-Channel Based Image Analysis). Saltwater-freshwater interface toe location (l_T) and submarine groundwater discharge gap (ζ_0) were determined analytically (Equations **??** and **??**), numerically and experimentally. The analytical (Van der Veer, 1977) values of l_T and ζ_0 are 863 *mm* and 564 *mm*, respectively. The FEFLOW simulations underpredict the ζ_0 compared to the experimental value (Tables 3.3) for all the cases. SGD gap (ζ_0) decreases with increase in beach slope. Figures 3.15 show saltwater-freshwater interface variations with beach slope.

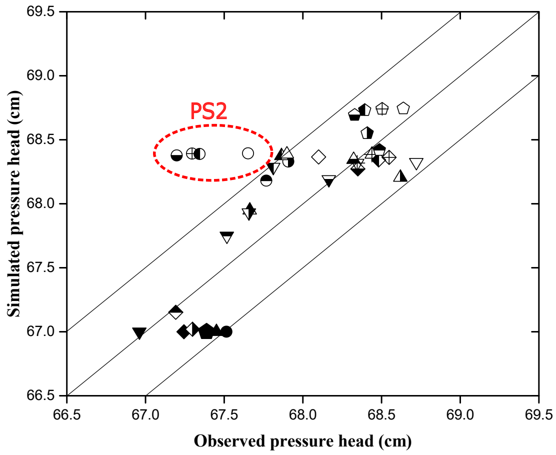

(a) $CASE-3A/S$

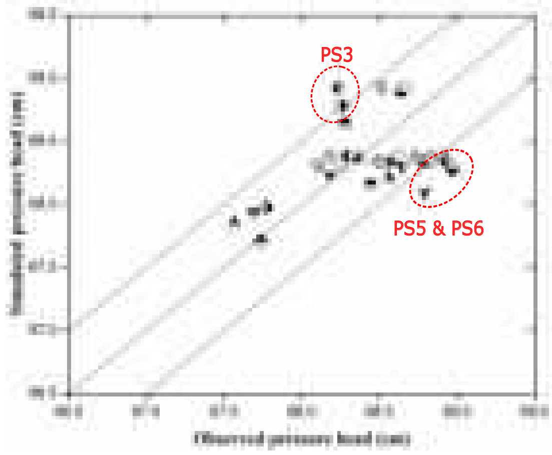

(b) $CASE-3B/S$

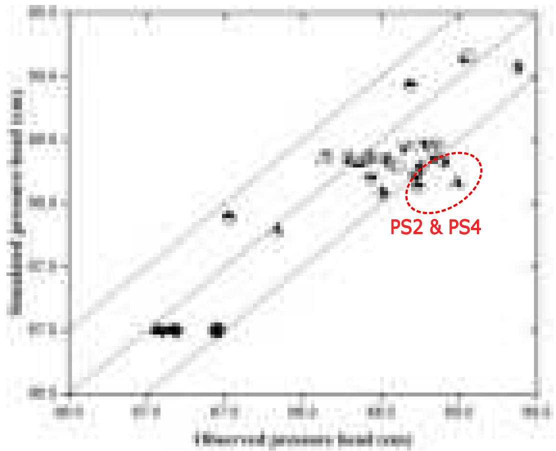

(c) $CASE-3C/S$

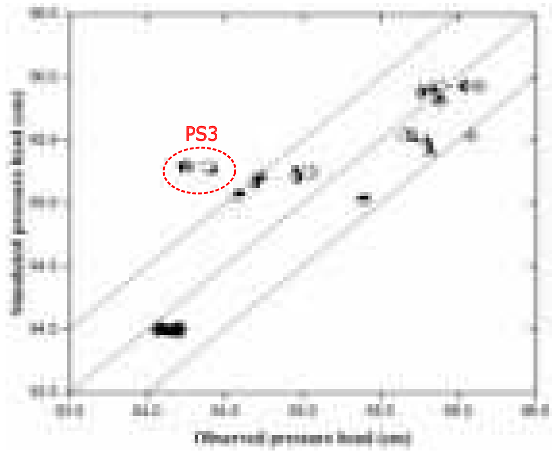

(d) $CASE-3D/S$

Figure 3.14: Comparison Between Time Varying Observed and Numerically Simulated Pressure Head Data

Table 3.3: Submarine Groundwater Discharge (SGD) Gap and Saltwater-Freshwater Interface Toe Length for Experiments with Single Layered Porous Media Under Static Saltwater Side Boundary Condition

Case	Slope	Sand	$\zeta_o(mm)$ Expt	$\ell_T(mm)$ Expt	$\zeta_o(mm)$ FEFLOW	$\ell_T(mm)$ FEFLOW	$\zeta_{o-FEFLOW}/\zeta_{o-Expt}$
$CASE-3A/S$	15^0	IS Sand Grade I d_{50}=1.12 mm	452.7	443.28	298.21	408.93	0.658
$CASE-3B/S$	20^0	IS Sand Grade I d_{50}=1.12 mm	288.81	540.80	284.78	543.02	0.986
$CASE-3C/S$	25^0	Coarse Sand d_{50}=1.12 mm	245.82	699.28	220.30	639.44	0.896
$CASE-3D/S$	30^0	Coarse Sand d_{50}=1.12 mm	241.79	816.75	188.06	609.51	0.777
							Avg= 0.82

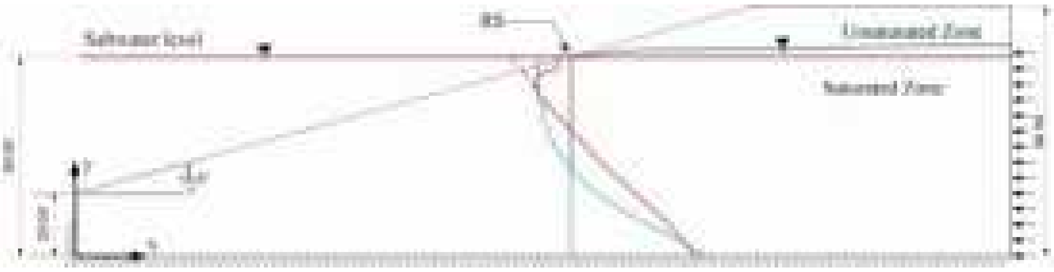

(a) $CASE - 3A/S$

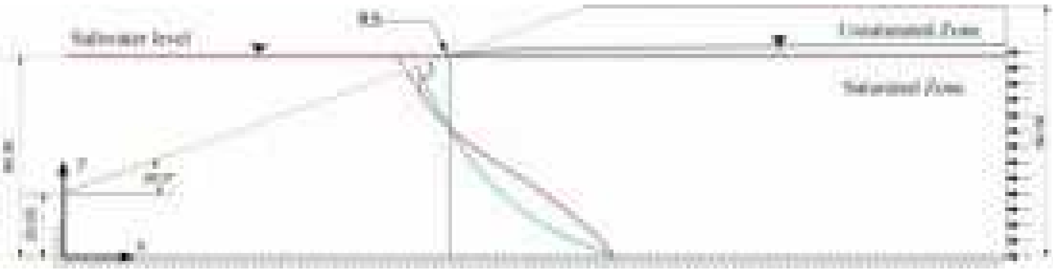

(b) $CASE - 3B/S$

(c) $CASE - 3C/S$

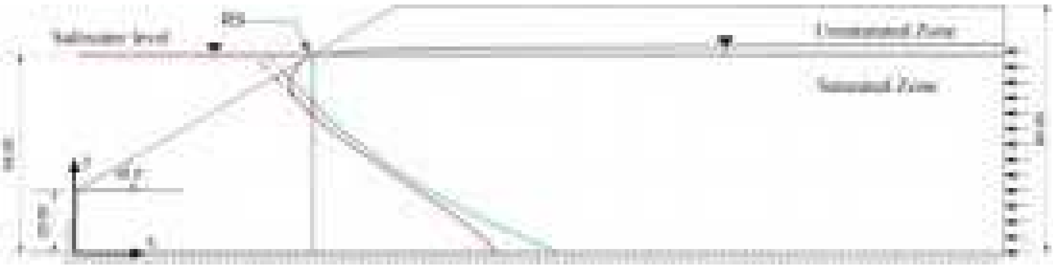

(d) $CASE - 3D/S$

Figure 3.15: Saltwater-freshwater Interface for Experiments with Single Layered Porous Media Under Static Saltwater Side Boundary Condition (Red Line: FEFLOW Simulation Results; Blue Line: Experimental Results Obtained from G-Channel Based Image Analysis)

SGD flow path was identified by using tracer injection technique. *Malachite Green* (external tracer) was injected under density neutral condition (without externally generated buoyancy) at different locations through a tube like setup within the porous media. The tracer experiments were started after attaining the quasi-steady state condition and continued till the tracer reached the intersection point of saltwater level and sloping beach face. Time varying images of the tracer experiments are shown in Figure 3.16. It is evident that SGD particles move along the SWI zone and rise in upward direction (up to the intersection point).

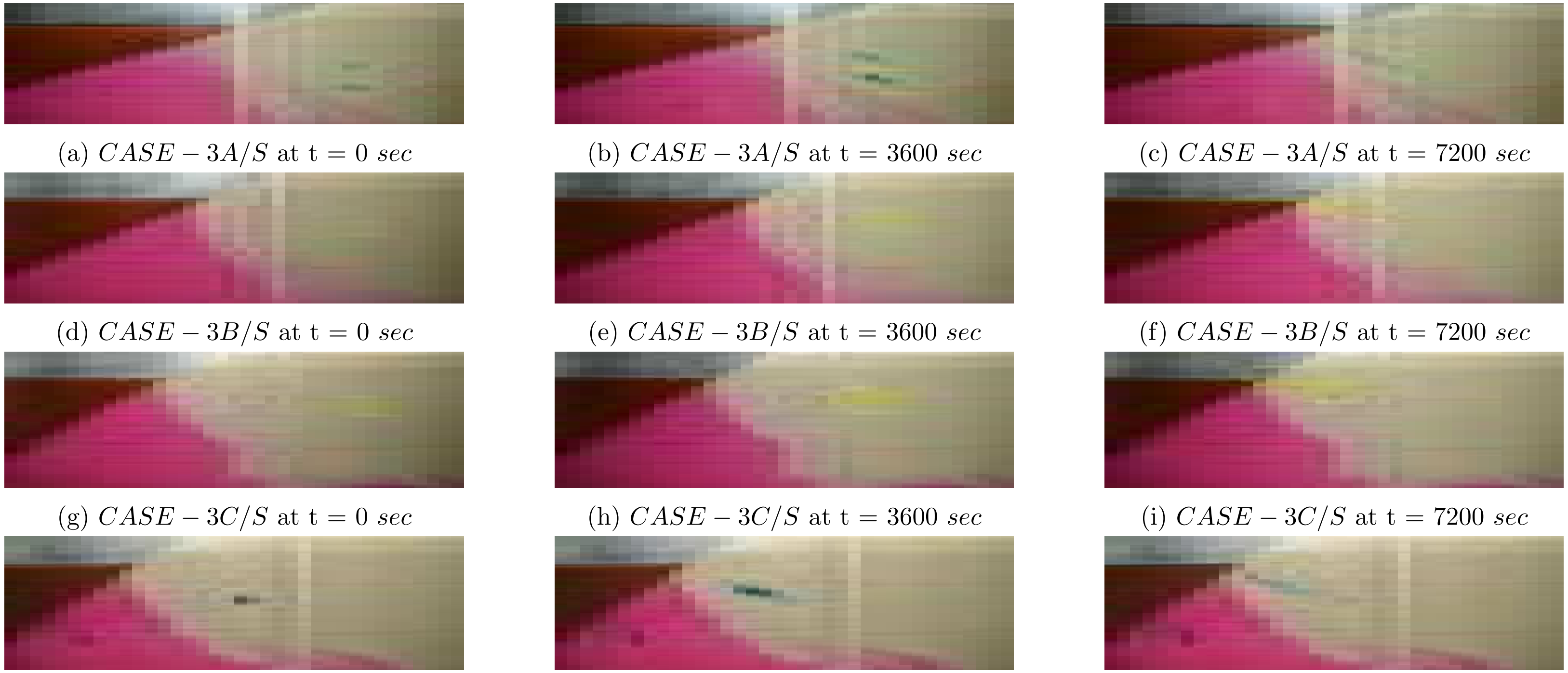

(a) $CASE - 3A/S$ at t = 0 *sec*
(b) $CASE - 3A/S$ at t = 3600 *sec*
(c) $CASE - 3A/S$ at t = 7200 *sec*
(d) $CASE - 3B/S$ at t = 0 *sec*
(e) $CASE - 3B/S$ at t = 3600 *sec*
(f) $CASE - 3B/S$ at t = 7200 *sec*
(g) $CASE - 3C/S$ at t = 0 *sec*
(h) $CASE - 3C/S$ at t = 3600 *sec*
(i) $CASE - 3C/S$ at t = 7200 *sec*
(j) $CASE - 3D/S$ at t = 0 *sec*
(k) $CASE - 3D/S$ at t = 3600 *sec*
(l) $CASE - 3D/S$ at t = 7200 *sec*

Figure 3.16: SGD Flow Pathways for Experiments with Single Layered Porous Media Under Static Saltwater Side Boundary Condition

3.2 Influence of Beach Slope on Saltwater Movement in Single Layer Under Tidal Condition

Tides are important oceanic force acting on coastal aquifers. Static saltwater level represents the average of tidal oscillations. Water varies between High Saltwater Level (HSL) and Low Saltwater Level (LSL) during rising and falling tide, respectively. In a tidal cycle saltwater level drops below the freshwater level during falling tide. This leads to a phase-averaged saltwater circulation within the saltwater wedge. Upper saline plume (USP) emerges as a result of circulation process. Moreover, freshwater discharge (Li et al., 1999; Moore et al., 2008; Robinson et al., 2007a, 2018; Yu et al., 2019b) occurs as submarine groundwater discharge (SGD) through the region between USP and the saltwater wedge. SGD depends on freshwater flux coming from inland side (Watson et al., 2010). Walther et al. (2017) performed numerical experiments with sloping beach face. However, no study is available on quantification of beach slope effect on coastal aquifers. The current study focused on quantification of beach slope effect in single layer unconfined aquifer under tidal condition through laboratory and numerical experiments. The laboratory experiments were carried out with Grade I (1-2 mm) Indian Standard Sand (IS: 650-1991) with varying beach slope to understand the saltwater dynamics in single (homogeneous) layered porous media under tidal saltwater boundary conditions. Laboratory experiments were conducted in *Sand Box Model* under controlled initial and boundary conditions. The experimental configurations are presented in Table 3.4. The flow circulation study in freshwater zone was also performed.

3.2.1 Experimental Method

The schematic diagram of the experimental setup is shown in Figure 3.17. It included three components i) Two Dimensional *Sand Box Model* (3.1 m length $\times$ 1.0 m high $\times$ 0.020 m wide), ii) Tidal Mechanism, iii) Pressure Transducers ($PS1$ to $PS6$) with Data Acquisition System. The both freshwater and saltwater reservoirs were available at both ends. The right side freshwater reservoir was utilized to supply freshwater flux from inland boundary. The left side saltwater reservoir was connected to the *Tidal Mechanism* with Oscillating saltwater column (Figure 3.17b). Water level in saltwater reservoir was maintained through overflow outlet located in left boundary of the *Sand Box Model*.

Four different beach slopes, 15°, 20°, 25°, and 30° were considered for cases $CASE-3A/T$, $CASE-3B/T$, $CASE-3C/T$ and $CASE-3D/T$, respectively.

Table 3.4: Configurations for Experiments with Single Layered Porous Media Under Tidal Saltwater Side Boundary Condition

Cases	Beach Slope	Sand	Stratification	Tidal/ Static	Remarks
$CASE-3A/T$	15^0	Grade I IS sand $d_{50} = 1.12\ mm$	No	Tidal	-
$CASE-3B/T$	20^0	Grade I IS Sand $d_{50} = 1.12\ mm$	No	Tidal	-
$CASE-3C/T$	25^0	Grade I IS Sand $d_{50} = 1.12\ mm$	No	Tidal	-
$CASE-3D/T$	30^0	Grade I IS Sand $d_{50} = 1.12\ mm$	No	Tidal	-

Saturated freshwater flow was allowed (for 2-3 days) through the intermediate zone ($Zone-B$) to get a stabilized aquifer equivalent formation. All of the following steps were performed before starting the experiments:

1. Preparation of the saltwater solution with *Rhodamine B*.
2. Valve connecting the *Tidal Mechanism* was opened.
3. Bottom outlet were closed.
4. The aquifer was saturated up to a height of 0.65 m with freshwater.
5. Continuous supply of freshwater in $ZoneC$ was ensured with peristaltic pump (120 rpm, equivalent to 6.00 m/d).
6. The outlet valve of $ZoneA$ placed at a 0.65 m was opened to maintain the water level.
7. Pressure transducers were connected and calibrated.
8. Camera was started in self capturing mode (2 s interval) along with the lighting arrangements.

A *Tidal Mechanism* was designed to impose a periodic oscillation boundary conditions at left side of the *Sand Box Model* (Figure 3.17b). It produces suction pressure in both the directions between saltwater reservoir (forward) to oscillating saltwater column (backward). The *Controller System* operates Rotodyne DC motor in forward and backward directions for a fixed time period to create a tidal wave.

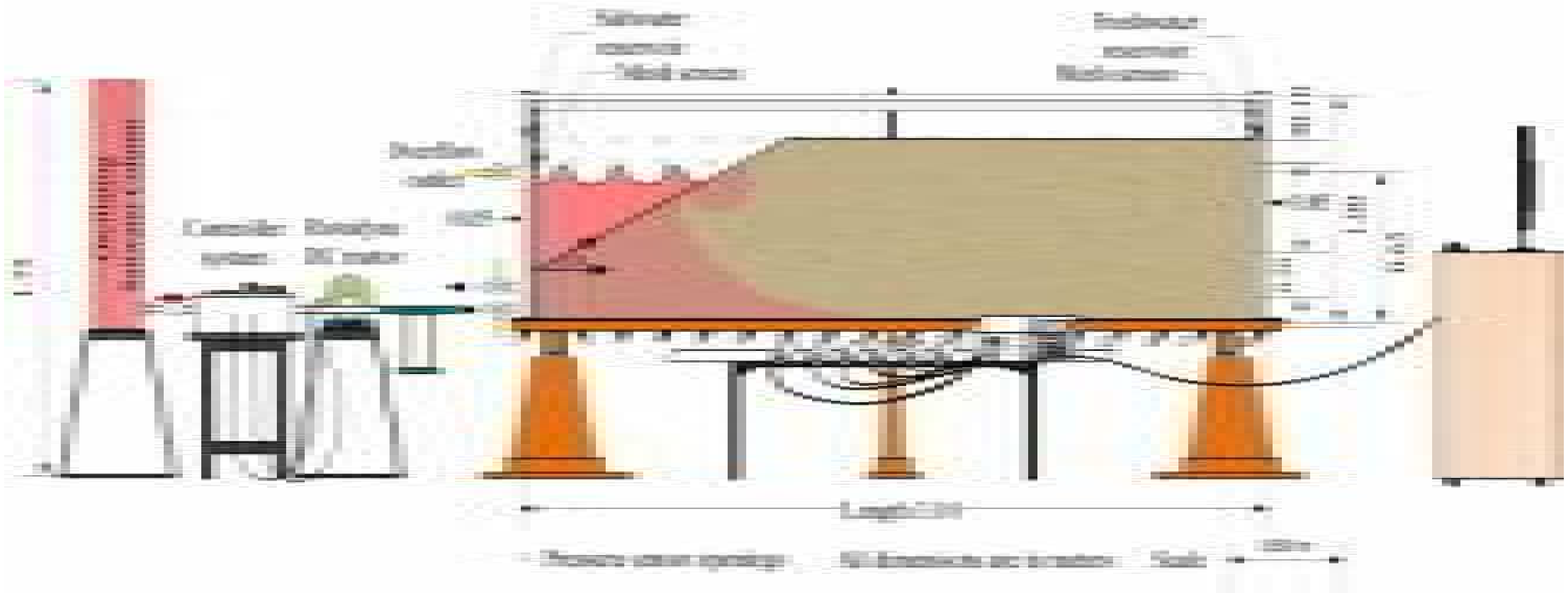

(a) Two Dimensional *Sand Box Model* with Tidal Mechanism

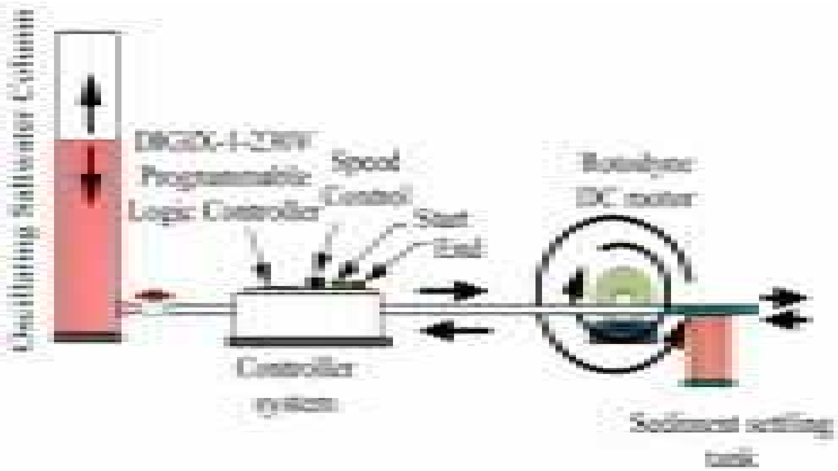

(b) Tidal Mechanism

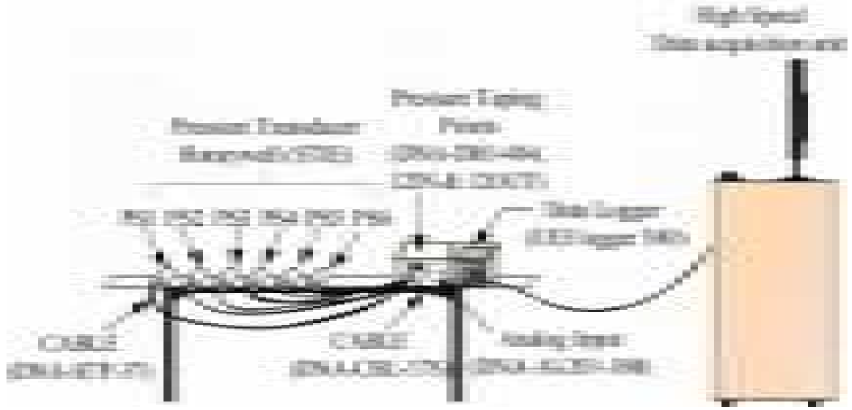

(c) Pressure Transducers with Data Acquisition System

Figure 3.17: Schematic Representation Experimental Setup with Single Layered Porous Media Under Tidal Saltwater Side Boundary Condition

Six pressure transducers ($PS1$ to $PS6$) were connected to the back side glass wall of the *Sand Box Model*. The pressure values were recorded (sampling frequency: 20 Hz) through the data acquisition system (Figure 3.17c). The salinity of the saltwater solution was monitored using the CTD Diver. Approximately 35000 mg/l saltwater concentration was maintained in $ZoneA$ after initial period (Figures 3.18a, 3.18b, 3.18c, and 3.18d). The pressure measurements for density dependent experiments were recorded only after stabilisation of the salinity measurements. Figure 3.18 shows the starting point for different experimental cases. The experiments ($CASE-3A/T$, $CASE-3B/T$, $CASE-3C/T$, $CASE-3D/T$) were continued until 18 h to 20 h (time required to achieve a quasi-steady condition).

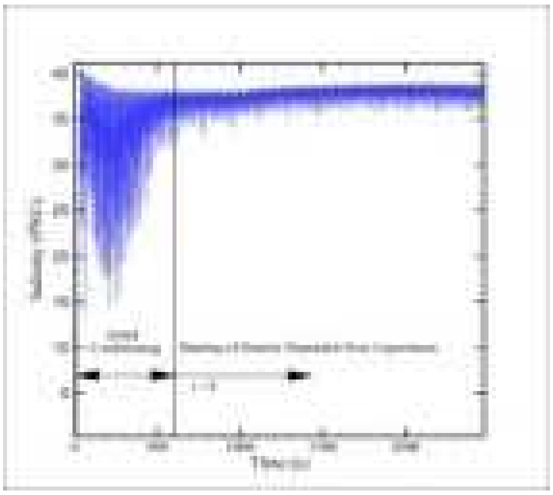

(a) $CASE-3A/T$

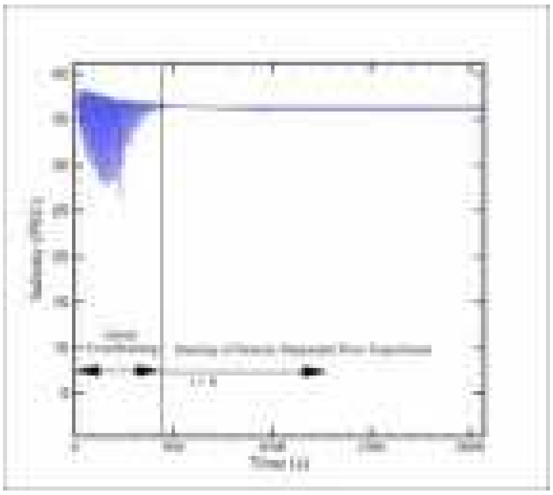

(b) $CASE-3B/T$

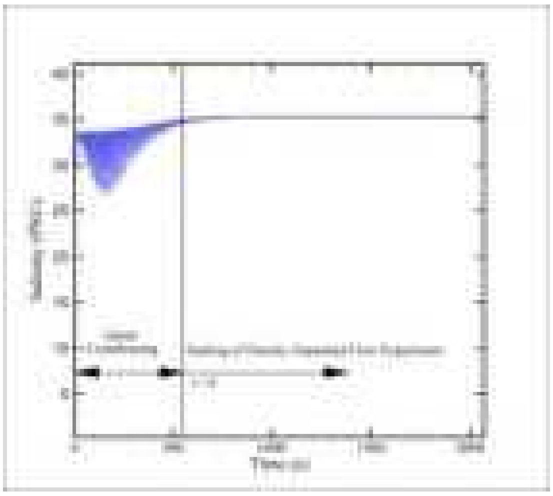

(c) $CASE-3C/T$

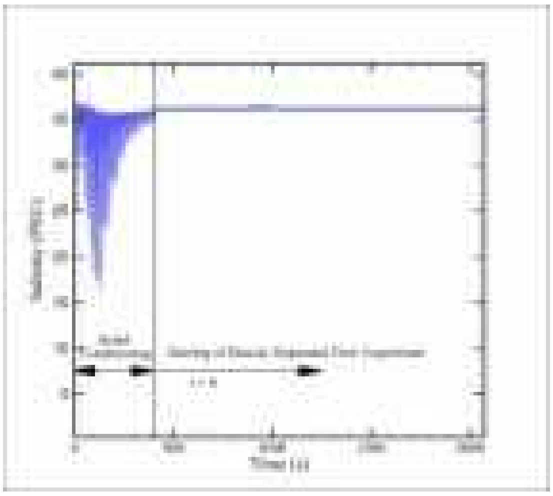

(d) $CASE-3D/T$

Figure 3.18: Observed Time Varying Salinity Profiles at Saltwater Reservoir ($Zone-A$)

3.2.2 Numerical Simulation Model

Numerical simulation model FEFLOW (Diersch, 2013) was utilized to get pressure head and concentration information for two-dimensional vertical cross-section at different time levels. Mesh convergence study was performed to determine optimal unstructured finite element mesh of different sizes (case dependent) for the *Sand Box Model*. The optimal element size varied from 0.001 m to 0.004 m. Peclet number criterion ($\mathrm{Pe_m} = \Delta \mathrm{L}/\alpha_\mathrm{L} < 4$) for numerical stability was followed while discretizing the case specific model domains with triangular mesh (Diersch, 2013). Details of boundary conditions are shown in Figure 3.19.

3.2.2.1 Initial and Boundary Conditions

The laboratory based physical model equivalent numerical domain ($CASE - 3A/T$, $CASE - 3B/T$, $CASE - 3C/T$, $CASE - 3D/T$), and relevant boundary conditions are shown in Figure 3.19. Initial conditions for all cases were specified in terms of head and concentration values. At the beginning, the domain was saturated with freshwater at constant flux from the right side (freshwater concentration). Initial conditions were specified in accordance with the boundary conditions by running the simulation model under quasi steady state condition (without saltwater). Along the saltwater-side boundary ($B_1 - C_1$) time varying equivalent freshwater head condition was applied. Concentration boundary conditions were assigned from the starting point (after stabilization of conductivity values as shown in Figure 3.18) of the experiments. Initial free surface in porous media or water table ($B_1 - F_1$) was identified from the quasi-steady state run. Two types of boundary conditions were assigned i) Dirichlet Boundary and ii) Neumann Boundary.

Dirichlet Boundary Condition
Time varying saltwater head equivalent boundary condition was specified along sloping boundary ($B_1 - C_1$). Actual tidal water levels were specified as Dirichlet Condition.

Individual nodes along the boundary were identified for specification of flow and concentration Dirichlet boundary conditions. A seepage face boundary was adopted up to the point where the saltwater level meets the sloping beach face. A constant mass concentration was applied for the boundary nodes below the saltwater surface. Above the saltwater surface two cases were considered (Shoushtari et al., 2015): i) atmospheric pressure was specified for the saturated nodes corresponding to previous time step, and ii) no-flow condition was specified for the

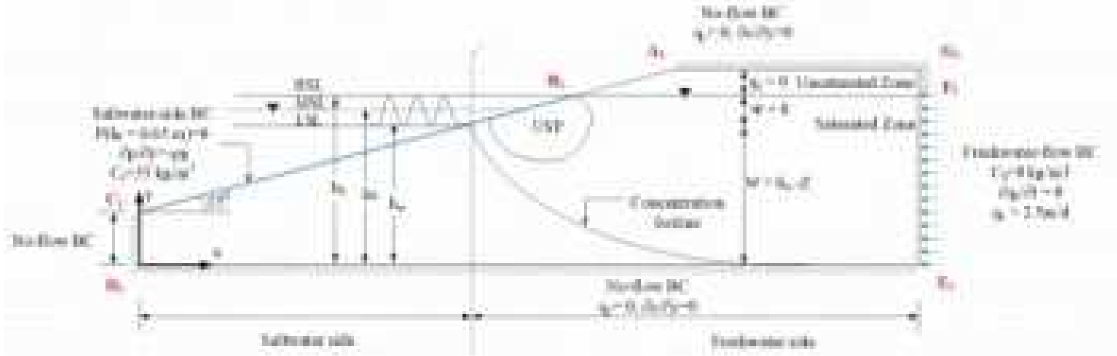

(a) $CASE-3A/T$

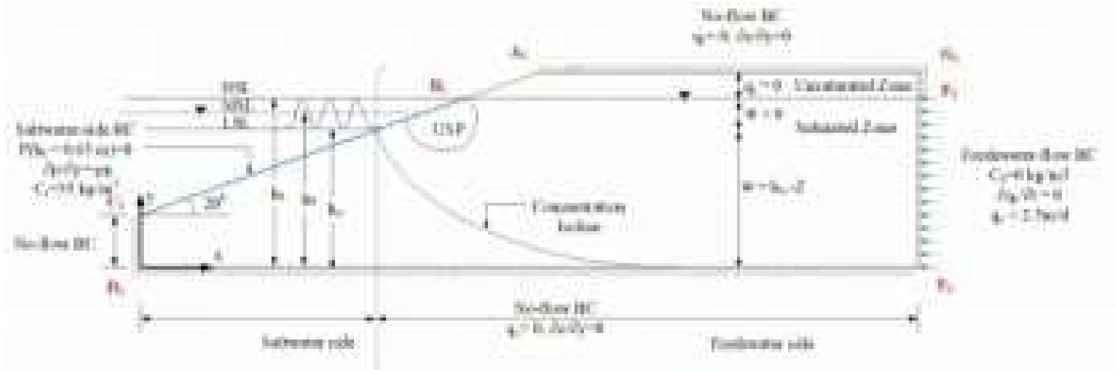

(b) $CASE-3B/T$

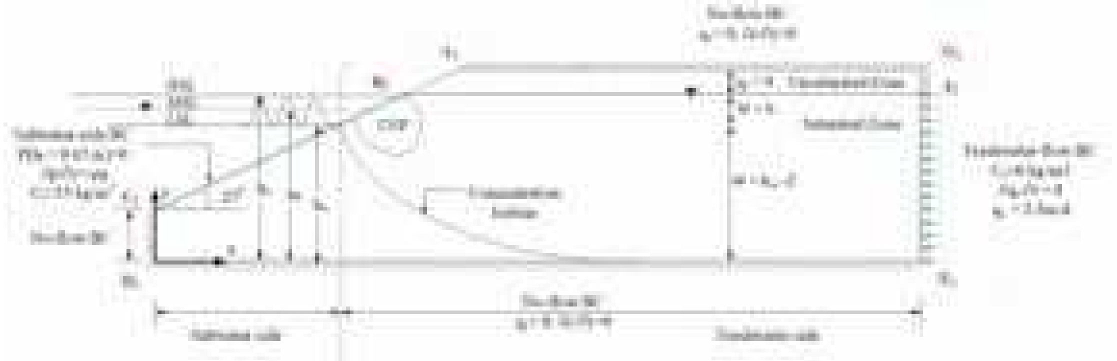

(c) $CASE-3C/T$

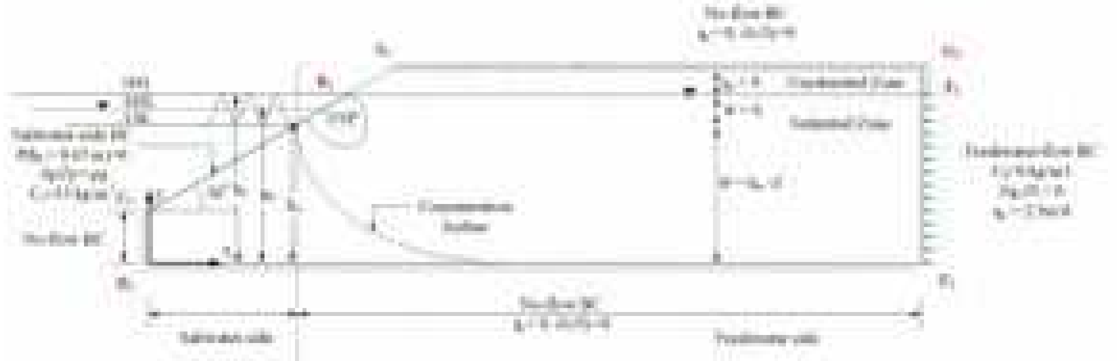

(d) $CASE-3D/T$

Figure 3.19: Boundary Conditions Used in Numerical Simulation for Experiments with Single Layered Porous Media Under Tidal Saltwater Side Condition.

unsaturated nodes. Specified constant concentration (saltwater, 35000 mg/l) condition was applied along the sloping boundary for all saturated nodes. Zero concentration level was specified for all unsaturated nodes.

Neumann Boundary Condition
Freshwater flow from right side ($E_1 - F_1$) was specified as Neumann flux type boundary condition. The peristaltic pump was used for creating the freshwater flux boundary condition. Top boundary ($G_1 - A_1$), bottom boundary ($D_1 - E_1$), vertical face in saltwater side boundary ($C_1 - D_1$), and top vertical face in right side boundary ($F_1 - G_1$) were specified with zero Neumann condition for flow and mass transport (concentration). The model was then calibrated against the experimental results using the physical parameters as shown in Table 3.5.

Table 3.5: Numerical Parameters Used for Experiments with Single Layered Porous Media Under Tidal Saltwater Side Boundary Condition

Parameters	**Symbols**	**Value**	**Unit**
Horizontal Length	L	3.1	m
Domain thickness	H	1.0	m
Porosity	ϵ	0.385	-
Saltwater level	h_f	0.66	m
Freshwater density	ρ_0	1000	kg/m^3
Saltwater density	ρ_s	1025	kg/m^3
Saltwater concentration	C_s	35	kg/m^3
Longitudinal dispersivity	β_L	0.004	m
Transverse dispersivity	β_T	0.0004	m
Molecular diffusion coefficient	D	10^{-9}	m^2/s
Density Ratio	χ	0.025	-
Hydraulic conductivity	K	600	m/d

3.2.3 G-Channel Based Image Analysis

Experimental images were analysed as per the *G-Channel Based Image Analysis* framework presented in Algorithm 1 (*Subsection* 3.1.3).

3.2.4 Results and Discussion

Saltwater-freshwater interface dynamics in single layer was studied for four different beach slopes ($\alpha =$, 15°, 20°, 25°, 30°) under tidal saltwater water level condition. Tidal experiments, viz, $CASE-3A/T$, $CASE-3B/T$, $CASE-3C/T$,

$CASE-3D/T$ were considered for quantification of influence of beach slope. Moreover, numerical simulations were also performed. Prominent fingering effect was not visible for any case under tidal condition. Due tidal water level variation two separate saltwater zones were visible for all cases. First saltwater zone was similar to the saltwater wedge visible under static saltwater boundary condition. The second zone, also known as *Upper Saline Plume*, extended between High Saltwater Level (HSL) and Low Saltwater Level (LSL). Submarine groundwater discharge (SGD) occurred through the intermediate zone between the saltwater wedge and USP. The zones are clearly visible in Figures 3.20, 3.21, 3.22, 3.23 for Saltwater-freshwater interfaces are clearly visible for $CASE-3A/T$, $CASE-3B/T$, $CASE-3C/T$, $CASE-3D/T$, respectively. The tidal oscillations changed the hydraulic gradient across the sloping beach face. This hydraulic gradient change generated circulating saltwater flow (in clockwise direction) within porous media in inter-tidal zone. This circulating flow resulted in the formation of the USP. The USP expended with time and moved in downward direction. Finally a deformed elliptic shaped USP was observed under quasi-steady state condition.

Saltwater-freshwater interface and concentration distribution were analyzed corresponding to $t = 600\ s$, $t = 2100\ s$, $t = 7320\ s$, $t = 25800\ s$. Reasonable match of experiment, image analysis and numerical simulation results were obtained for all the cases. As observed in static cases ($CASE-3A/S$, $CASE-3B/S$, $CASE-3C/S$, $CASE-3D/S$) saltwater intrusion occurs rapidly for flatter slopes ($CASE-3A/T$). Size of saltwater wedge was minimum in $CASE-3D/T$. Comparative analysis showed that saltwater intrusion length (Toe length) decreases with increasing beach slope. Further, saltwater intrusion length decreases under tidal condition ($CASE-3A/T$, $CASE-3B/T$, $CASE-3C/T$, $CASE-3D/T$) compared to static condition ($CASE-3A/S$, $CASE-3B/S$, $CASE-3C/S$, $CASE-3D/S$). Both experimental and numerical solutions showed similar trends. Overall time required to reach a quasi-steady condition was more in $CASE-3A/T$ compared to $CASE-3A/S$. Similar trend was also observed for other slopes (20°, 25°, 30°). However, $CASE-3D/T$ was continued for maximum time among all the tidal cases to achieve a quasi-steady state condition. Overall influence of slope is evident from these analysis.

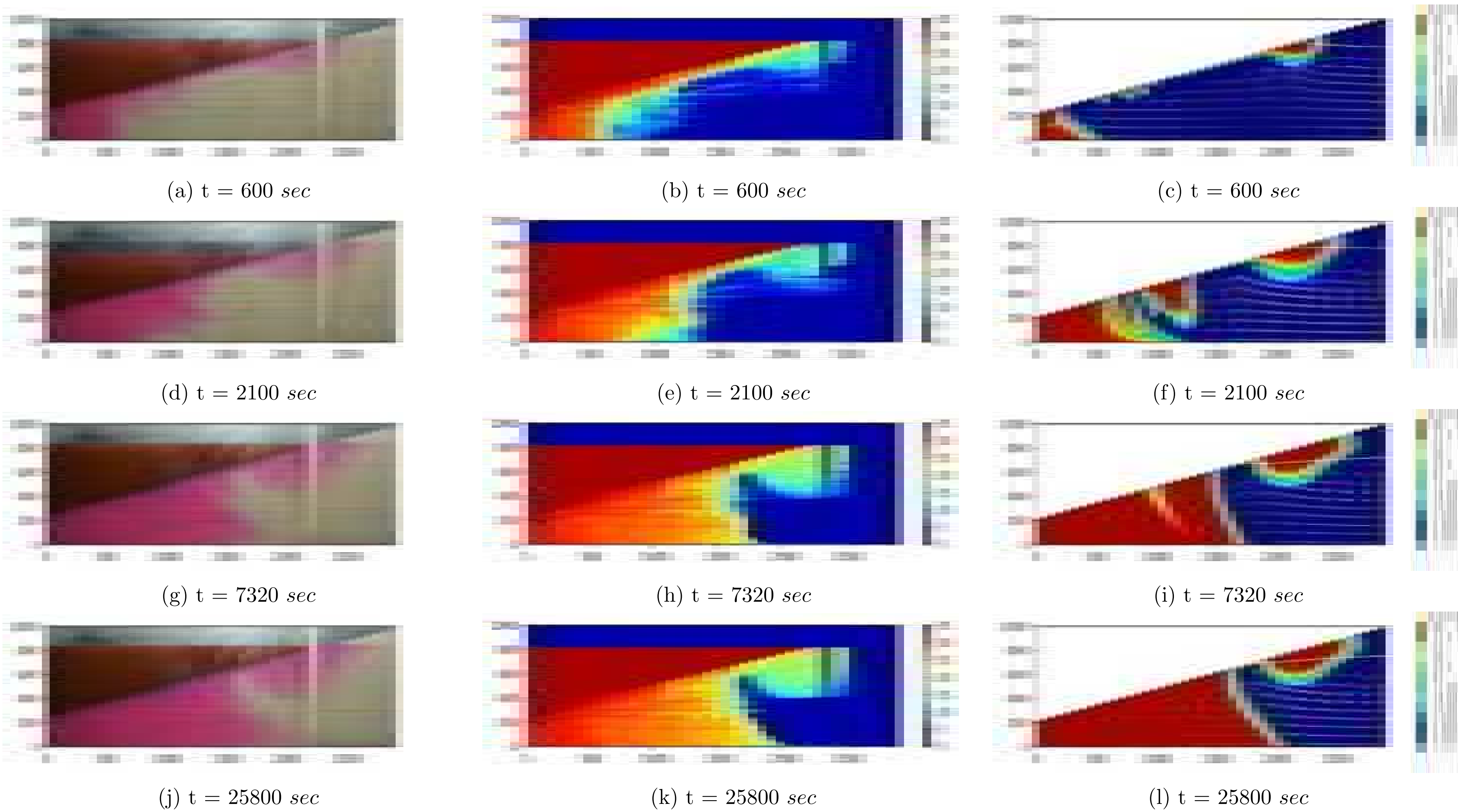

(a) t = 600 sec (b) t = 600 sec (c) t = 600 sec

(d) t = 2100 sec (e) t = 2100 sec (f) t = 2100 sec

(g) t = 7320 sec (h) t = 7320 sec (i) t = 7320 sec

(j) t = 25800 sec (k) t = 25800 sec (l) t = 25800 sec

Figure 3.20: Development of Saltwater Wedge with Time in $CASE - 3A/T$ [First Column: Experimental Images; Second Column: Output of G-Channel Based Image Analysis; Third Column: Numerical Simulation, The Color Maps Indicate Concentration]. All dimensions are in mm.

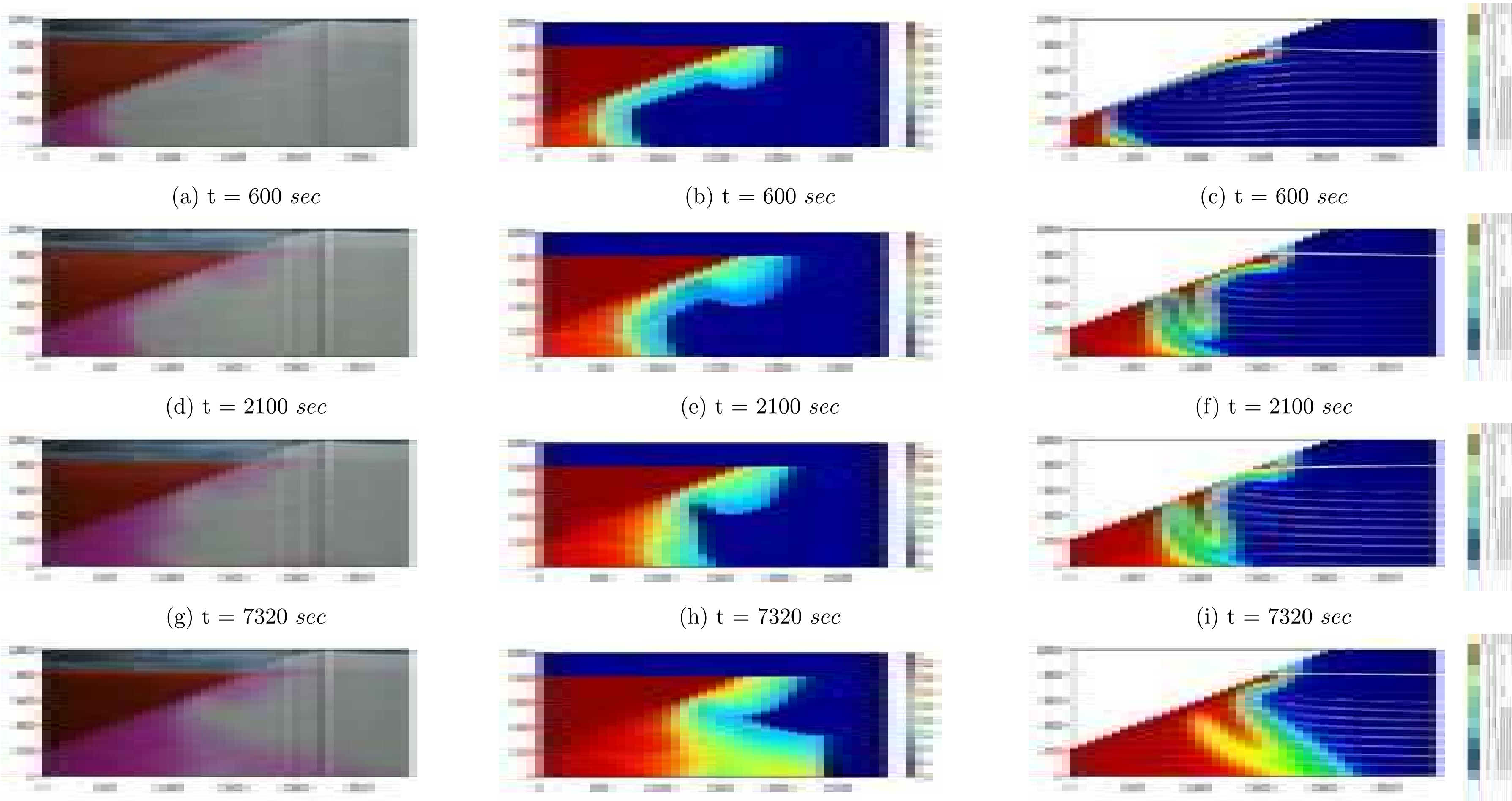

(a) t = 600 sec (b) t = 600 sec (c) t = 600 sec

(d) t = 2100 sec (e) t = 2100 sec (f) t = 2100 sec

(g) t = 7320 sec (h) t = 7320 sec (i) t = 7320 sec

(j) t = 25800 sec (k) t = 25800 sec (l) t = 25800 sec

Figure 3.21: Development of Saltwater Wedge with Time in $CASE - 3B/T$ [First Column: Experimental Images; Second Column: Output of G-Channel Based Image Analysis; Third Column: Numerical Simulation, The Color Maps Indicate Concentration]. All dimensions are in mm.

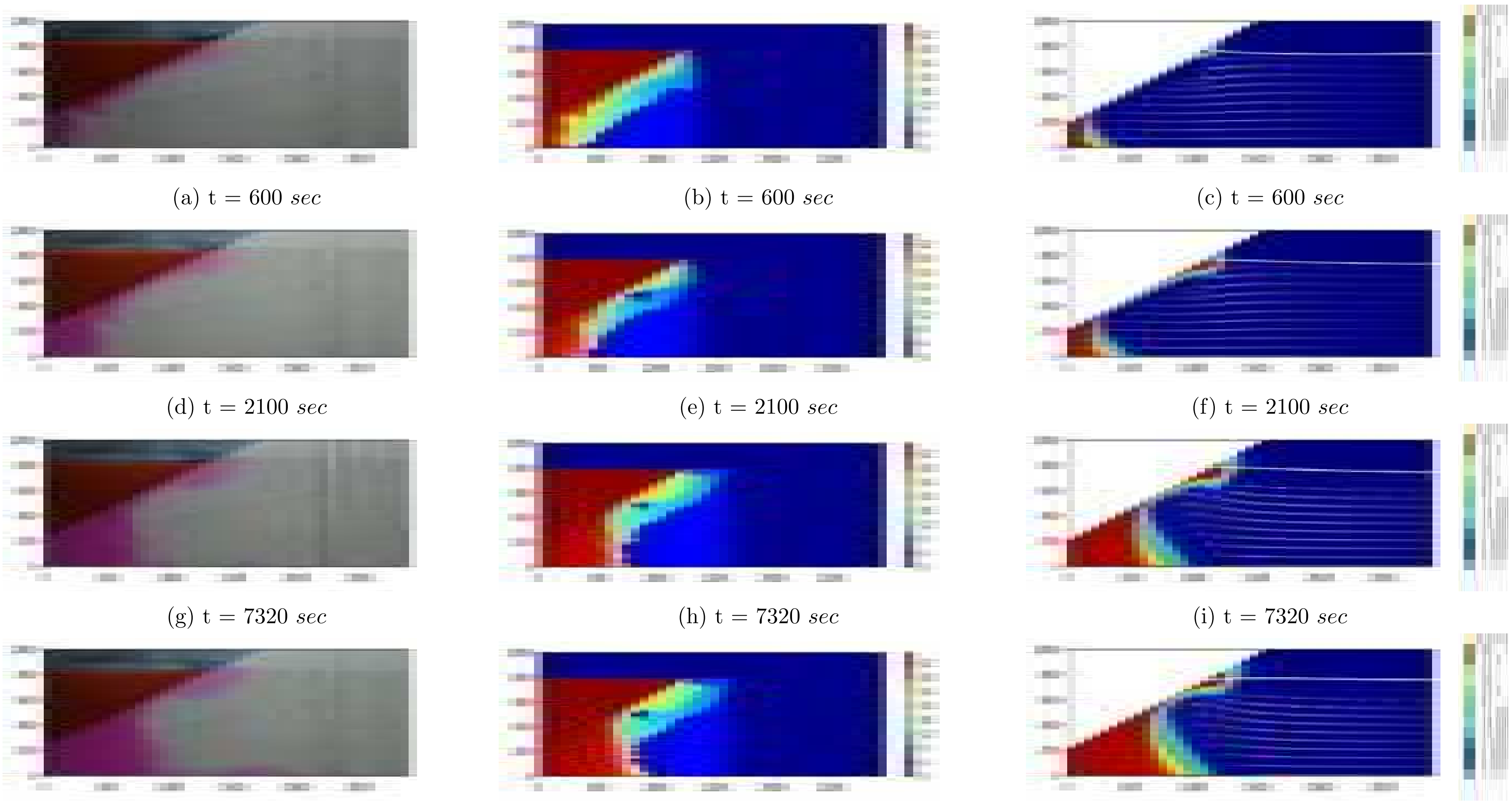

(a) t = 600 sec (b) t = 600 sec (c) t = 600 sec

(d) t = 2100 sec (e) t = 2100 sec (f) t = 2100 sec

(g) t = 7320 sec (h) t = 7320 sec (i) t = 7320 sec

(j) t = 25800 sec (k) t = 25800 sec (l) t = 25800 sec

Figure 3.22: Development of Saltwater Wedge with Time in $CASE - 3C/T$ [First Column: Experimental Images; Second Column: Output of G-Channel Based Image Analysis; Third Column: Numerical Simulation, The Color Maps Indicate Concentration]. All dimensions are in mm.

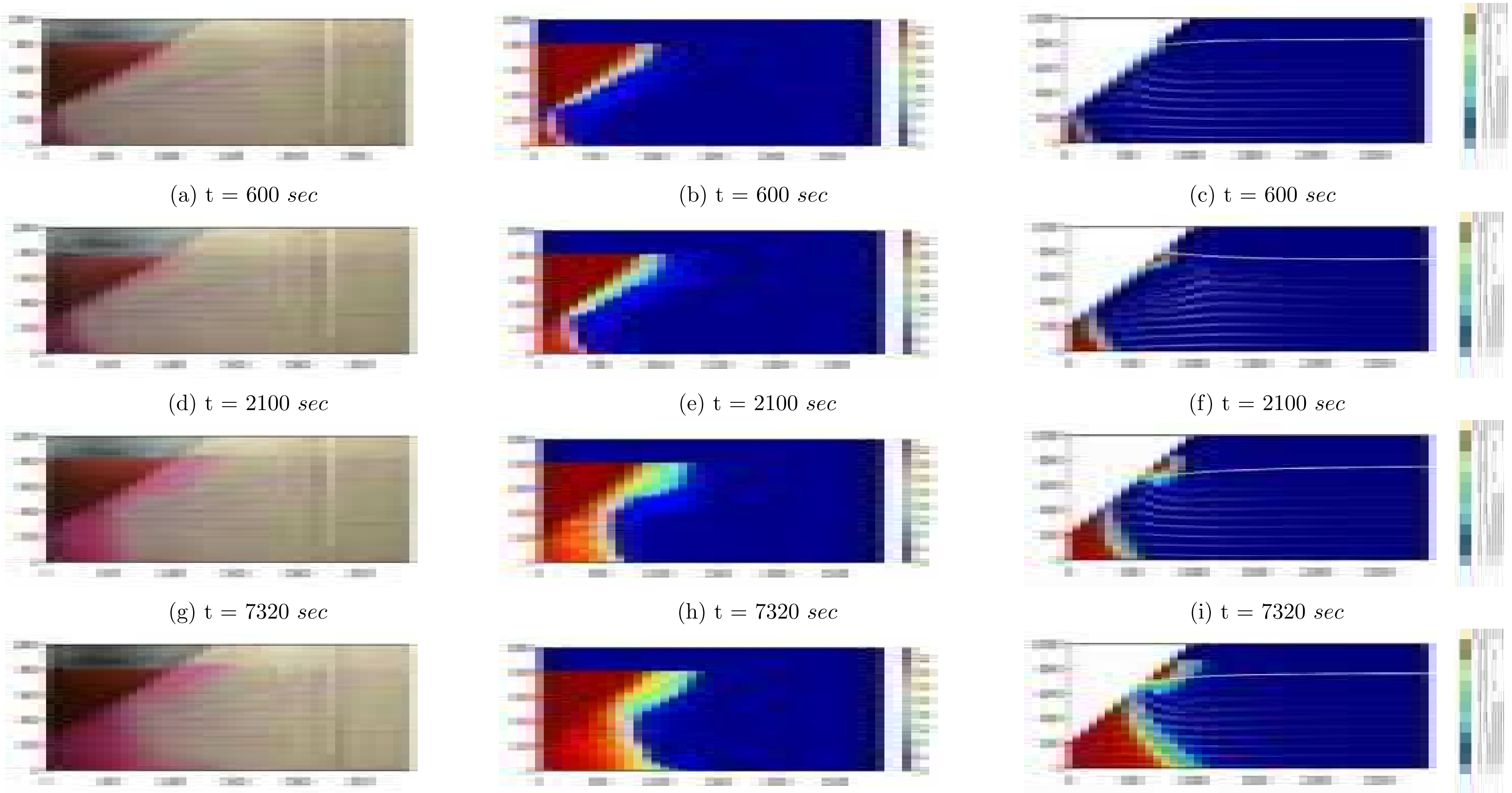

(a) t = 600 *sec* (b) t = 600 *sec* (c) t = 600 *sec*

(d) t = 2100 *sec* (e) t = 2100 *sec* (f) t = 2100 *sec*

(g) t = 7320 *sec* (h) t = 7320 *sec* (i) t = 7320 *sec*

(j) t = 25800 *sec* (k) t = 25800 *sec* (l) t = 25800 *sec*

Figure 3.23: Development of Saltwater Wedge with Time in $CASE-3D/T$ [First Column: Experimental Images; Second Column: Output of G-Channel Based Image Analysis; Third Column: Numerical Simulation, The Color Maps Indicate Concentration]. All dimensions are in mm.

Numerically simulated and experimental (Pore Water Pressure Measurement) hydraulic head values were plotted in Figure 3.24 with 1 cm band on both sides. Unlike static water level condition, the outlier clusters are corresponding to different time periods for different slopes. No outliers are visible for $CASE-3A/T$. However, outlier cluster are corresponding to time level 1800 s, 3600 s, 44760 s for $CASE-3B/T$, $CASE-3C/T$, $CASE-3D/T$, respectively. Time varying head values for $CASE-3A/T$, $CASE-3B/T$, $CASE-3C/T$, $CASE-3D/T$ are shown in Figure 3.25.

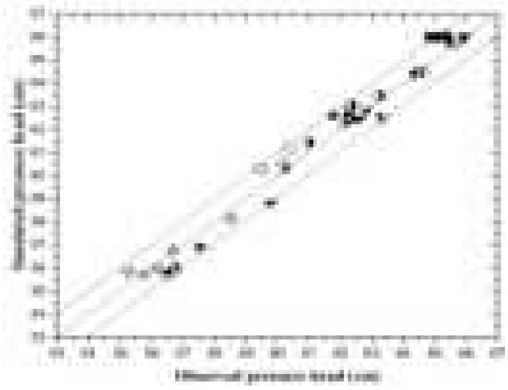

(a) $CASE-3A/T$

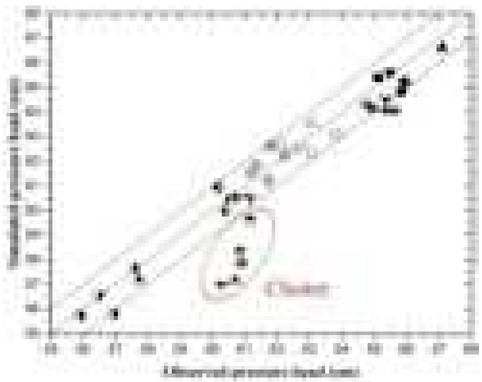

(b) $CASE-3B/T$

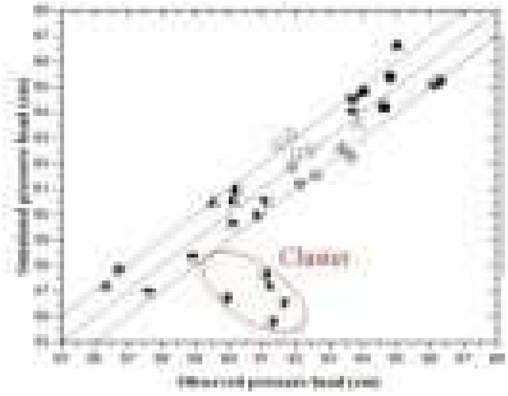

(c) $CASE-3C/T$

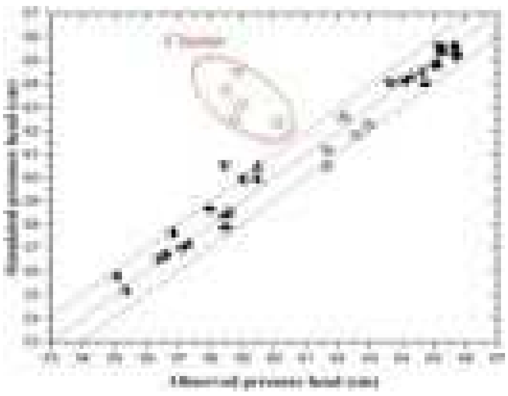

(d) $CASE-3D/T$

Figure 3.24: Comparison Between Time Varying Observed and Numerically Simulated Pressure Head Data

Processed experimental images (G-Channel Based Image Analysis) and numerically simulated saltwater-freshwater interface (50%-salinity line) were compared. The analytical (Van der Veer, 1977) values of l_T and ζ_0 are 863 mm and 564 mm,

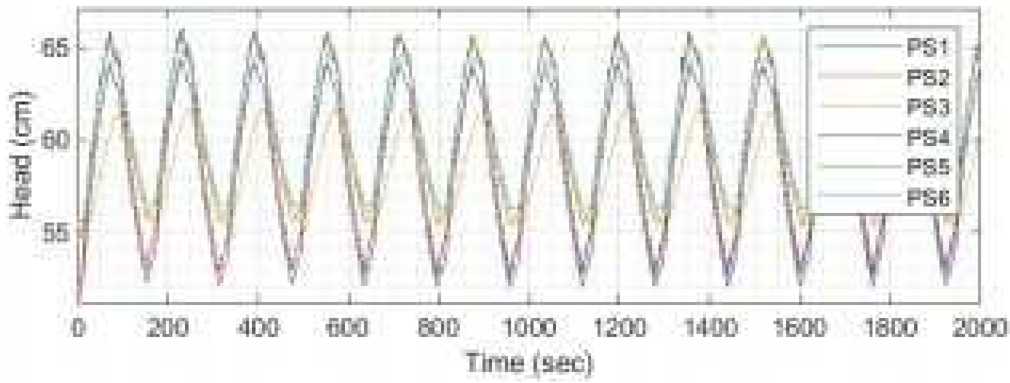

(a) $CASE-3A/T$

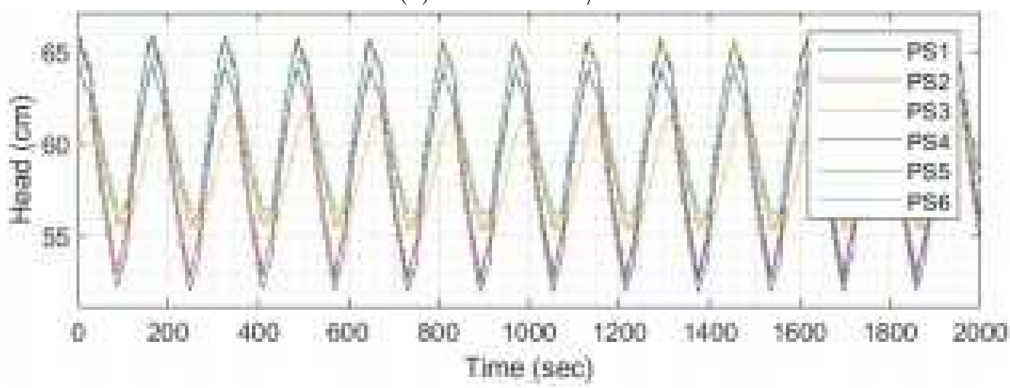

(b) $CASE-3B/T$

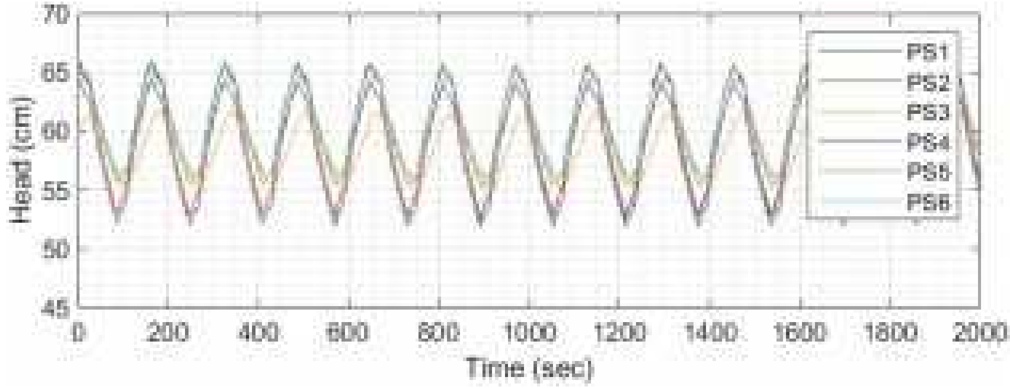

(c) $CASE-3C/T$

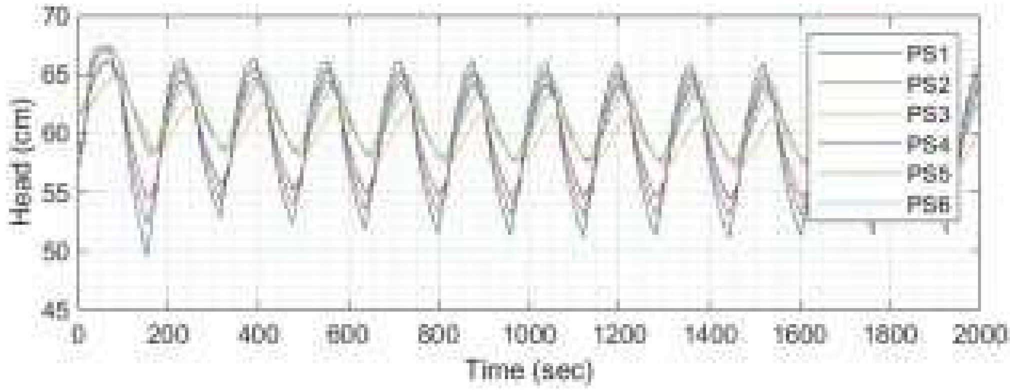

(d) $CASE-3D/T$

Figure 3.25: Observed Time Varying Pore-Water Pressure Head

respectively. The FEFLOW simulations underpredict the ζ_0 compared to the experimental value (Tables 3.6) for all the cases. Overall decreasing pattern was observed for SGD gap (ζ_0) with increase in beach slope. However, increase in ζ_0 value was observed in tidal case (e.g., $CASE - 3A/T$) when compared to static one (e.g., $CASE - 3A/S$) with same beach slope. Figure 3.26 shows saltwater-freshwater interface variations with beach slope.

Rhodamine B was utilized as the saltwater tracer. In tracer injection technique *Methyl Orange* was used as a neutral density tracer. The tracer without salt was injected in freshwater zone to identify the SGD flow path under quasi-steady state condition. Starting from the initial injection the tracer movement was captured till it reached the top of the saltwater surface. Figure 3.26 shows the SGD flow paths (tracer flow paths) for $CASE-3A/T$, $CASE-3B/T$, $CASE-3C/T$, and $CASE-3D/T$. It is evident that fresh water particles move along the saltwater-freshwater interface. Particles get discharged to the saltwater region through the intermediate zone of saltwater wedge and USP.

Table 3.6: Submarine Groundwater Discharge (SGD) Gap and Saltwater-Freshwater Interface Toe Length for Experiments with Single Layered Porous Media Under Tidal Saltwater Side Boundary Condition

Case	Slope	Sand	$\zeta_o(mm)$ Expt	$\ell_T(mm)$ Expt	$\zeta_o(mm)$ FEFLOW	$\ell_T(mm)$ FEFLOW	$\zeta_{o-FEFLOW}/\zeta_{o-Expt}$
$CASE-3A/T$	15^0	IS Sand Grade I d_{50}=1.12 mm	680.80	260.67	631.69	258.82	0.690
$CASE-3B/T$	20^0	IS Sand Grade I d_{50}=1.12 mm	619.42	364.13	530.13	361.36	0.855
$CASE-3C/T$	25^0	IS Sand Grade I d_{50}=1.12 mm	543.52	430.63	494.41	459.27	0.909
$CASE-3D/T$	30^0	IS Sand Grade I d_{50}=1.12 mm	565.84	372.44	513.39	402.00	0.907
							Avg= 0.83

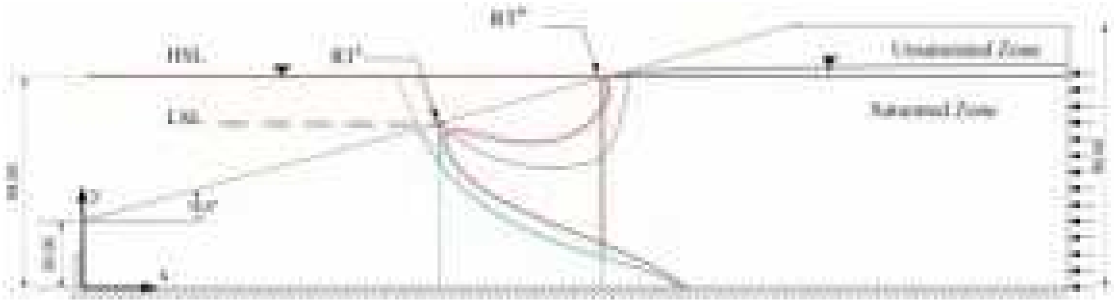

(a) $CASE - 3A/T$

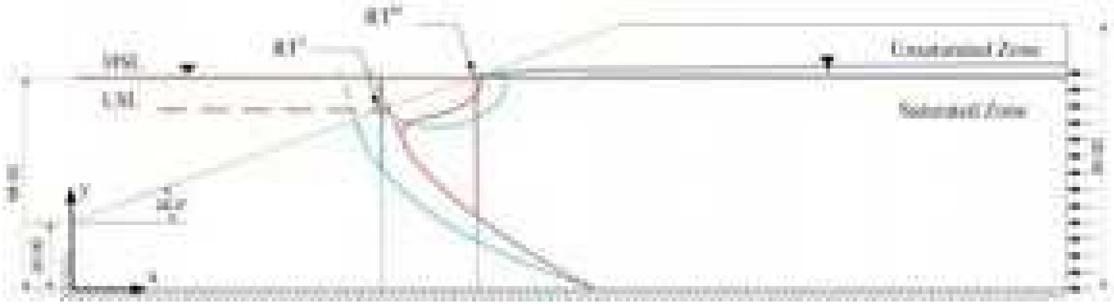

(b) $CASE - 3B/T$

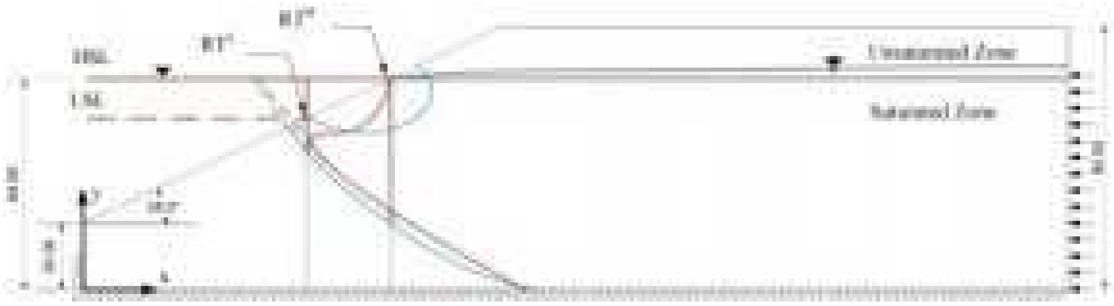

(c) $CASE - 3C/T$

(d) $CASE - 3D/T$

Figure 3.26: Saltwater-freshwater Interface for Experiments with Single Layered Porous Media Under Tidal Saltwater Side Boundary Condition (Red Line: FEFLOW Simulation Results; Blue Line: Experimental Results Obtained from G-Channel Based Image Analysis)

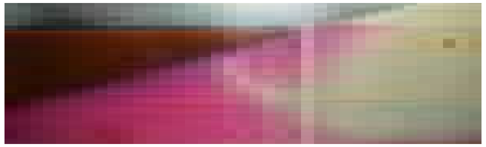

(a) $CASE - 3A/T$ at t = 0 sec

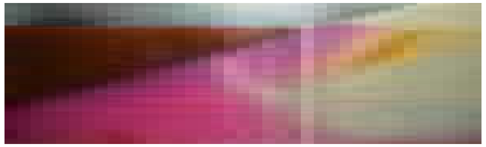

(b) $CASE - 3A/T$ at t = 3600 sec

(c) $CASE - 3A/T$ at t = 7200 sec

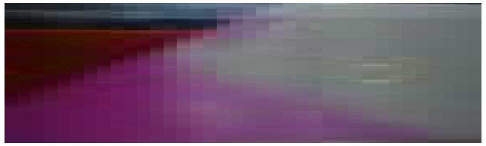

(d) $CASE - 3B/T$ at t = 0 sec

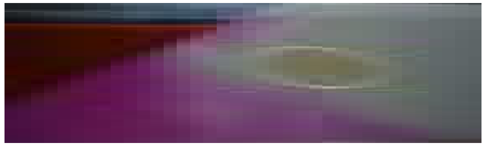

(e) $CASE - 3B/T$ at t = 3600 sec

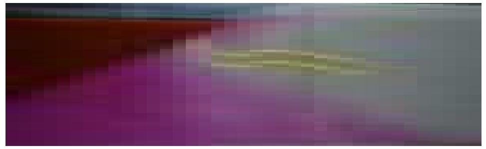

(f) $CASE - 3B/T$ at t = 7200 sec

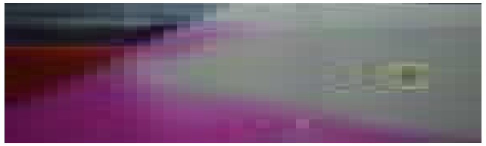

(g) $CASE - 3C/T$ at t = 0 sec

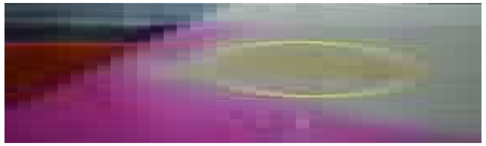

(h) $CASE - 3C/T$ at t = 3600 sec

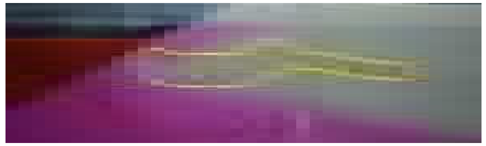

(i) $CASE - 3C/T$ at t = 7200 sec

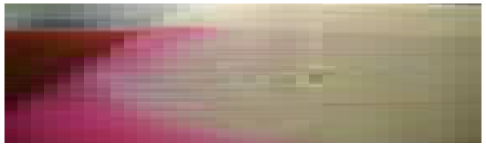

(j) $CASE - 3D/T$ at t = 0 sec

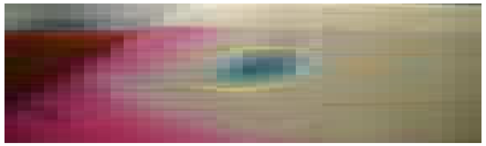

(k) $CASE - 3D/T$ at t = 3600 sec

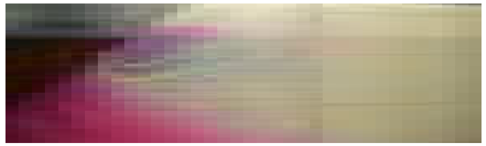

(l) $CASE - 3D/T$ at t = 7200 sec

Figure 3.27: SGD Flow Pathways for Experiments with Single Layered Porous Media Under Tidal Saltwater Side Boundary Condition

3.3 Summary

The current Chapter included the physical experiments, numerical simulations and image analysis for the single layered (Grade-I IS Sand) sloping beach under static and tidal saltwater boundary conditions. A G-Channel based image analysis technique was proposed for experimental images. A comprehensive analysis was performed to quantify the influence of sloping beach on saltwater dynamics in porous media. The next Chapter presents quantification of influence of beach slope on saltwater dynamics in stratified porous media.

Chapter 4

Influence of Beach Slope on Saltwater Movement in Multilayered Porous Media Under Static and Tidal Conditions

4.0 Overview

The previous Chapter covered the influence of beach slope on saltwater dynamics in single layered porous media under static and tidal saltwater boundary conditions. Heterogenous formation alters the flow dynamics over various length scales (Simmons et al., 2001; Houben and Post, 2017). The multilayered structures are the most commonly encountered forms of subsurface heterogeneity. Process complexity increases due to intra and inter layer mass transfer in multilayered porous media. Distinct flow patterns and saltwater-freshwater interfaces can be seen when compared to single layered porous media. A better understanding of flow dynamics in multilayered porous media is required for controlling saltwater intrusion. Previous saltwater intrusion studies (Ketabchi et al., 2014; Liu et al., 2014; Dose et al., 2014; Mehdizadeh et al., 2014, 2017; Strack and Ausk, 2015) considered stratified representation to simulate subsurface heterogeneous conditions. Numerous experimental investigations (Abdoulhalik and Ahmed, 2017b; Strack and Ausk, 2015) showed that layered heterogeneity affects the saltwater-freshwater interface toe location. The steady state saltwater-freshwater interface was mostly studied in the context of multiple permeable layers. Few studies considered the effects of low permeability layer on saltwater dynamics (Lu et al., 2013; Abdoulhalik and Ahmed, 2017b, a). Dagan and Zeitoun (1998b, a) examined the effects of heterogeneity on the shape of the saltwater-freshwater interface in horizontally layered aquifers with randomly distributed hydraulic conductivity. It was observed that uncertainty in predicting toe location increases without including the stratification information. Held et al. (2005) observed similar results. Moreover, geometry and position of toe location are directly related to the degree of heterogeneity of the aquifer. However, saltwater dynamics in sloping beach stratified porous media (with thin low permeability layer) was not studied with/without tidal conditions. The relative position and thickness of the stratified porous layers significantly affect the density dependent flow. The current study focuses on quantification of impact of beach slope variation on saltwater-freshwater interface movement in stratified porous media (both confined and unconfined configuration) under static and tidal saltwater side boundary conditions. Physical experiment, numerical analysis, image analysis and analytical solution were utilized for quantitative and qualitative analysis.

4.1 Experimental Details

The laboratory experiments were carried out to understand the influence of beach slope on saltwater dynamics in multilayered porous media (3 layered configuration including low-permeability strata) under static and tidal saltwater side boundary conditions. Grade-I Indian Standard Sand (1-2 *mm*) was used as the aquifer material for both unconfined (Top) and confined (Bottom) layers. Bentonite was used as the aquitard material for the low permeable layer (middle). Three layered porous media was placed in the *Zone B* of *Sand Box Model*. Thickness of top, middle, and bottom layers were 34 *cm*, 4 *cm*, 34 *cm*, respectively. Six pressure transducers ($PS1$ in saltwater zone; $PS2$, $PS3$, $PS4$, $PS6$ in confined zone; $PS5$ in unconfined zone) were utilized for pressure measurements. Experiments were conducted with four different beach slopes under static and tidal saltwater side boundary conditions.

4.1.1 Experiments with Static Saltwater Side Boundary Condition

The experimental setup for static saltwater side boundary condition is shown in Figure 4.1. The experimental configurations are presented in Table 4.1. The laboratory experiments were performed as per the framework presented in *Section* **??**. Saltwater salinity (35 PSU) was maintained in $ZoneA$ of the *Sand Box Model* after initial period (Figures 4.2a , 4.2b, 4.2c, and 4.2d). The static experiments were continued until 12 h to 14 h (time required to achieve a quasi-steady condition).

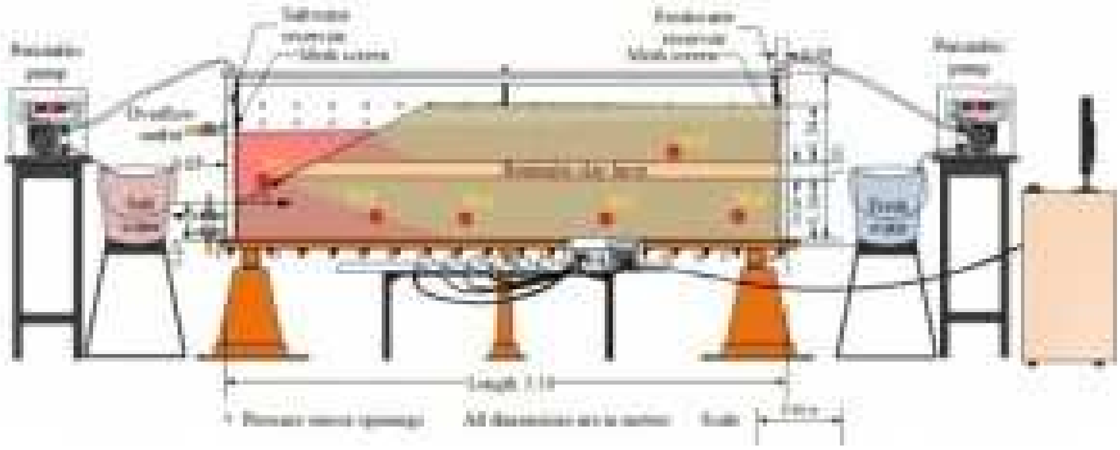

Figure 4.1: Schematic Representation Experimental Setup with Multilayered Porous Media Under Static Saltwater Side Boundary Condition

Table 4.1: Configurations for Experiments with Multilayered Porous Media Under Static Saltwater Side Boundary Condition

Cases	Beach Slope	Sand	Stratification	Tidal/ Static	Remarks
$CASE-4A/S$	15^0	Grade I IS Sand (d_{50}=1.12 mm) 40 mm clay layer	Yes	Static	-
$CASE-4B/S$	20^0	Grade I IS Sand (d_{50}=1.12 mm) 40 mm clay layer	Yes	Static	-
$CASE-4C/S$	25^0	Grade I IS Sand (d_{50}=1.12 mm) 40 mm clay layer	Yes	Static	-
$CASE-4D/S$	30^0	Grade I IS Sand (d_{50}=1.12 mm) 40 mm clay layer	Yes	Static	-

4.1.2 Experiments with Tidal Saltwater Side Boundary Condition

The experimental setup for tidal saltwater side boundary condition is shown in Figure 4.3. The experimental configurations are presented in Table 4.2. The laboratory experiments were performed as per the framework presented in *Subsection* 3.2.1. Saltwater salinity (35 PSU) was maintained in $ZoneA$ of the *Sand Box*

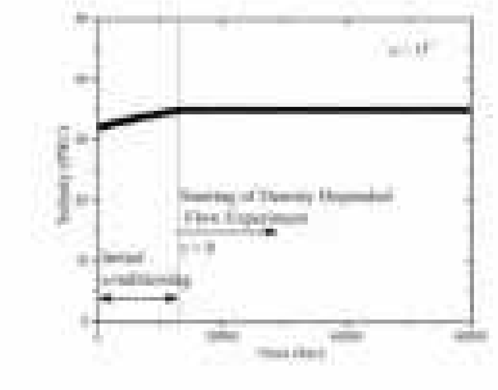

(a) $CASE-4A/S$

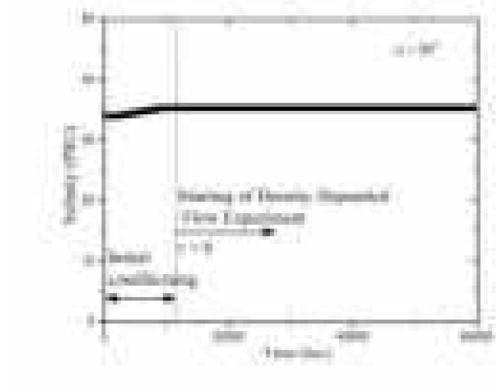

(b) $CASE-4B/S$

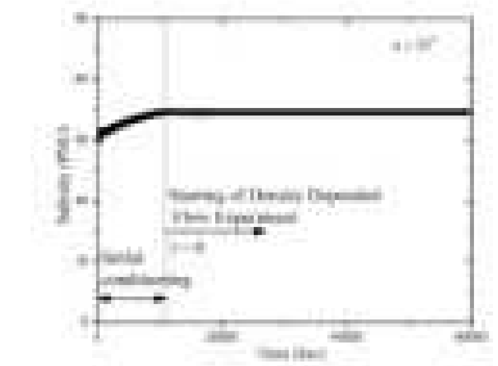

(c) $CASE-4C/S$

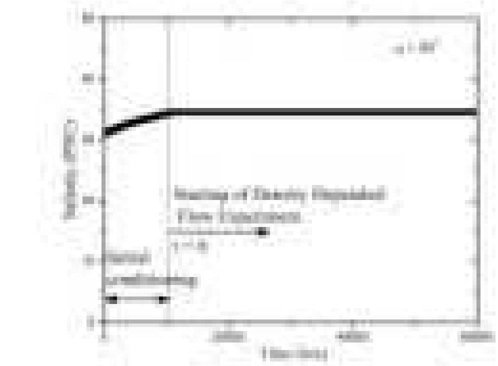

(d) $CASE-4D/S$

Figure 4.2: Observed Time Varying Salinity Profiles at Saltwater Reservoir ($Zone-A$)

Model after initial period (Figures 4.4a , 4.4b, 4.4c, and 4.4d). The tidal experiments were continued until 18 h to 20 h (time required to achieve a quasi-steady condition).

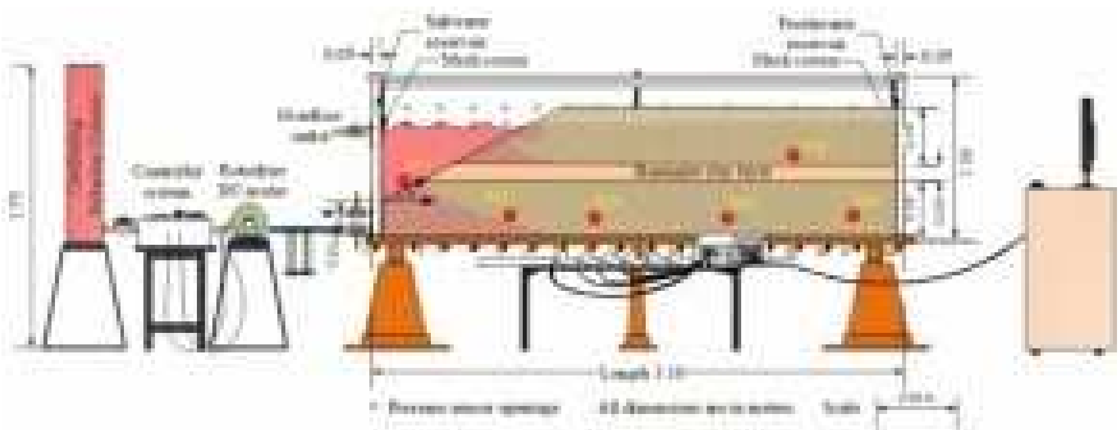

Figure 4.3: Schematic Representation Experimental Setup with Multilayered Porous Media Under Tidal Saltwater Side Boundary Condition

Table 4.2: Configurations for Experiments with Multilayered Porous Media Under Tidal Saltwater Side Boundary Condition

Cases	Beach Slope	Sand	Stratification	Tidal/ Static	Remarks
$CASE-4A/T$	15^0	Grade I IS Sand (d_{50}=1.12 mm) 40 mm clay layer	Yes	Tidal	-
$CASE-4B/T$	20^0	Grade I IS Sand (d_{50}=1.12 mm) 40 mm clay layer	Yes	Tidal	-
$CASE-4C/T$	25^0	Grade I IS Sand (d_{50}=1.12 mm) 40mm clay layer	Yes	Tidal	-
$CASE-4D/T$	30^0	Grade I IS Sand (d_{50}=1.12 mm) 40mm clay layer	Yes	Tidal	-

4.2 Numerical Modelling Method

FEFLOW (Diersch, 2013) based numerical simulation models were used to validate the experimental results (pressure head and concentration) at different time levels. Conceptualized as two-dimensional vertical cross-section was used simulations. The variably density flow and transport equations are provided in *Section* **??**. Unstructured finite element mesh (as per Peclet number criterion) of different sizes were used to discretize the *Sand Box Model*. Mesh convergence study was also performed.

4.2.1 Numerical Simulations with Static Saltwater Side Boundary Condition

The laboratory based physical model equivalent numerical domains ($CASE-4A/S$, $CASE-4B/S$, $CASE-4C/S$ and $CASE-4D/S$), and relevant boundary conditions are shown in Figure 4.5. Initial conditions were specified for head and concentration values from quasi-steady condition without saltwater intrusion. Along the saltwater-side boundary ($B_2 - F_2$) equivalent static freshwater head condition was applied. Concentration boundary conditions were assigned from the starting point (after stabilization of salinity values) of the experiments. Initial free

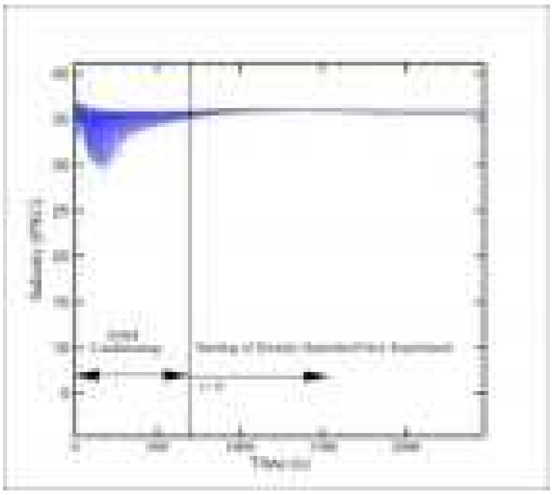

(a) $CASE-4A/T$

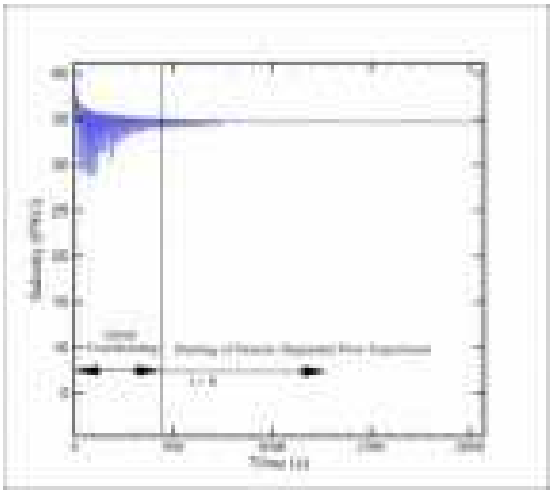

(b) $CASE-4B/T$

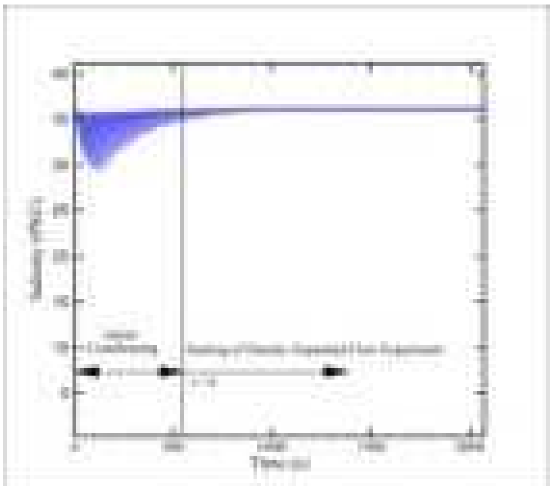

(c) $CASE-4C/T$

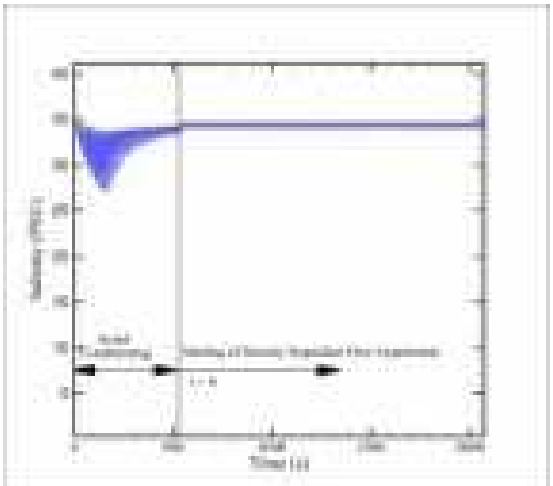

(d) $CASE-4D/T$

Figure 4.4: Observed Time Varying Salinity Profiles at Saltwater Reservoir ($Zone-A$)

surface in porous media or water table (B_2-I_2) was identified from the quasi-steady state run. Two types of boundary conditions were applied i) Dirichlet Boundary and ii) Neumann Boundary.

4.2.1.1 Dirichlet Boundary Condition

The saltwater head equivalent hydrostatic boundary condition was specified along sloping boundary (B_2-F_2). Specified constant concentration (saltwater, 35000 mg/l) condition was applied along the sloping boundary. Individual nodes along the boundary were identified for specification of flow and concentration Dirichlet boundary conditions.

4.2.1.2 Neumann Boundary Condition

Freshwater flow from right side (H_2-I_2) was specified as Neumann flux type boundary condition. The peristaltic pump was used for creating the freshwater

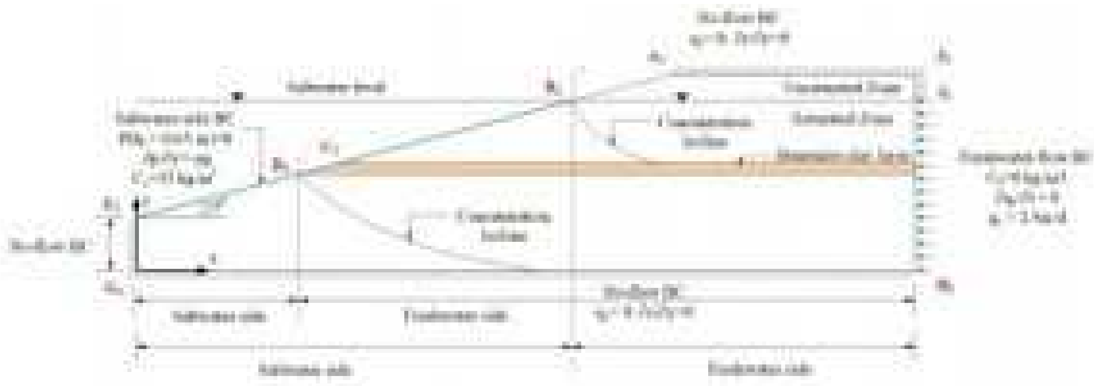

(a) $CASE-4A/S$

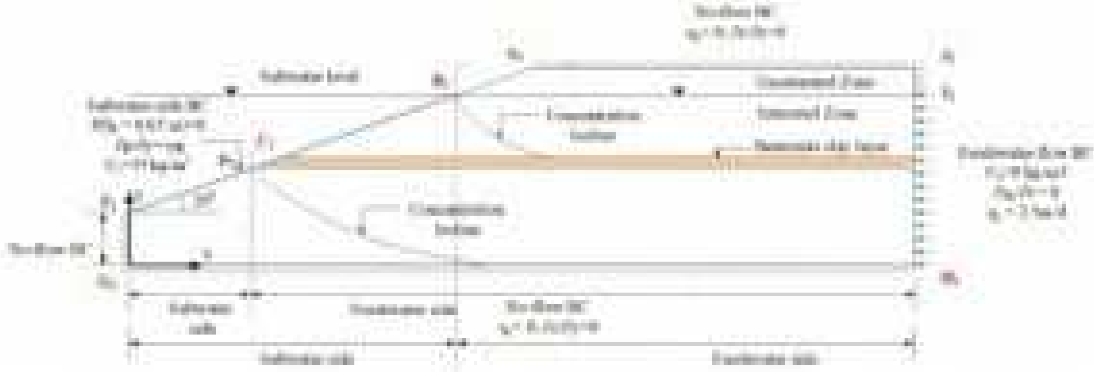

(b) $CASE-4B/S$

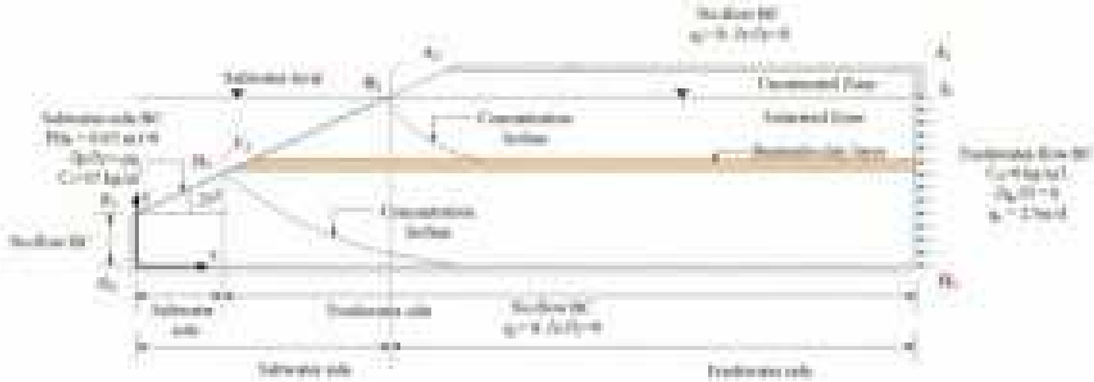

(c) $CASE-4C/S$

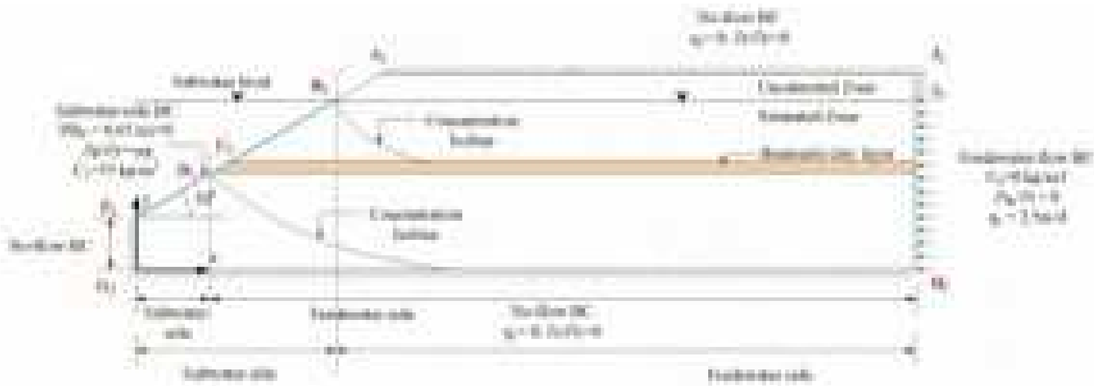

(d) $CASE-4D/S$

Figure 4.5: Boundary Conditions Used in Numerical Simulation for Experiments with Multilayered Porous Media Under Static Saltwater Side Condition

flux boundary condition. Top boundary ($J_2 - A_2$), bottom boundary ($G_2 - H_2$), vertical face in saltwater side boundary ($F_2 - G_2$), and top vertical face in right side boundary ($I_2 - J_2$) were specified with zero Neumann condition for flow and mass transport (concentration).

4.2.2 Numerical Simulations with Tidal Saltwater Side Boundary Condition

The laboratory based physical model equivalent numerical domains ($CASE - 4A/T$, $CASE - 4B/T$, $CASE - 4C/T$ and $CASE - 4D/T$), and relevant boundary conditions are shown in Figure 4.6. Initial conditions were specified same as for $CASE - 4A/S$, $CASE - 4B/S$, $CASE - 4C/S$ and $CASE - 4D/S$. Two types of boundary conditions were assigned i) Dirichlet Boundary and ii) Neumann Boundary.

4.2.2.1 Dirichlet Boundary Condition

Time varying saltwater head equivalent boundary condition was specified along sloping boundary ($B_2 - F_2$). Individual nodes along the boundary were identified for specification of flow and concentration Dirichlet boundary conditions. Boundary conditions were assigned as per *Subsubsection* 3.2.2.1 for saturated/unsaturated nodes identified during a particular tidal cycle.

4.2.2.2 Neumann Boundary Condition

The Neumann boundary conditions were specified as per *Subsubsection* 4.2.1.2.

Individual models under static and tidal saltwater boundary conditions were calibrated against the experimental results using the physical parameters as presented in Table 4.3.

4.3 G-Channel Based Image Analysis

Experimental images were analysed as per the *G-Channel Based Image Analysis* framework presented in Algorithm 1 (*Subsection* 3.1.3).

4.4 Results and Discussion

Saltwater-freshwater interface dynamics in multilayered porous media was studied experimentally and numerically for four different beach slopes (α =, 15°, 20°, 25°, 30°) under static ($CASE - 4A/S$, $CASE - 4B/S$, $CASE - 4C/S$,

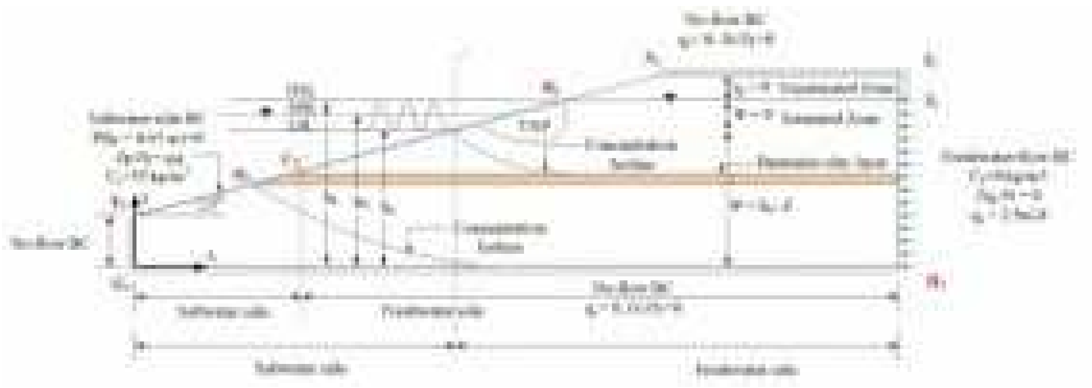

(a) $CASE-4A/T$

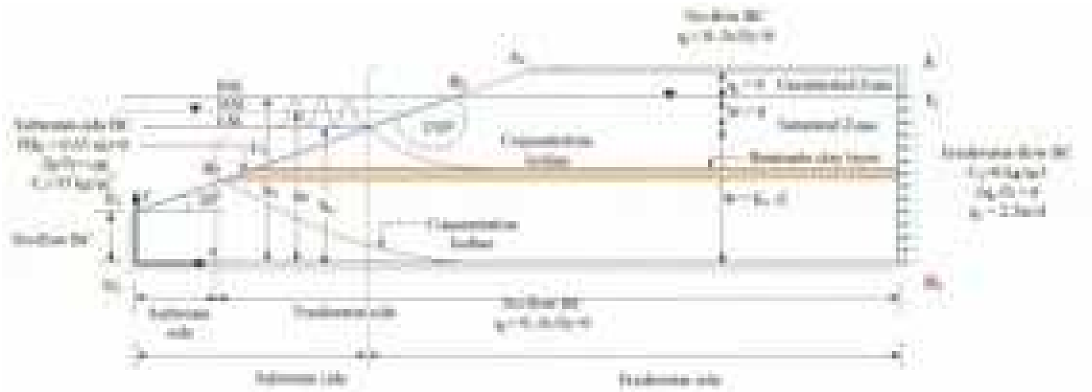

(b) $CASE-4B/T$

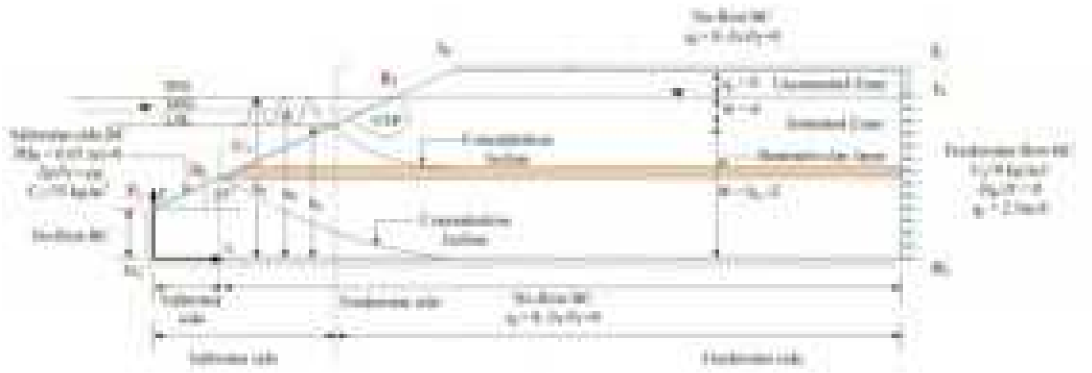

(c) $CASE-4C/T$

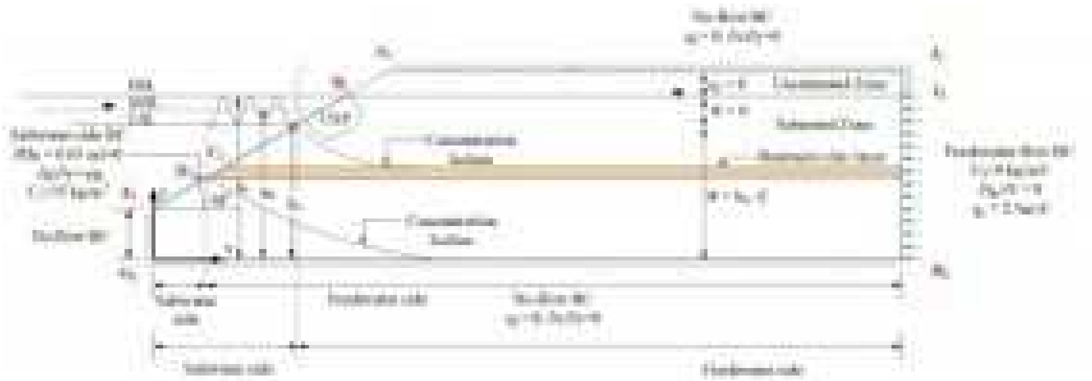

(d) $CASE-4D/T$

Figure 4.6: Boundary Conditions Used in Numerical Simulation for Experiments with Multilayered Porous Media Under Tidal Saltwater Side Condition

Table 4.3: Numerical Parameters Used for Experiments with Multilayered Porous Media Under Static and Tidal Saltwater Side Boundary Conditions

Parameters	**Symbols**	**Value**	**Unit**
Horizontal Length	L	3.1	m
Domain thickness	H	1.0	m
Porosity	ϵ	0.385	-
Saltwater level	h_f	0.66	m
Freshwater density	ρ_0	1000	kg/m^3
Saltwater density	ρ_s	1025	kg/m^3
Saltwater concentration	C_s	35	kg/m^3
Longitudinal dispersivity	β_L	0.004	m
Transverse dispersivity	β_T	0.0004	m
Molecular diffusion coefficient	D	10^{-9}	m^2/s
Density Ratio	χ	0.025	-
Hydraulic conductivity(IS Sand)	K_s	600	m/d
Hydraulic conductivity(Bentonite)	K_B	0.00004	m/d

$CASE-4D/S$) and tidal ($CASE-4A/T$, $CASE-4B/T$, $CASE-4C/T$, $CASE-4D/T$) saltwater side boundary conditions. Physical experiments, numerical simulations, experimental image analysis, and analytical solution were utilized for quantitative analysis. Time varying saltwater intrusion patterns for static experiments, G-Channel based image analysis and numerical simulations (0.5-concentration isoline) are shown in Figures 4.7, 4.8, 4.9, 4.10. Saltwater-freshwater interface and concentration distribution were analyzed corresponding to $t = 600\ s$, $t = 2100\ s$, $t = 7320\ s$, $t = 25800\ s$. Reasonable match of experiment, image analysis and numerical simulation results were obtained for all the cases. Fingering effect was prominent in unconfined layer($CASE-4A/S$) for flatter slope (15°). However, reduction in fingering effect was observed with the increase in beach slope. Minimal effect was observed in confined layer. It was also observed that scale effect dominates the fingering effect, e.g., larger effect was present in case of $CASE-3A/S$ when compared to $CASE-4A/S$. Saltwater intrudes rapidly in unconfined layer compared to confined one. No specific trend was observed with respect to the size of the saltwater wedge both in case of unconfined and confined layers. This may be due to scale effect as some specific trends were observed in case of single layered configurations. Time required to reach the quasi-steady condition was less in case of flatter slope ($CASE-4A/S$). It increases with the increase in beach slope.

Time varying saltwater intrusion patterns for tidal condition are shown in Figures 4.11, 4.12, 4.13, 4.14. Prominent fingering effect was not visible for any case under tidal condition. Under tidal action both saltwater wedge and *Upper Saline Plume* were visible for unconfined layer. Only saltwater wedge was observed in confined layer. Submarine groundwater discharge (SGD) occurred through the intermediate zone between the saltwater wedge and USP. The zones are clearly visible in Figures 4.11, 4.12, 4.13, 4.14 for $CASE-4A/T$, $CASE-4B/T$, $CASE-4C/T$, $CASE-4D/T$, respectively. As observed in static cases ($CASE-4A/S$, $CASE-4B/S$, $CASE-4C/S$, $CASE-4D/S$) saltwater intrusion occurs rapidly in unconfined layer compared to confined layers. Saltwater wedge size increases for flatter slopes ($CASE-4A/T$). Size of saltwater wedge was minimum in $CASE-4D/T$. Comparative analysis showed that saltwater intrusion length (Toe length) decreases with increasing beach slope. Further, saltwater intrusion length decreases under tidal condition ($CASE-4A/T$, $CASE-4B/T$, $CASE-4C/T$, $CASE-4D/T$) compared to static condition ($CASE-4A/S$, $CASE-4B/S$, $CASE-4C/S$, $CASE-4D/S$). Overall time required to reach a quasi-steady condition was more in $CASE-4A/T$ compared to $CASE-4A/S$. Similar trend was also observed for other slopes (20°, 25°, 30°). However, $CASE-4D/T$ was continued for maximum time among all the tidal cases to achieve a quasi-steady state condition.

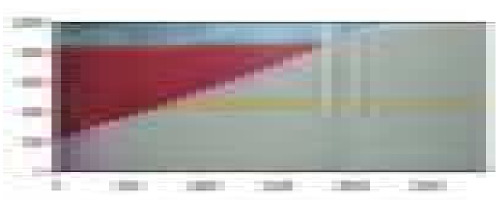

(a) t = 600 *sec*

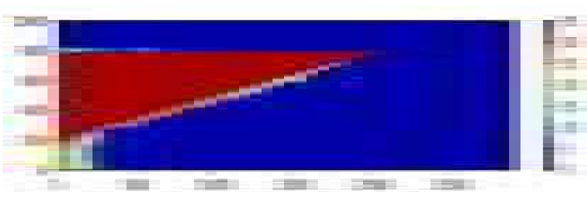

(b) t = 600 *sec*

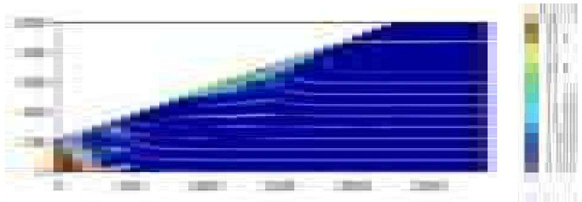

(c) t = 600 *sec*

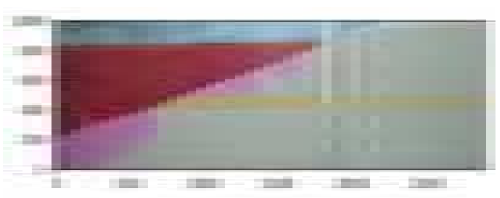

(d) t = 2100 *sec*

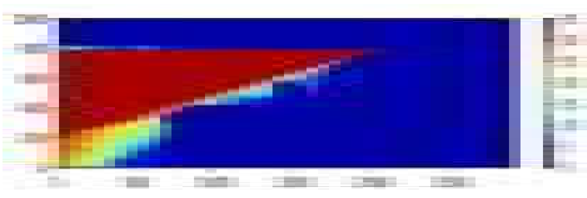

(e) t = 2100 *sec*

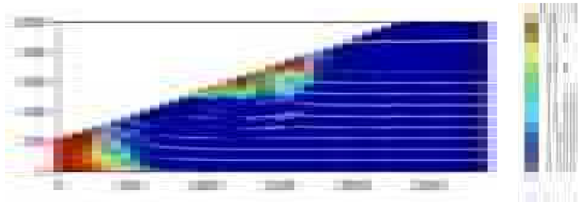

(f) t = 2100 *sec*

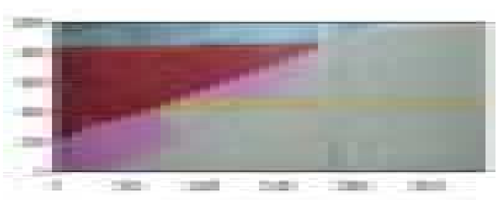

(g) t = 7320 *sec*

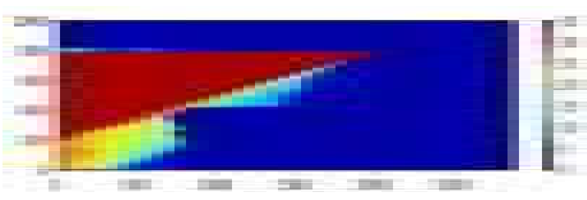

(h) t = 7320 *sec*

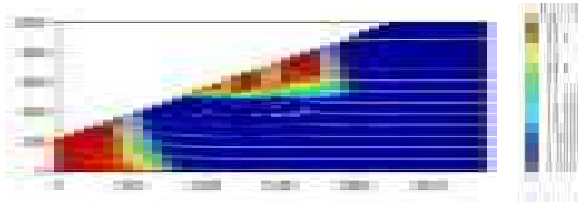

(i) t = 7320 *sec*

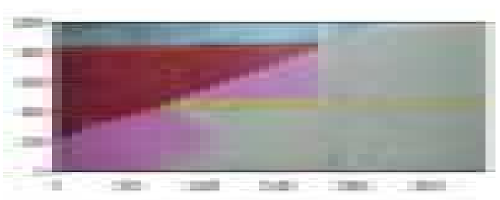

(j) t = 25800 *sec*

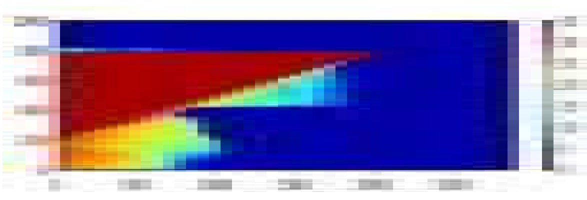

(k) t = 25800 *sec*

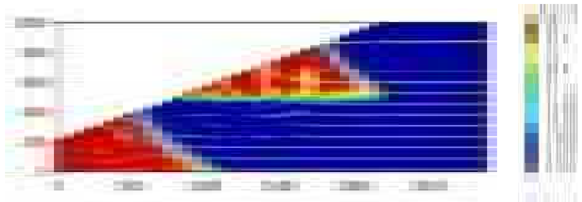

(l) t = 25800 *sec*

Figure 4.7: Development of Saltwater Wedge with Time in $CASE-4A/S$ [First Column: Experimental Images; Second Column: Output of G-Channel Based Image Analysis; Third Column: Numerical Simulation, The Color Maps Indicate Concentration]. All dimensions are in mm.

(a) t = 600 *sec*

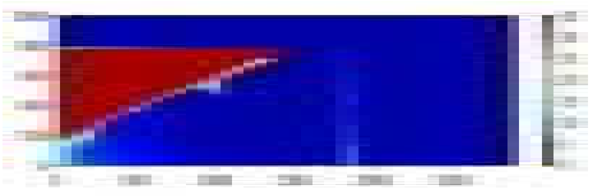

(b) t = 600 *sec*

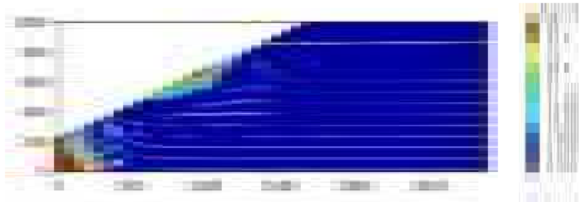

(c) t = 600 *sec*

(d) t = 2100 *sec*

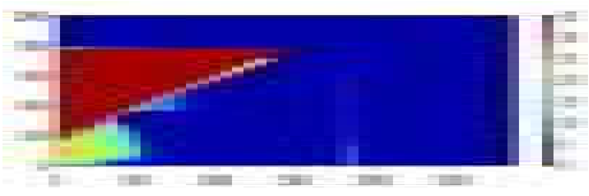

(e) t = 2100 *sec*

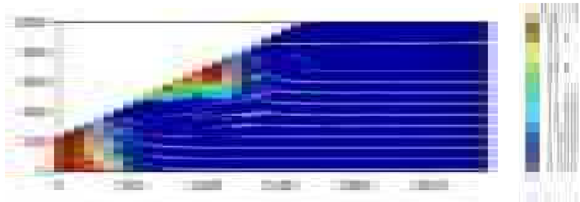

(f) t = 2100 *sec*

(g) t = 7320 *sec*

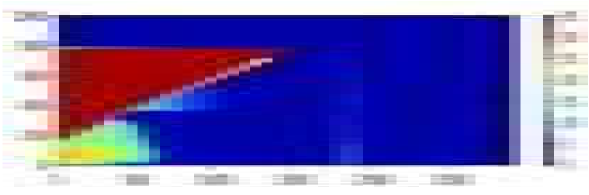

(h) t = 7320 *sec*

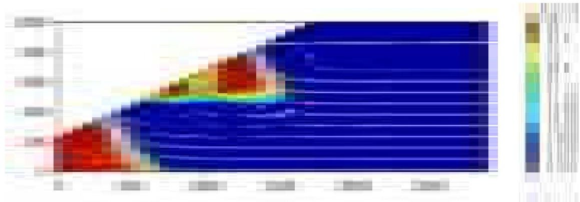

(i) t = 7320 *sec*

(j) t = 25800 *sec*

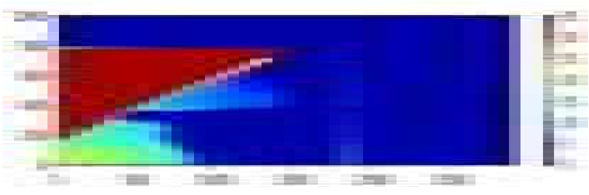

(k) t = 25800 *sec*

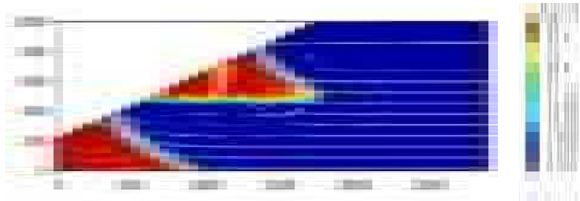

(l) t = 25800 *sec*

Figure 4.8: Development of Saltwater Wedge with Time in $CASE-4B/S$ [First Column: Experimental Images; Second Column: Output of G-Channel Based Image Analysis; Third Column: Numerical Simulation, The Color Maps Indicate Concentration]. All dimensions are in mm.

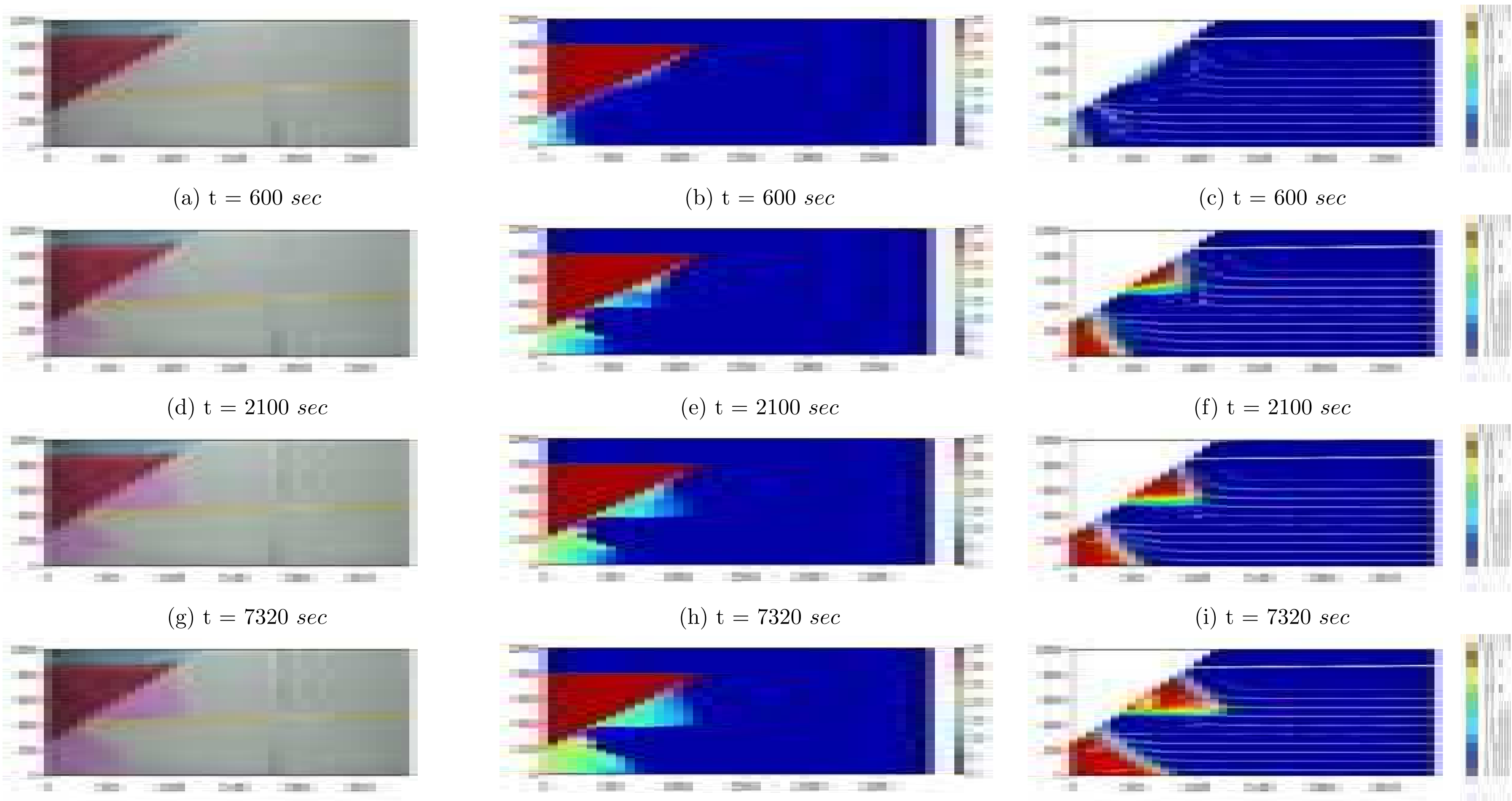

(a) t = 600 *sec* (b) t = 600 *sec* (c) t = 600 *sec*

(d) t = 2100 *sec* (e) t = 2100 *sec* (f) t = 2100 *sec*

(g) t = 7320 *sec* (h) t = 7320 *sec* (i) t = 7320 *sec*

(j) t = 25800 *sec* (k) t = 25800 *sec* (l) t = 25800 *sec*

Figure 4.9: Development of Saltwater Wedge with Time in $CASE - 4C/S$ [First Column: Experimental Images; Second Column: Output of G-Channel Based Image Analysis; Third Column: Numerical Simulation, The Color Maps Indicate Concentration]. All dimensions are in mm.

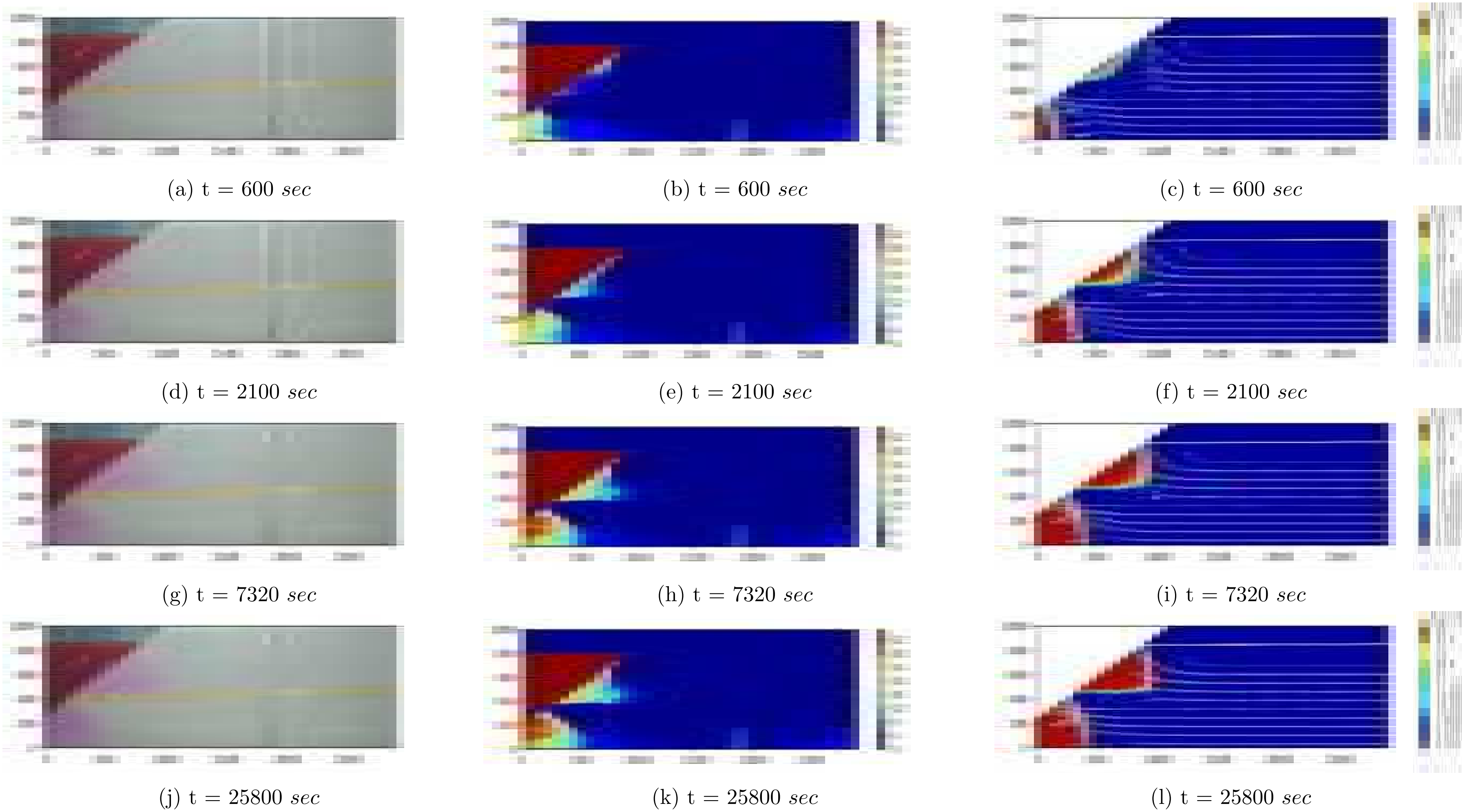

(a) t = 600 sec (b) t = 600 sec (c) t = 600 sec

(d) t = 2100 sec (e) t = 2100 sec (f) t = 2100 sec

(g) t = 7320 sec (h) t = 7320 sec (i) t = 7320 sec

(j) t = 25800 sec (k) t = 25800 sec (l) t = 25800 sec

Figure 4.10: Development of Saltwater Wedge with Time in $CASE - 4D/S$ [First Column: Experimental Images; Second Column: Output of G-Channel Based Image Analysis; Third Column: Numerical Simulation, The Color Maps Indicate Concentration]. All dimensions are in mm.

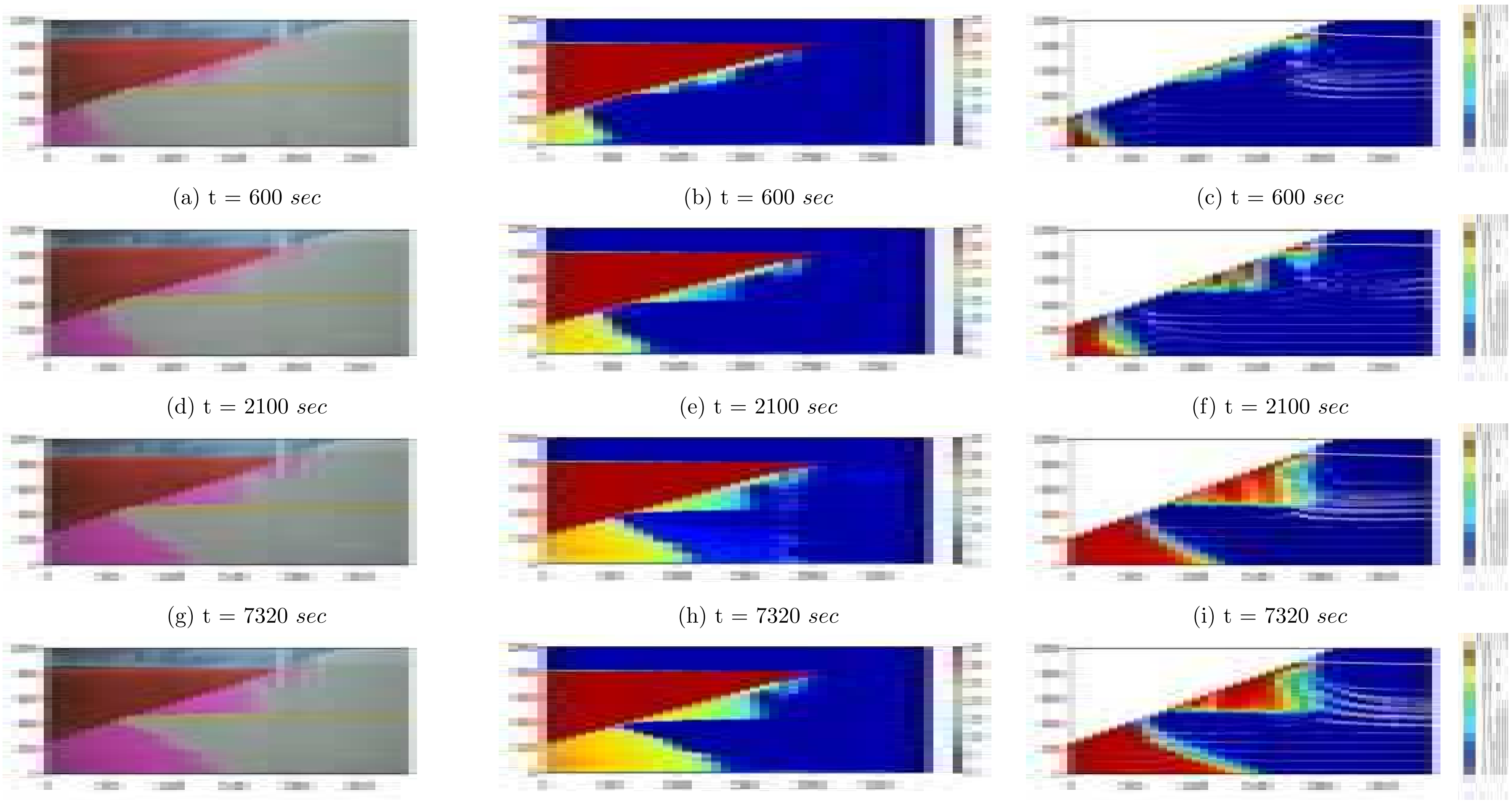

(a) t = 600 sec (b) t = 600 sec (c) t = 600 sec

(d) t = 2100 sec (e) t = 2100 sec (f) t = 2100 sec

(g) t = 7320 sec (h) t = 7320 sec (i) t = 7320 sec

(j) t = 25800 sec (k) t = 25800 sec (l) t = 25800 sec

Figure 4.11: Development of Saltwater Wedge with Time in $CASE - 4A/T$ [First Column: Experimental Images; Second Column: Output of G-Channel Based Image Analysis; Third Column: Numerical Simulation, The Color Maps Indicate Concentration]. All dimensions are in mm.

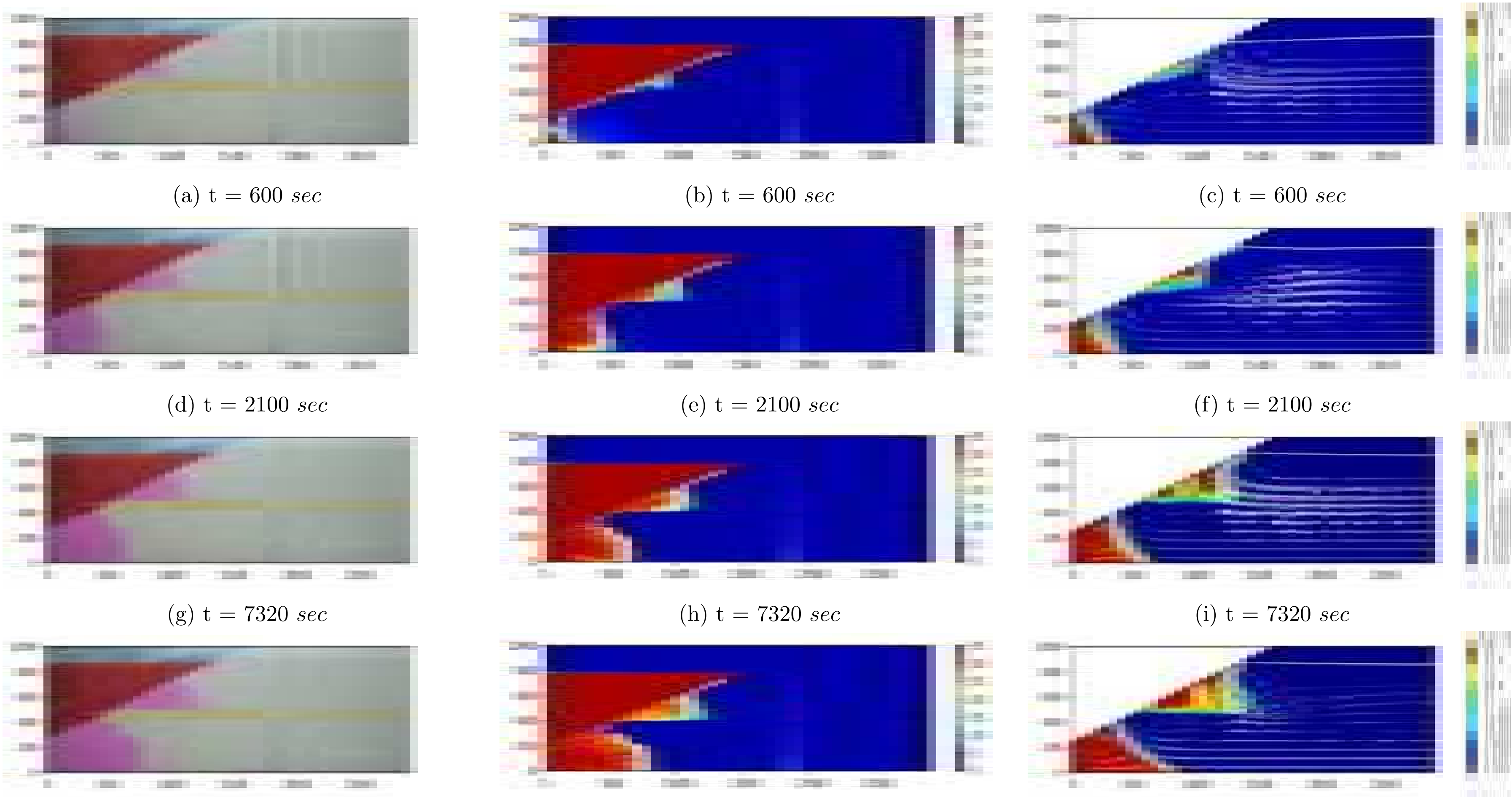

(a) t = 600 sec (b) t = 600 sec (c) t = 600 sec

(d) t = 2100 sec (e) t = 2100 sec (f) t = 2100 sec

(g) t = 7320 sec (h) t = 7320 sec (i) t = 7320 sec

(j) t = 25800 sec (k) t = 25800 sec (l) t = 25800 sec

Figure 4.12: Development of Saltwater Wedge with Time in $CASE-4B/T$ [First Column: Experimental Images; Second Column: Output of G-Channel Based Image Analysis; Third Column: Numerical Simulation, The Color Maps Indicate Concentration]. All dimensions are in mm.

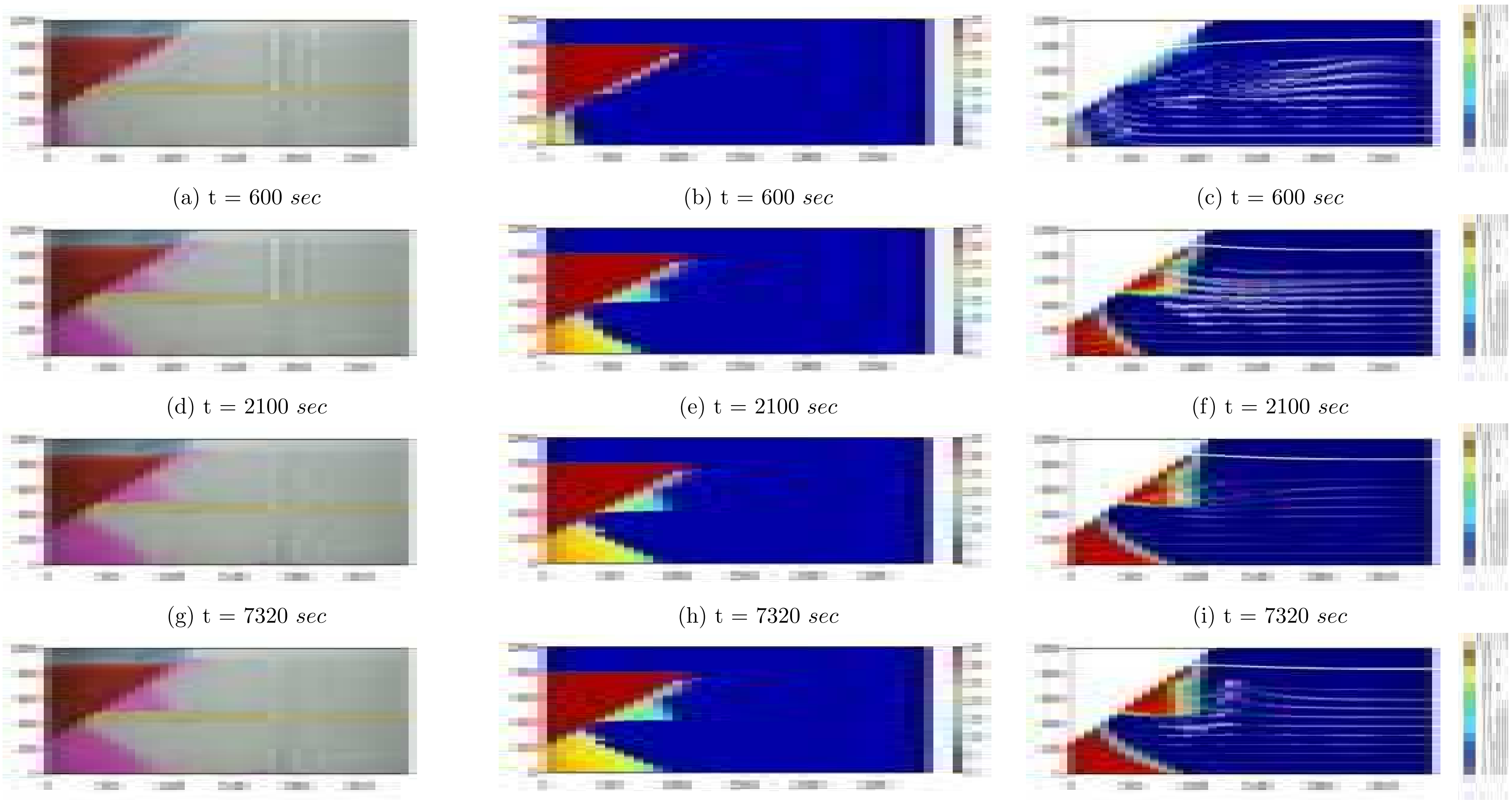

(a) t = 600 *sec* (b) t = 600 *sec* (c) t = 600 *sec*

(d) t = 2100 *sec* (e) t = 2100 *sec* (f) t = 2100 *sec*

(g) t = 7320 *sec* (h) t = 7320 *sec* (i) t = 7320 *sec*

(j) t = 25800 *sec* (k) t = 25800 *sec* (l) t = 25800 *sec*

Figure 4.13: Development of Saltwater Wedge with Time in $CASE - 4C/T$ [First Column: Experimental Images; Second Column: Output of G-Channel Based Image Analysis; Third Column: Numerical Simulation, The Color Maps Indicate Concentration]. All dimensions are in mm.

(a) t = 600 sec

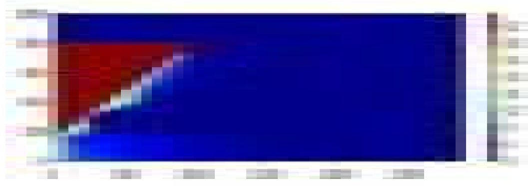

(b) t = 600 sec

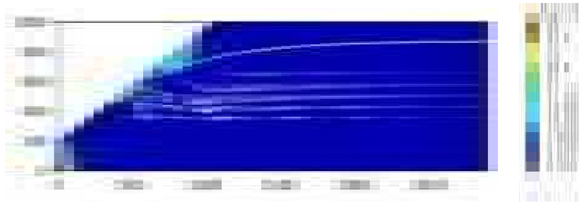

(c) t = 600 sec

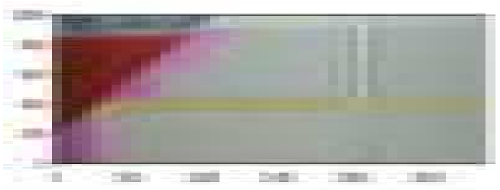

(d) t = 2100 sec

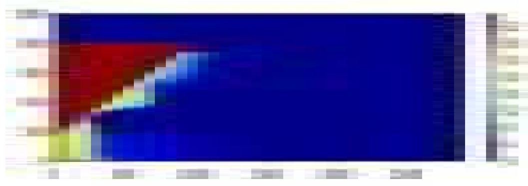

(e) t = 2100 sec

(f) t = 2100 sec

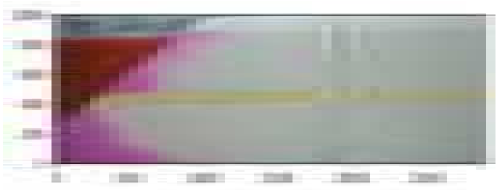

(g) t = 7320 sec

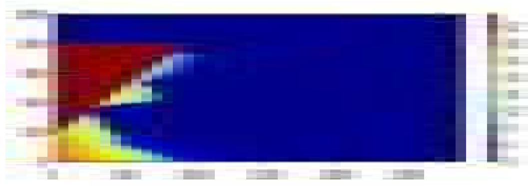

(h) t = 7320 sec

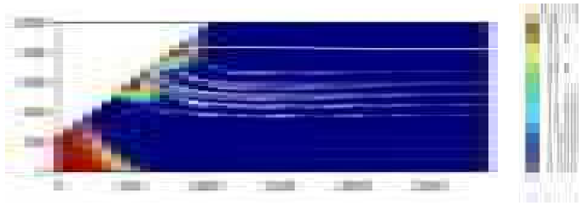

(i) t = 7320 sec

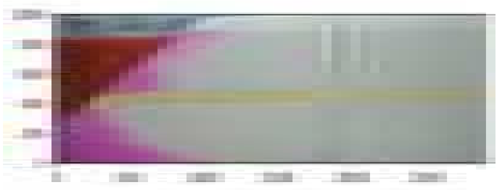

(j) t = 25800 sec

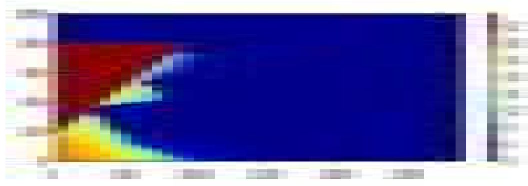

(k) t = 25800 sec

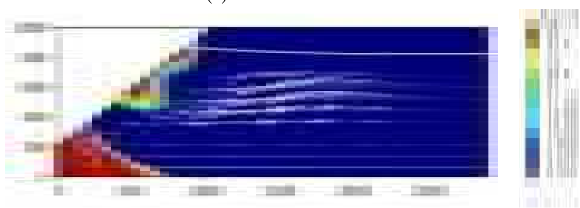

(l) t = 25800 sec

Figure 4.14: Development of Saltwater Wedge with Time in $CASE - 4D/T$ [First Column: Experimental Images; Second Column: Output of G-Channel Based Image Analysis; Third Column: Numerical Simulation, The Color Maps Indicate Concentration]. All dimensions are in mm.

4.4.1 Pore Water Pressure Measurement

Numerical and experimental (Pore Water Pressure Measurement) hydraulic head values were plotted to check the consistency of the obtained results. Figure 4.15 shows the plots corresponding to $CASE-4A/S$, $CASE-4B/S$, $CASE-4C/S$, and $CASE-4D/S$ with a 0.5 *cm* band on both sides. The outlier clusters corresponding to different pressure transducers are clearly visible from the plots. Spatial location of pressure transducers ($PS1$, $PS2$, $PS3$, $PS4$, $PS5$, $PS6$) were fixed with respect to *Sand Box Model* for cases. In $CASE-4A/S$ all the pressure transducers showed good match except $PS4$ (in confined layer). This was due to the influence of submarine groundwater discharge (SGD). Similar effects were also observed in $PS4$ and $PS3$ for $CASE-4B/S$ and $CASE-4D/S$, respectively. Deviation in $PS5$ (unconfined layer) was due to freshwater boundary effect in $CASE-4C/S$. This overestimation was due to marginal rise of water level near right boundary.

Time varying experimental head values for $CASE-4A/T$, $CASE-4B/T$, $CASE-4C/T$, $CASE-4D/T$ are shown in Figure 4.16. Numerical and experimental hydraulic head values were plotted in Figure 4.17 with 1 *cm* band on both sides. Submarine groundwater discharge (SGD) was observed for $PS4$ in $CASE-4A/T$. Right side boundary effect was prominent in $PS6$ (confined layer) for $CASE-4B/T$. Similar effect was also observed in $CASE-4C/T$ and $CASE-4D/T$ for $PS5$ (unconfined layer).

4.4.2 Comparison with Analytical Expression

Comparative analysis was performed with saltwater-freshwater interface corresponding to 50%-salinity line from FEFLOW and processed images (G-Channel Based Image Analysis). Saltwater-freshwater interface toe location (l_T) and submarine groundwater discharge gap (ζ_0) were determined analytically (Equations **??** and **??**), numerically and experimentally. The analytical (Van der Veer, 1977) values of l_T and ζ_0 for unconfined layer are 507 *mm* and 564 *mm*, respectively. The FEFLOW simulations underpredict the ζ_0 compared to the experimental value (Tables 4.4) under static saltwater side boundary condition ($CASE-4A/S$, $CASE-4B/S$, $CASE-4C/S$, $CASE-4D/S$). SGD gap (ζ_0) varies with beach slope for both unconfined and confined layers. Figure 4.18 shows saltwater-freshwater interface variations with beach slope under static saltwater side condition.

The FEFLOW simulations under-predict the ζ_0 compared to the experimental

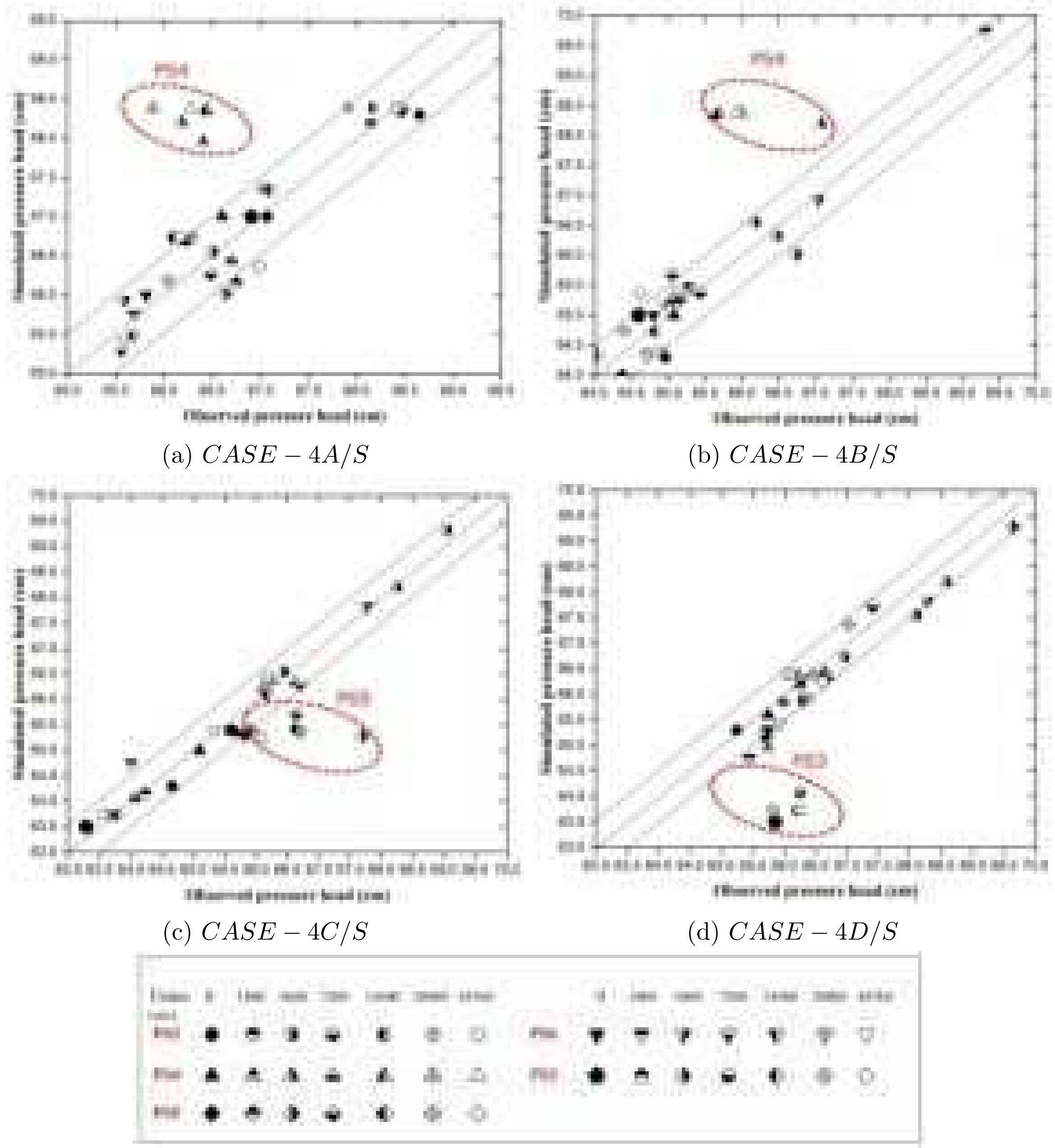

(a) $CASE - 4A/S$ (b) $CASE - 4B/S$

(c) $CASE - 4C/S$ (d) $CASE - 4D/S$

Figure 4.15: Comparison Between Time Varying Observed and Numerically Simulated Pressure Head Data

value (Tables 4.5) for $CASE - 4A/T$, $CASE - 4B/T$, $CASE - 4C/T$, $CASE - 4D/T$. Overall increase in ζ_0 value was observed in tidal case (e.g., $CASE - 4A/T$) when compared to static one (e.g., $CASE - 4A/S$) with same beach slope. Figure 4.19 shows saltwater-freshwater interface variations with beach slope under tidal saltwater side condition.

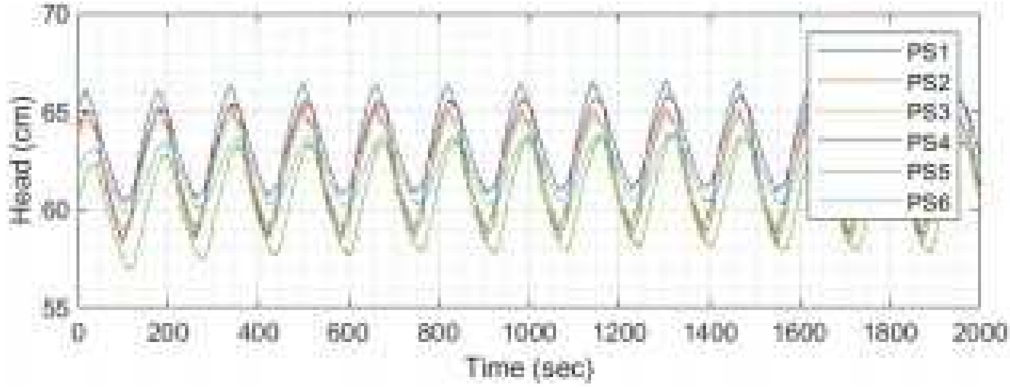

(a) $CASE - 4A/T$

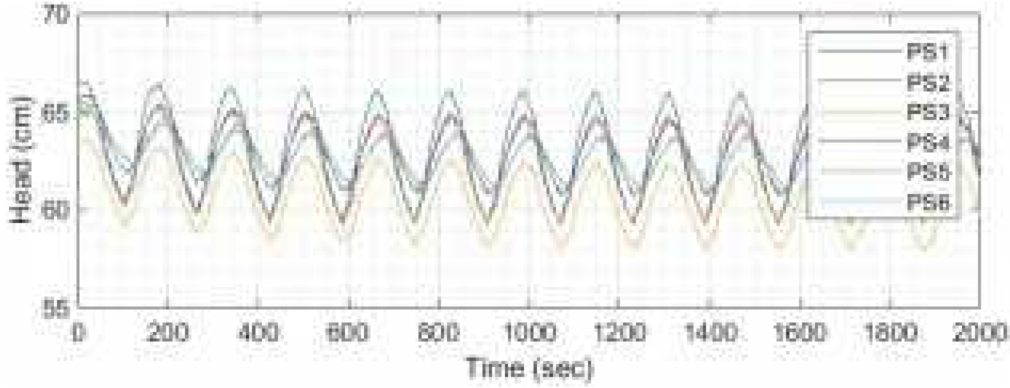

(b) $CASE - 4B/T$

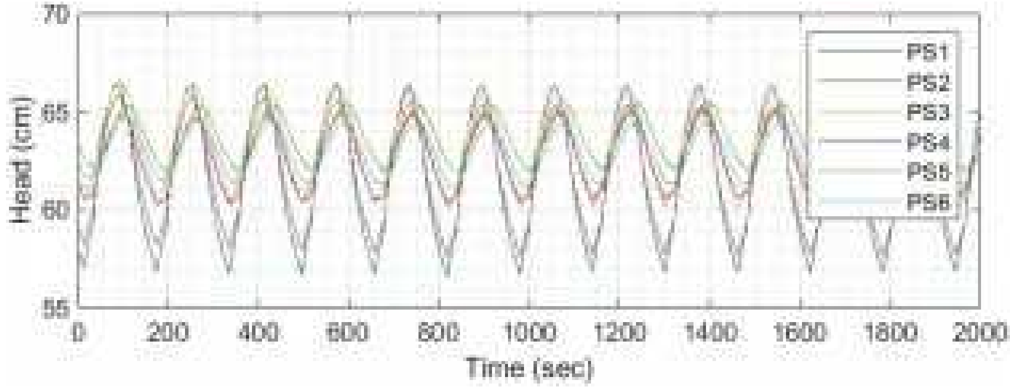

(c) $CASE - 4C/T$

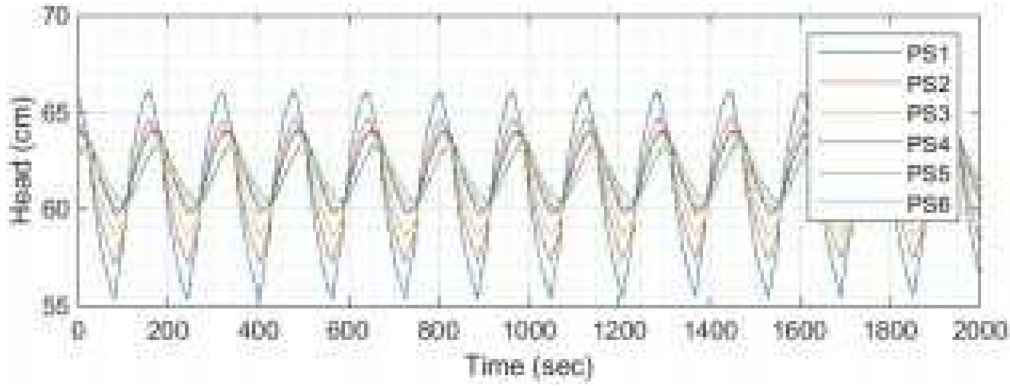

(d) $CASE - 4D/T$

Figure 4.16: Observed Time Varying Pore-Water Pressure Head

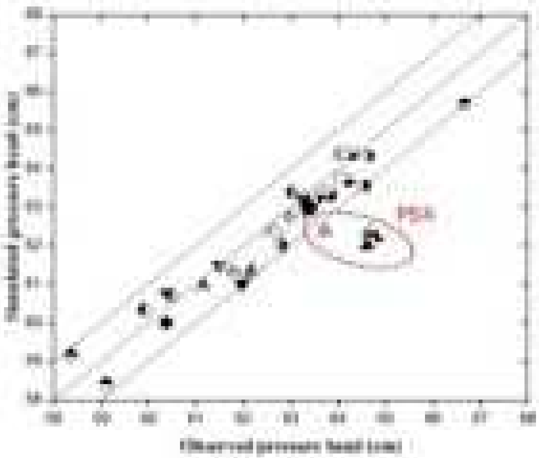

(a) $CASE-4A/T$

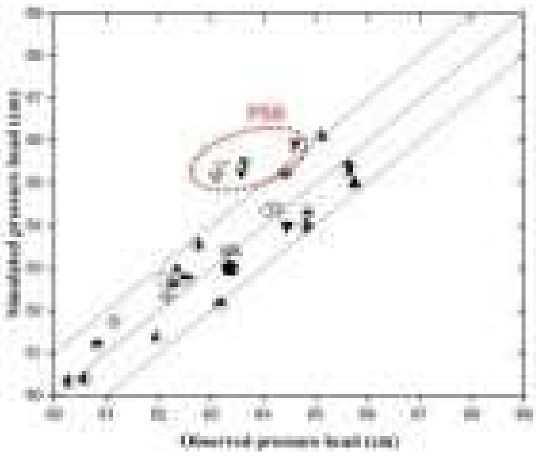

(b) $CASE-4B/T$

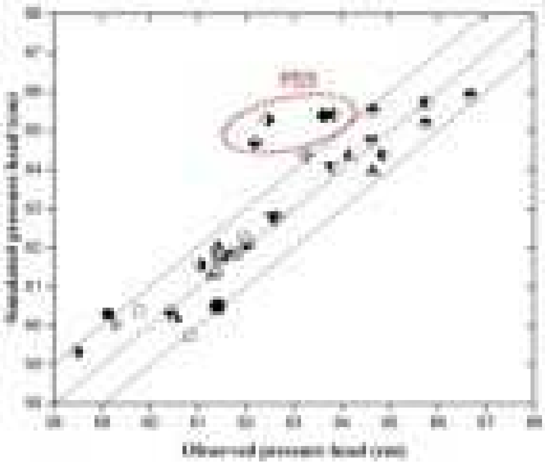

(c) $CASE-4C/T$

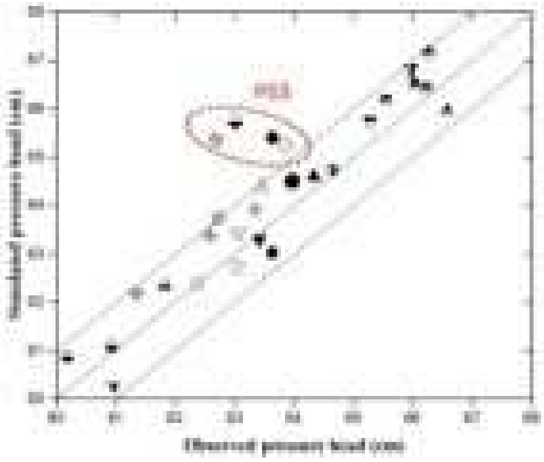

(d) $CASE-4D/T$

Figure 4.17: Comparison Between Time Varying Observed and Numerically Simulated Pressure Head Data

Table 4.4: Submarine Groundwater Discharge (SGD) Gap and Saltwater-Freshwater Interface Toe Length for Experiments with Multilayered Porous Media Under Static Saltwater Side Boundary Condition

Case	Slope	layer	Sand	$\zeta_o(mm)$ Expt	$\ell_T(mm)$ Expt	$\zeta_o(mm)$ FEFLOW	$\ell_T(mm)$ FEFLOW	$\zeta_{o-FEFLOW}/\zeta_{o-Expt}$
$CASE-4A/S$	15^0	Upper	Grade I IS Sand (d_{50}=1.12 mm)	119.73	188.29	95.24	192.39	0.795
		Lower	4 cm Low Permeable Layer	68.02	1194.34	25.51	1015.15	0.375
$CASE-4B/S$	20^0	Upper	Grade I IS Sand (d_{50}=1.12 mm)	112.43	222.85	85.98	248.45	0.764
		Lower	4 cm thick Low Permeable Layer	72.75	560.94	40.62	457.83	0.558
$CASE-4C/S$	25^0	Upper	Grade I IS Sand (d_{50}=1.12 mm)	149.28	203.65	84.09	218.58	0.563
		Lower	4 cm thick Low Permeable Layer	57.63	425.83	51.96	370.37	0.901
$CASE-4D/S$	30^0	Upper	Grade I IS sand (d_{50}=1.12 mm)	76.53	298.94	69.91	323.11	0.913
		Lower	4 cm thick Low Permeable Layer	107.71	405.93	74.64	317.04	0.692
							Avg= 0.69	

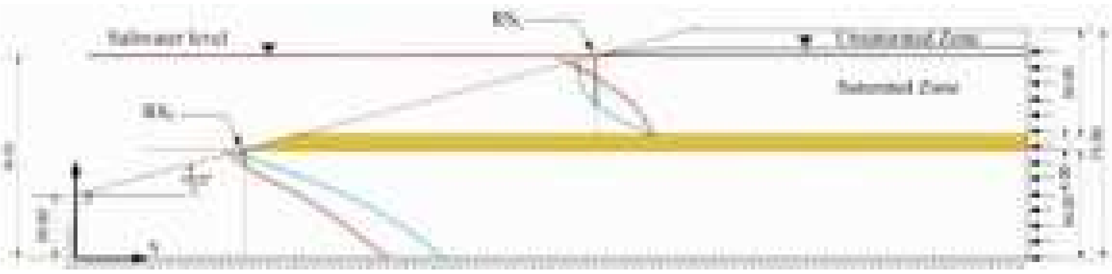

(a) $CASE-4A/S$

(b) $CASE-4B/S$

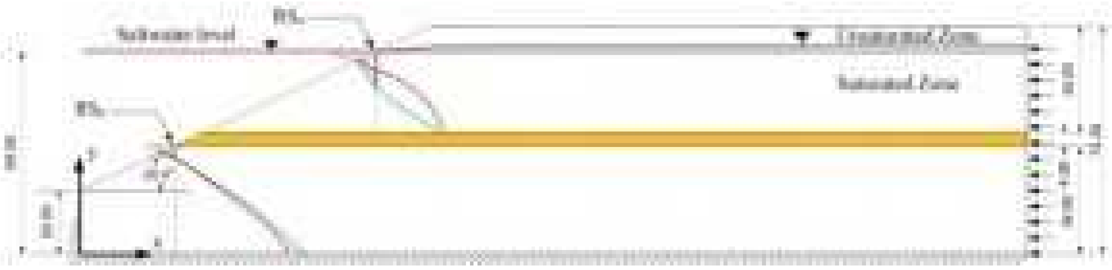

(c) $CASE-4C/S$

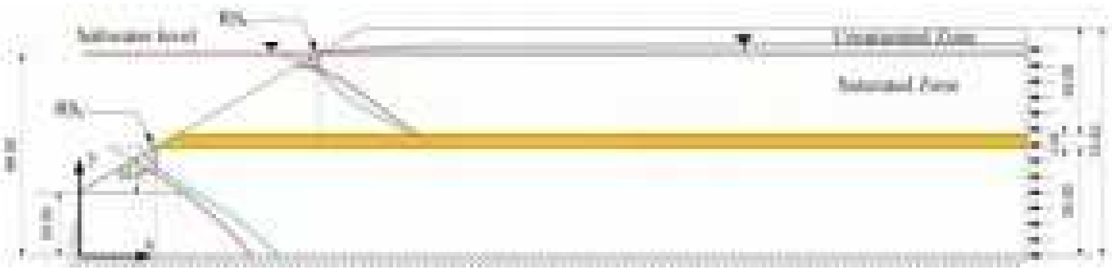

(d) $CASE-4D/S$

Figure 4.18: Saltwater-freshwater Interface for Experiments with Multilayered Porous Media Under Static Saltwater Side Boundary Condition (Red Line: FEFLOW Simulation Results; Blue Line: Experimental Results Obtained from G-Channel Based Image Analysis)

Table 4.5: Submarine Groundwater Discharge (SGD) Gap and Saltwater-Freshwater Interface Toe Length for Experiments with Multilayered Porous Media Under Tidal Saltwater Side Boundary Condition

Case	Slope	Layer	Sand	$\zeta_o(mm)$ Expt	$\ell_T(mm)$ Expt	$\zeta_o(mm)$ FEFLOW	$\ell_T(mm)$ FEFLOW	$\zeta_{o-FEFLOW}/\zeta_{o-Expt}$
$CASE-4A/T$	15^0	Upper	Grade I IS Sand (d_{50}=1.12 mm)	292	1798	97	1829	0.33
		Lower	4 cm thick Low Permeable Layer	45	1698	30	1695	0.66
$CASE-4B/T$	20^0	Upper	Grade I IS Sand (d_{50}=1.12 mm)	272	1342	163	1373	0.59
		Lower	4 cm thick Low Permeable Layer	104	972	94	969	0.90
$CASE-4C/T$	25^0	Upper	Grade I IS Sand (d_{50}=1.12 mm)	281	1063	201	1085	0.71
		Lower	4 cm thick Low Permeable Layer	139	841	96	839	0.69
$CASE-4D/T$	30^0	Upper	Grade I IS Sand (d_{50}=1.12 mm)	328	825	166	858	0.50
		Lower	4 cm thick Low Permeable Layer	125	630	122	484	0.97
							Avg= 0.66	

(a) $CASE - 4A/T$

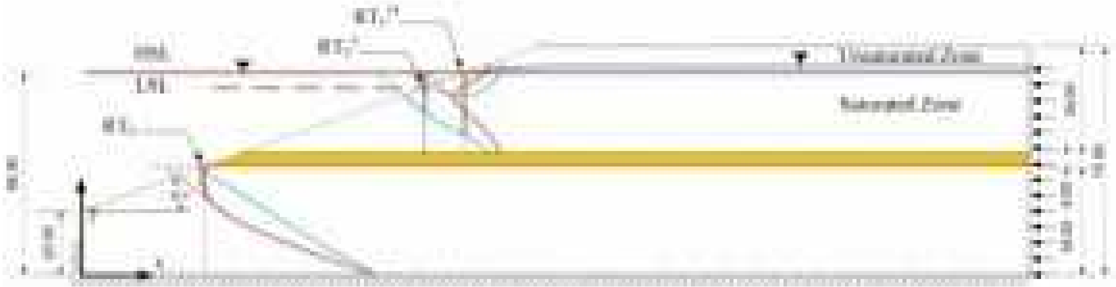

(b) $CASE - 4B/T$

(c) $CASE - 4C/T$

(d) $CASE - 4D/T$

Figure 4.19: Saltwater-freshwater Interface for Experiments with Multilayered Porous Media Under Static Saltwater Side Boundary Condition (Red Line: FEFLOW Simulation Results; Blue Line: Experimental Results Obtained from G-Channel Based Image Analysis)

4.4.3 Freshwater Flow Patterns

SGD flow pathways were identified by using tracer injection technique. *Rhodamine B* was utilized as the saltwater tracer. *Methyl Orange* was utilized as the external tracer for both static and tidal conditions. The external tracer was injected at different locations through a tube like setup under density neutral condition to minimize the externally generated buoyancy effect. The tracer experiments were started after attaining the quasi-steady state condition and continued till the tracer reached the saltwater surface. Time varying images of the tracer experiments under static and tidal conditions are shown in Figure 4.20 and Figure 4.21, respectively. It is evident that SGD particles move along the saltwater-freshwater interface zone and rise in upward to the intersection point in unconfined layer for static cases. SGD Particles get discharged to the saltwater region through the intermediate zone of saltwater wedge and USP for tidal cases.

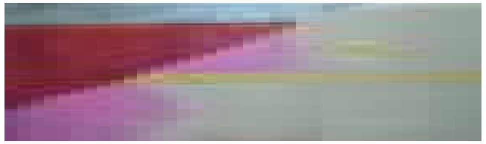

(a) $CASE-4A/S$ at t = 0 sec

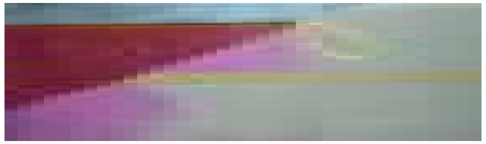

(b) $CASE-4A/S$ at t = 3600 sec

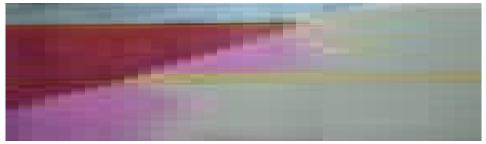

(c) $CASE-4A/S$ at t = 7200 sec

(d) $CASE-4B/S$ at t = 0 sec

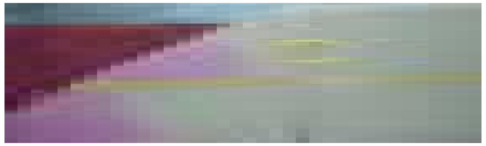

(e) $CASE-4B/S$ at t = 3600 sec

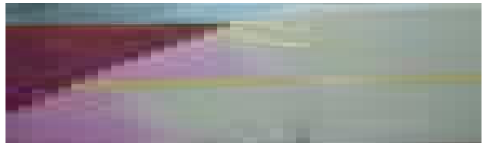

(f) $CASE-4B/S$ at t = 7200 sec

(g) $CASE-4C/S$ at t = 0 sec

(h) $CASE-4C/S$ at t = 3600 sec

(i) $CASE-4C/S$ at t = 7200 sec

(j) $CASE-4D/S$ at t = 0 sec

(k) $CASE-4D/S$ at t = 3600 sec

(m) $CASE-4D/S$ at t = 7200 sec

(l) 30^0 sloping seepage face

Figure 4.20: SGD Flow Pathways for Experiments with Multilayered Porous Media Under Static Saltwater Side Boundary Condition

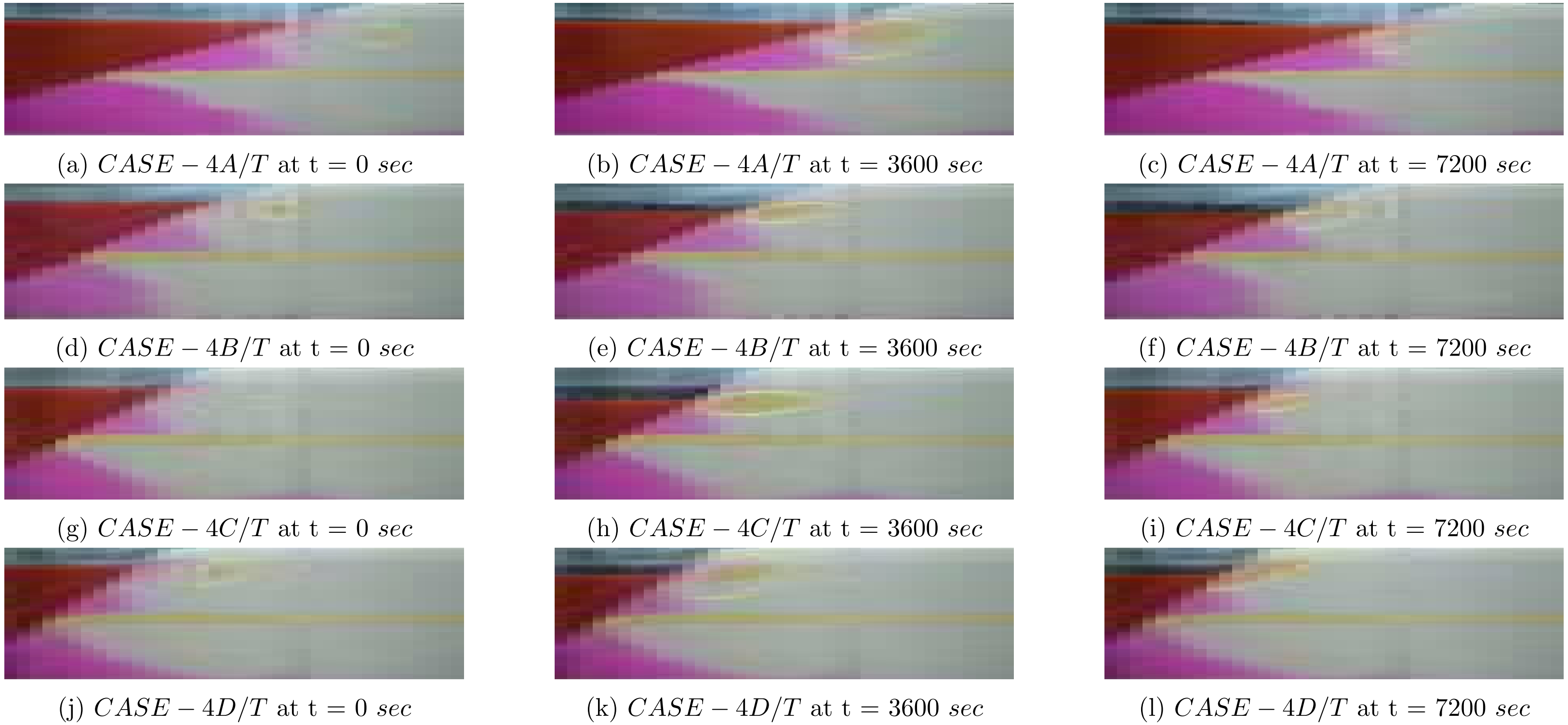

(a) $CASE-4A/T$ at t = 0 sec
(b) $CASE-4A/T$ at t = 3600 sec
(c) $CASE-4A/T$ at t = 7200 sec
(d) $CASE-4B/T$ at t = 0 sec
(e) $CASE-4B/T$ at t = 3600 sec
(f) $CASE-4B/T$ at t = 7200 sec
(g) $CASE-4C/T$ at t = 0 sec
(h) $CASE-4C/T$ at t = 3600 sec
(i) $CASE-4C/T$ at t = 7200 sec
(j) $CASE-4D/T$ at t = 0 sec
(k) $CASE-4D/T$ at t = 3600 sec
(l) $CASE-4D/T$ at t = 7200 sec

Figure 4.21: SGD Flow Pathways for Experiments with Multilayered Porous Media Under Tidal Saltwater Side Boundary Condition

4.5 Summary

The current Chapter included the physical experiments, numerical simulations and image analysis for the multilayered (Grade-I IS Sand) sloping beach under static and tidal saltwater boundary conditions. A comprehensive analysis was performed to quantify the influence of sloping beach on saltwater dynamics in multilayered porous media. The next Chapter presents Dimensional Analysis of the single and multilayered experiments under static and tidal saltwater side boundary conditions.

Chapter 6

Overview and Conclusions

6.1 Overview

The major objective of the Thesis was to study the influence of beach slope and tidal conditions on saltwater dynamics in single and multilayered porous media. Experiments were performed in a 2*D Sand Box Model* (longitudinal & vertical) to study the beach slope effect in both unconfined and confined aquifer configurations under tidal and non-tidal (static) conditions. Summary of the experimental cases for single and multilayered porous media are presented in Table 6.1 and Table 6.2, respectively. The cases $CASE-1/S$, $CASE-3A/S$, $CASE-3B/S$, $CASE-3C/S$, $CASE-3D/S$ were corresponding to single layered porous media under static saltwater side boundary condition. The saltwater side boundary condition was changed to tidal one in $CASE-3A/T$, $CASE-3B/T$, $CASE-3C/T$, $CASE-3D/T$. The cases: $CASE-2/S$, $CASE-4A/S$, $CASE-4B/S$, $CASE-4C/S$, $CASE-4D/S$ were corresponding to multilayered porous media under static saltwater side boundary condition. The saltwater side boundary condition was changed to tidal one in cases: $CASE-4A/T$, $CASE-4B/T$, $CASE-4C/T$, $CASE-4D/T$. Locally available *Clean Sand* was utilized as aquifer material in $CASE-1/S$ and$CASE-2/S$. However, Grade-I IS Sand was used for all other cases. *Bentonite* was used for low permeability layer. *Rohdamine B* was utilized as the saltwater tracer. Time varying pore-water pressure and images were captured during the experiments. A novel G-Channel based image analysis technique was proposed for identification of saltwater-freshwater interface and concentration distribution within the porous media. Laboratory experiments were validated by FEFLOW based numerical models. Time varying saltwater intrusion flow pattern from experiments, G-Channel based image analysis and numerical simulations (0.5-concentration isoline) were utilized for comprehensive analysis. Reasonable match of experiment, image analysis and numerical simulation results

Table 6.1: Configurations for Experiments with Single Layered Porous Media Under Static and Tidal Saltwater Side Boundary Conditions

CASES	Beach Slope	Sand	Stratification	Saltwater Boundary Conditions
$CASE-1/S$	15^0	Clean Sand (d_{50} = 1.024 mm)	No	Static
$CASE-3A/S$	15^0	Grade I IS Sand (d_{50}=1.12 mm)	No	Static
$CASE-3B/S$	20^0	Grade I IS Sand (d_{50}=1.12 mm)	No	Static
$CASE-3C/S$	25^0	Grade I IS Sand (d_{50}=1.12 mm)	No	Static
$CASE-3D/S$	30^0	Grade I IS Sand (d_{50}=1.12 mm)	No	Static
$CASE-3A/T$	15^0	Grade I IS Sand (d_{50}=1.12 mm)	No	Tidal
$CASE-3B/T$	20^0	Grade I IS Sand (d_{50}=1.12 mm)	No	Tidal
$CASE-3C/T$	25^0	Grade I IS Sand (d_{50}=1.12 mm)	No	Tidal
$CASE-3D/T$	30^0	Grade I IS Sand (d_{50}=1.12 mm)	No	Tidal

were obtained for all the cases. Submarine groundwater discharge (SGD) pathways were identified through tracer injection technique for all the cases. Flow circulation mechanism in saltwater wedge was also identified in $CASE-1/S$. Dimensional Analysis was performed for identification of influencing non-dimensional parameters. Non-dimensional parameter based equations were identified for saltwater-freshwater interface toe length (L_S) and SGD Gap (ζ_0) calculation.

Table 6.2: Configurations for Experiments with Multilayered Porous Media Under Static and Tidal Saltwater Side Boundary Conditions

CASES	Beach Slope	Sand	Stratification	Saltwater Boundary Conditions
$CASE-2/S$	15^0	Clean Sand ($d_{50} = 1.024\ mm$) 30 mm clay layer	Yes	Static
$CASE-4A/S$	15^0	Grade I IS Sand (d_{50}=1.12 mm) 40 mm clay layer	Yes	Static
$CASE-4B/S$	20^0	Grade I IS Sand (d_{50}=1.12 mm) 40 mm clay layer	Yes	Static
$CASE-4C/S$	25^0	Grade I IS Sand (d_{50}=1.12 mm) 40 mm clay layer	Yes	Static
$CASE-4D/S$	30^0	Grade I IS Sand (d_{50}=1.12 mm) 40 mm clay layer	Yes	Static
$CASE-4A/T$	15^0	Grade I IS Sand (d_{50}=1.12 mm) 40 mm clay layer	Yes	Tidal
$CASE-4B/T$	20^0	Grade I IS Sand (d_{50}=1.12 mm) 40 mm clay layer	Yes	Tidal
$CASE-4C/T$	25^0	Grade I IS Sand (d_{50}=1.12 mm) 40 mm clay layer	Yes	Tidal
$CASE-4D/T$	30^0	Grade I IS Sand (d_{50}=1.12 mm) 40 mm clay layer	Yes	Tidal

6.2 Conclusions

The following conclusions can be inferred from the present Thesis:

- Experimental and numerical analyses showed that the movement rate and volume of the saltwater wedge (i.e., saltwater-freshwater interface toe length) decreases with the increase in beach slope (e.g., $\alpha = 15^0$ to $\alpha = 30^0$). Saltwater intrusion occurred rapidly, i.e., size of the saltwater wedge increases, for flatter slopes ($CASE-3A/S$). Thus saltwater-freshwater interface intruded less in $CASE-3D/S$. Both experimental and numerical solutions showed similar trends.

- Fingering effect is prominent in $CASE-3A/S$ for 15° slope. It is evident that initial saltwater fingering effect reduces with the increase in beach slope $CASE-3D/S$ for 30°. However, under tidal condition finger effect was observed only in $CASE-3A/T$ for the flatter slope. This was due to scale effect.

- The G-Channel (of R-G-B) based image analysis technique identified the saltwater-freshwater interface and concentration gradient from the experimental images. The 50% concentration isolines obtained from the numerical simulations were matched with the interfaces obtained from the image analysis. Narrow mixing zone was observed for the current set of experiments.

- Numerically simulated and transient pore-water pressure head data quantified the time-varying saltwater movement in porous medium. Pressure transducer placed near to the right boundary showed over-height condition ($PS6$ in $CASE-3B/S$). This was due to marginal rise of water level in presence of freshwater flux.

- Tide significantly alters the seawater circulation pattern. In case of stratified porus medium, saltwater movement in lower confined layer was slower than the movement in upper unconfined layer for both tidal and static seaside conditions. However, intrusion length decreases under tidal condition.

- Time required to reach the quasi-steady condition was less under static condition (e.g., $CASE-3A/S$). It increases with the increase in beach slope for the single layered experimental analysis under static boundary conditions. Similar trend was also observed for tidal condition. However, marginal rise in overall experimental time was seen in tidal cases and (e.g., $CASE-3D/T$) compared to static one (e.g., $CASE-3D/S$).

- Upper saline plume (USP) developed for all experimental cases for unconfined layer in single and multilayered systems under tidal saltwater side boundary condition. The extent of the upper saline plume was dependent on the freshwater flux.

- Submarine groundwater discharge (SGD) gap (ζ_0) obtained from the physical experiments vary with slopes. The vertical SGD gap (ζ_0) decreases with increase in beach face slope whereas the SWI toe length increases. Ratio of experimental to analytical (Van der Veer, 1977) submarine groundwater discharge (SGD) gap (ζ_0) varied from 52% to 28% with increase in beach slope (15^0 to 30^0) for single layered system under static saltwater boundary condition. However, increase (51% to 94%) in SWI toe length ratio (experimental to analytical) was observed for increase in beach slope under similar conditions. Under tidal condition, SGD gap ratio decreased from 79% to 65% with the increase in slope (15^0 to 30^0). Overall increase (30% to 43%) in SWI toe length ratio was observed for increase in beach slope under similar conditions.

- Submarine groundwater discharge (SGD) flow pathways were identified by density neutral tracer injection technique for unconfined layer in single and multilayered systems. SGD particles move along the saltwater-freshwater interface zone and rise in upward direction up to the intersection point intersection point of saltwater level and sloping beach face under static condition. Particles get discharged to the saltwater region through the intermediate zone of saltwater wedge and USP under tidal condition.

- Dimensionless groups were identified for both tidal and non-tidal conditions. The saltwater-freshwater interface toe length and submarine groundwater discharge gap values were dependent on beach slope. Flow stability was determined on the basis of Rayleigh number ($R_a^\star = 150$ to 250 or 750).

A number of experiments were performed to quantify the influence of beach slope on saltwater dynamics in porous media. This study addressed some of the existing gaps in the available frameworks/ methodologies. The quantification framework should be applicable to other groundwater contaminant movement studies with minor modifications. In field situations $2D$ Electrical Resistivity Tomography (ERT) data can be utilized in place of experimental images.

6.3 Recommendations for Future Work

The present study can be extended to the following to enhance the understanding of tidal influence on coastal aquifers:

- The density-dependent experiments should be done for flatter beach slopes (less than 10^0) and Island aquifer systems (tidal condition on both sides).
- Length of the Sand Box Model should be increased to create effective semi-infinite aquifer system.
- Number of pressure transducers should be increased to capture true 2D variation.
- Introduction of tensiometer and soil moisture sensors would help in understanding the capillary effect.

References

Abarca, E., Carrera, J., Sánchez-Vila, X., and Dentz, M. (2007). Anisotropic dispersive henry problem. *Advances in Water Resources*, 30(4):913–926.

Abdoulhalik, A., Abdelgawad, A. M., and Ahmed, A. A. (2020). Impact of layered heterogeneity on transient saltwater upconing in coastal aquifers. *Journal of Hydrology*, 581:124393.

Abdoulhalik, A., Ahmed, A., and Hamill, G. (2017). A new physical barrier system for seawater intrusion control. *Journal of Hydrology*, 549:416–427.

Abdoulhalik, A. and Ahmed, A. A. (2017a). The effectiveness of cutoff walls to control saltwater intrusion in multi-layered coastal aquifers: Experimental and numerical study. *Journal of environmental management*, 199:62–73.

Abdoulhalik, A. and Ahmed, A. A. (2017b). How does layered heterogeneity affect the ability of subsurface dams to clean up coastal aquifers contaminated with seawater intrusion. *Journal of hydrology*, 553:708–721.

Abdoulhalik, A. and Ahmed, A. A. (2018). Transient investigation of saltwater upconing in laboratory-scale coastal aquifer. *Estuarine, Coastal and Shelf Science*, 214:149–160.

Adegoke, K. A. and Bello, O. S. (2015). Dye sequestration using agricultural wastes as adsorbents. *Water Resources and Industry*, 12:8–24.

Armanuos, A. M., Ibrahim, M. G., Mahmod, W. E., Takemura, J., and Yoshimura, C. (2019). Analysing the combined effect of barrier wall and freshwater injection countermeasures on controlling saltwater intrusion in unconfined coastal aquifer systems. *Water Resources Management*, 33(4):1265–1280.

Bear, J. (1999). Conceptual and mathematical modeling. In *Seawater Intrusion in Coastal Aquifers—Concepts, Methods and Practices*, pages 127–161. Springer.

Buckingham, E. (1914). Physically similar systems. *Journal of the Washington Academy of Sciences*, 4(13):347–353.

Cartwright, N., Nielsen, P., and Li, L. (2004). Experimental observations of watertable waves in an unconfined aquifer with a sloping boundary. *Advances in Water Resources*, 27(10):991–1004.

Chang, S. W. and Clement, T. P. (2013). Laboratory and numerical investigation of transport processes occurring above and within a saltwater wedge. *Journal of contaminant hydrology*, 147:14–24.

Cheng, A.-D. and Ouazar, D. (1999). Analytical solutions. In *Seawater intrusion in coastal aquifers—concepts, methods and practices*, pages 163–191. Springer.

Dagan, G. and Zeitoun, D. (1998a). Free-surface flow toward a well and interface upconing in stratified aquifers of random conductivity. *Water resources research*, 34(11):3191–3196.

Dagan, G. and Zeitoun, D. G. (1998b). Seawater-freshwater interface in a stratified aquifer of random permeability distribution. *Journal of Contaminant Hydrology*, 29(3):185–203.

Dalai, C., Munusamy, S. B., and Dhar, A. (2020). Experimental and numerical investigation of saltwater intrusion dynamics on sloping sandy beach under static seaside boundary condition. *Flow Measurement and Instrumentation*, 75:101794.

Dentz, M., Tartakovsky, D., Abarca, E., Guadagnini, A., Sanchez-Vila, X., and Carrera, J. (2006). Variable-density flow in porous media. *Journal of fluid mechanics*, 561:209–235.

Diersch, H.-J. and Kolditz, O. (2002). Variable-density flow and transport in porous media: approaches and challenges. *Advances in water resources*, 25(8-12):899–944.

Diersch, H.-J. G. (2013). *FEFLOW: finite element modeling of flow, mass and heat transport in porous and fractured media*. Springer Science & Business Media.

Dose, E. J., Stoeckl, L., Houben, G. J., Vacher, H., Vassolo, S., Dietrich, J., and Himmelsbach, T. (2014). Experiments and modeling of freshwater lenses in layered aquifers: steady state interface geometry. *Journal of hydrology*, 509:621–630.

Goswami, R. R. and Clement, T. P. (2007). Laboratory-scale investigation of saltwater intrusion dynamics. *Water Resources Research*, 43(4).

Hassanizadeh, S. M. and Leijnse, A. (1995). A non-linear theory of high-concentration-gradient dispersion in porous media. *Advances in Water Resources*, 18(4):203–215.

Hastings, C., Mosteller, F., Tukey, J. W., Winsor, C. P., et al. (1947). Low moments for small samples: a comparative study of order statistics. *The Annals of Mathematical Statistics*, 18(3):413–426.

Held, R., Attinger, S., and Kinzelbach, W. (2005). Homogenization and effective parameters for the henry problem in heterogeneous formations. *Water resources research*, 41(11).

Henry, H. R. (1960). Salt intrusion into coastal aquifers. Technical report.

Henry, H. R. (1964). Effects of dispersion on salt encroachment in coastal aquifers, in" seawater in coastal aquifers". *US Geological Survey, Water Supply Paper*, 1613:C70–C80.

Holzbecher, E. O. (1998). *Modeling density-driven flow in porous media: principles, numerics, software*. Springer Science & Business Media.

Houben, G. and Post, V. E. (2017). The first field-based descriptions of pumping-induced saltwater intrusion and upconing. *Hydrogeology Journal*, 25(1):243–247.

Jakovovic, D., Werner, A. D., de Louw, P. G., Post, V. E., and Morgan, L. K. (2016). Saltwater upconing zone of influence. *Advances in Water Resources*, 94:75–86.

Jiao, C.-Y. and Hötzl, H. (2004). An experimental study of miscible displacements in porous media with variation of fluid density and viscosity. *Transport in porous media*, 54(2):125–144.

Ketabchi, H., Mahmoodzadeh, D., Ataie-Ashtiani, B., Werner, A. D., and Simmons, C. T. (2014). Sea-level rise impact on fresh groundwater lenses in two-layer small islands. *Hydrological Processes*, 28(24):5938–5953.

Kim, I. H. and Yang, J.-S. (2018). Prioritizing countermeasures for reducing seawater-intrusion area by considering regional characteristics using seawat and a multicriteria decision-making method. *Hydrological Processes*, 32(25):3741–3757.

Kim, K.-Y., Chon, C.-M., and Park, K.-H. (2007). A simple method for locating the fresh water–salt water interface using pressure data. *Groundwater*, 45(6):723–728.

Konz, M., Ackerer, P., Meier, E., Huggenberger, P., Zechner, E., and Gechter, D. (2008). On the measurement of solute concentrations in 2-d flow tank experiments.

Konz, M., Ackerer, P., Younes, A., Huggenberger, P., and Zechner, E. (2009a). Two-dimensional stable-layered laboratory-scale experiments for testing density-coupled flow models. *Water Resources Research*, 45(2).

Konz, M., Younes, A., Ackerer, P., Fahs, M., Huggenberger, P., and Zechner, E. (2009b). Variable-density flow in heterogeneous porous media—laboratory experiments and numerical simulations. *Journal of contaminant hydrology*, 108(3-4):168–175.

Kuan, W. K., Jin, G., Xin, P., Robinson, C., Gibbes, B., and Li, L. (2012). Tidal influence on seawater intrusion in unconfined coastal aquifers. *Water Resources Research*, 48(2).

Kuan, W. K., Xin, P., Jin, G., Robinson, C. E., Gibbes, B., and Li, L. (2019). Combined effect of tides and varying inland groundwater input on flow and salinity distribution in unconfined coastal aquifers. *Water Resources Research*, 55(11):8864–8880.

Lee, C.-H. and Cheng, R. T.-S. (1974). On seawater encroachment in coastal aquifers. *Water Resources Research*, 10(5):1039–1043.

Li, L., Barry, D., Stagnitti, F., and Parlange, J.-Y. (1999). Submarine groundwater discharge and associated chemical input to a coastal sea. *Water Resources Research*, 35(11):3253–3259.

Li, L., Barry, D. A., Jeng, D. S., and Prommer, H. (2004). Tidal dynamics of groundwater flow and contaminant transport in coastal aquifers. *Coastal aquifer management: Monitoring, modeling, and case studies*, pages 115–141.

List, E. J. (1965). *The stability and mixing of a density-stratified horizontal flow in a saturated porous medium.* PhD thesis, California Institute of Technology.

Liu, Y., Jiao, J. J., and Luo, X. (2016). Effects of inland water level oscillation on groundwater dynamics and land-sourced solute transport in a coastal aquifer. *Coastal Engineering*, 114:347–360.

Liu, Y., Mao, X., Chen, J., and Barry, D. A. (2014). Influence of a coarse interlayer on seawater intrusion and contaminant migration in coastal aquifers. *Hydrological Processes*, 28(20):5162–5175.

Llopis-Albert, C. and Pulido-Velazquez, D. (2014). Discussion about the validity of sharp-interface models to deal with seawater intrusion in coastal aquifers. *Hydrological Processes*, 28(10):3642–3654.

Lu, C., Cao, H., Ma, J., Shi, W., Rathore, S. S., Wu, J., and Luo, J. (2019). A proof-of-concept study of using a less permeable slice along the shoreline to increase fresh groundwater storage of oceanic islands: Analytical and experimental validation. *Water Resources Research*, 55(8):6450–6463.

Lu, C., Chen, Y., Zhang, C., and Luo, J. (2013). Steady-state freshwater–seawater mixing zone in stratified coastal aquifers. *Journal of Hydrology*, 505:24–34.

Luyun Jr, R., Momii, K., and Nakagawa, K. (2011). Effects of recharge wells and flow barriers on seawater intrusion. *Groundwater*, 49(2):239–249.

MacAllister, D., Jackson, M., Butler, A., and Vinogradov, J. (2018). Remote detection of saline intrusion in a coastal aquifer using borehole measurements of self-potential. *Water Resources Research*, 54(3):1669–1687.

Manickam, O. and Homsy, G. (1995). Fingering instabilities in vertical miscible displacement flows in porous media. *Journal of Fluid Mechanics*, 288:75–102.

Mehdizadeh, S. S., Karamalipour, S. E., and Asoodeh, R. (2017). Sea level rise effect on seawater intrusion into layered coastal aquifers (simulation using dispersive and sharp-interface approaches). *Ocean & Coastal Management*, 138:11–18.

Mehdizadeh, S. S., Ketabchi, H., Ghoroqi, M., and Hasanzadeh, A. K. (2020). Experimental and numerical assessment of saltwater recession in coastal aquifers by constructing check dams. *Journal of Contaminant Hydrology*, page 103637.

Mehdizadeh, S. S., Werner, A. D., Vafaie, F., and Badaruddin, S. (2014). Vertical leakage in sharp-interface seawater intrusion models of layered coastal aquifers. *Journal of Hydrology*, 519:1097–1107.

Mehnert, E. and Jennings, A. A. (1985). The effect of salinity-dependent hydraulic conductivity on saltwater intrusion episodes. *Journal of Hydrology*, 80(3-4):283–297.

MOEFCC (2017). Database on Coastal States of India. *Website of Ministry of Environment Forest and Climate Change website.*

Moore, W. S., Sarmiento, J. L., and Key, R. M. (2008). Submarine groundwater discharge revealed by 228 ra distribution in the upper atlantic ocean. *Nature Geoscience*, 1(5):309–311.

Nakagawa, K., Momii, K., and Berndtsson, R. (2005). Saltwater intrusion in coastal aquifer comparison between the cip and moc simulation technique. *Environmental Modeling & Assessment*, 10(4):323–329.

Nielsen, P. (1990). Tidal dynamics of the water table in beaches. *Water Resources Research*, 26(9):2127–2134.

Oostrom, M., Dane, J., Güven, O., and Hayworth, J. (1992). Experimental investigation of dense solute plumes in an unconfined aquifer model. *Water Resources Research*, 28(9):2315–2326.

Oostrom, M., Dane, J., Güven, O., Hayworth, J., and Hill, W. (1991). Concentration measurements in dense leachate plumes using a gamma radiation system. In *Symposium on Ground Water*, pages 287–292. ASCE.

Oswald, S. and Kinzelbach, W. (2004). Three-dimensional physical benchmark experiments to test variable-density flow models. *Journal of Hydrology*, 290(1-2):22–42.

Oswald, S. E., Spiegel, M. A., and Kinzelbach, W. (2007). Three-dimensional saltwater–freshwater fingering in porous media: contrast agent mri as basis for numerical simulations. *Magnetic resonance imaging*, 25(4):537–540.

Oz, I., Shalev, E., Yechieli, Y., and Gvirtzman, H. (2015). Saltwater circulation patterns within the freshwater–saltwater interface in coastal aquifers: Laboratory experiments and numerical modeling. *Journal of Hydrology*, 530:734–741.

Pearl, Z., Magaritz, M., and Bendel, P. (1993). Nuclear magnetic resonance imaging of miscible fingering in porous media. *Transport in porous media*, 12(2):107–123.

Pinder, G. F. and Cooper Jr, H. H. (1970). A numerical technique for calculating the transient position of the saltwater front. *Water Resources Research*, 6(3):875–882.

Post, V. E. A. and Werner, A. D. (2017). Coastal aquifers: Scientific advances in the face of global environmental challenges.

Reilly, T. E. and Goodman, A. S. (1985). Quantitative analysis of saltwater-freshwater relationships in groundwater systems—a historical perspective. *Journal of Hydrology*, 80(1-2):125–160.

Robinson, C., Gibbes, B., Carey, H., and Li, L. (2007a). Salt-freshwater dynamics in a subterranean estuary over a spring-neap tidal cycle. *Journal of Geophysical Research: Oceans*, 112(C9).

Robinson, C., Li, L., and Prommer, H. (2007b). Tide-induced recirculation across the aquifer-ocean interface. *Water Resources Research*, 43(7).

Robinson, C. E., Xin, P., Santos, I. R., Charette, M. A., Li, L., and Barry, D. A. (2018). Groundwater dynamics in subterranean estuaries of coastal unconfined aquifers: Controls on submarine groundwater discharge and chemical inputs to the ocean. *Advances in water resources*, 115:315–331.

Schincariol, R. A. and Schwartz, F. W. (1990). An experimental investigation of variable density flow and mixing in homogeneous and heterogeneous media. *Water Resources Research*, 26(10):2317–2329.

Schincariol, R. A., Schwartz, F. W., and Mendoza, C. A. (1994). On the generation of instabilities in variable density flow. *Water Resources Research*, 30(4):913–927.

Schotting, R., Moser, H., and Hassanizadeh, S. (1999). High-concentration-gradient dispersion in porous media: experiments, analysis and approximations. *Advances in Water Resources*, 22(7):665–680.

Shen, Y., Xin, P., and Yu, X. (2020). Combined effect of cutoff wall and tides on groundwater flow and salinity distribution in coastal unconfined aquifers. *Journal of Hydrology*, 581:124444.

Shi, W., Lu, C., Ye, Y., Wu, J., Li, L., and Luo, J. (2018). Assessment of the impact of sea-level rise on steady-state seawater intrusion in a layered coastal aquifer. *Journal of hydrology*, 563:851–862.

Shoushtari, S. M. H. J., Cartwright, N., Perrochet, P., and Nielsen, P. (2015). Influence of hysteresis on groundwater wave dynamics in an unconfined aquifer with a sloping boundary. *Journal of Hydrology*, 531:1114–1121.

Simmons, C. T., Fenstemaker, T. R., and Sharp Jr, J. M. (2001). Variable-density groundwater flow and solute transport in heterogeneous porous media: approaches, resolutions and future challenges. *Journal of Contaminant Hydrology*, 52(1-4):245–275.

Simmons, C. T. and Narayan, K. A. (1997). Mixed convection processes below a saline disposal basin. *Journal of Hydrology*, 194(1-4):263–285.

Simpson, M. and Clement, T. (2003). Theoretical analysis of the worthiness of henry and elder problems as benchmarks of density-dependent groundwater flow models. *Advances in Water Resources*, 26(1):17–31.

Simpson, M. J. and Clement, T. P. (2004). Improving the worthiness of the henry problem as a benchmark for density-dependent groundwater flow models. *Water Resources Research*, 40(1).

Smith, A. J. (2004). Mixed convection and density-dependent seawater circulation in coastal aquifers. *Water Resources Research*, 40(8).

Souza, W. R. and Voss, C. I. (1987). Analysis of an anisotropic coastal aquifer system using variable-density flow and solute transport simulation. *Journal of Hydrology*, 92(1-2):17–41.

Sriapai, T., Walsri, C., Phueakphum, D., and Fuenkajorn, K. (2012). Physical model simulations of seawater intrusion in unconfined aquifer. *Songklanakarin Journal of Science & Technology*, 34(6).

Stoeckl, L., Walther, M., and Graf, T. (2016). A new numerical benchmark of a freshwater lens. *Water Resources Research*, 52(4):2474–2489.

Strack, O. and Ausk, B. (2015). A formulation for vertically integrated groundwater flow in a stratified coastal aquifer. *Water Resources Research*, 51(8):6756–6775.

Swartz, C. H. and Schwartz, F. W. (1998). An experimental study of mixing and instability development in variable-density systems. *Journal of Contaminant Hydrology*, 34(3):169–189.

Van der Veer, P. (1977). Analytical solution for steady interface flow in a coastal aquifer involving a phreatic surface with precipitation. *Journal of Hydrology*, 34(1-2):1–11.

Volker, R. and Rushton, K. (1982). An assessment of the importance of some parameters for seawater intrusion in aquifers and a comparison of dispersive and sharp-interface modelling approaches. *Journal of Hydrology*, 56(3-4):239–250.

Voss, C. I. and Souza, W. R. (1987). Variable density flow and solute transport simulation of regional aquifers containing a narrow freshwater-saltwater transition zone. *Water Resources Research*, 23(10):1851–1866.

Walther, M., Graf, T., Kolditz, O., Liedl, R., and Post, V. (2017). How significant is the slope of the sea-side boundary for modelling seawater intrusion in coastal aquifers. *Journal of Hydrology*, 551:648–659.

Watson, S., Barry, D., Schotting, R., and Hassanizadeh, S. (2002). Validation of classical density-dependent solute transport theory for stable, high-concentration-gradient brine displacements in coarse and medium sands. *Advances in Water Resources*, 25(6):611–635.

Watson, T. A., Werner, A. D., and Simmons, C. T. (2010). Transience of seawater intrusion in response to sea level rise. *Water Resources Research*, 46(12).

Welty, C. and Gelhar, L. W. (1994). Evaluation of longitudinal dispersivity from nonuniform flow tracer tests. *Journal of Hydrology*, 153(1-4):71–102.

Werner, A. D., Bakker, M., Post, V. E., Vandenbohede, A., Lu, C., Ataie-Ashtiani, B., Simmons, C. T., and Barry, D. A. (2013). Seawater intrusion processes, investigation and management: recent advances and future challenges. *Advances in Water Resources*, 51:3–26.

Werner, A. D., Jakovovic, D., and Simmons, C. T. (2009). Experimental observations of saltwater up-coning. *Journal of Hydrology*, 373(1-2):230–241.

Wooding, R. (1963). Convection in a saturated porous medium at large rayleigh number or peclet number. *Journal of Fluid Mechanics*, 15(4):527–544.

Wooding, R., Tyler, S. W., and White, I. (1997). Convection in groundwater below an evaporating salt lake: 1. onset of instability. *Water Resources Research*, 33(6):1199–1217.

Wu, H., Lu, C., Yan, M., and Werner, A. D. (2020). Expanding freshwater lenses adjacent to gaining rivers through vertical low-hydraulic-conductivity barriers: Analytical and experimental validation. *Water Resources Research*, 56(2):e2019WR025750.

Yu, X., Xin, P., and Lu, C. (2019a). Seawater intrusion and retreat in tidally-affected unconfined aquifers: Laboratory experiments and numerical simulations. *Advances in Water Resources*, 132:103393.

Yu, X., Xin, P., Wang, S. S., Shen, C., and Li, L. (2019b). Effects of multi-constituent tides on a subterranean estuary. *Advances in Water Resources*, 124:53–67.

Zhang, B., Zheng, X., Zheng, T., Xin, J., Sui, S., and Zhang, D. (2019). The influence of slope collapse on water exchange between a pit lake and a heterogeneous aquifer. *Frontiers of Environmental Science & Engineering*, 13(2):20.

Zhang, Q., Volker, R., and Lockington, D. (2001). Influence of seaward boundary condition on contaminant transport in unconfined coastal aquifers. *Journal of Contaminant Hydrology*, 49(3-4):201–215.

Zhang, Q., Volker, R. E., and Lockington, D. A. (2002). Experimental investigation of contaminant transport in coastal groundwater. *Advances in Environmental Research*, 6(3):229–237.

Zhou, Y., Lim, D., Cupola, F., and Cardiff, M. (2016). Aquifer imaging with pressure waves—evaluation of low-impact characterization through sandbox experiments. *Water Resources Research*, 52(3):2141–2156.